Mechanical response of foams : elasticity, plasticity, and rearrangements

Deen, M.S. van

Mechanical Response of Foams:
Elasticity, Plasticity, and Rearrangements

PROEFSCHRIFT

ter verkrijging van
de graad van Doctor aan de Universiteit Leiden,
op gezag van Rector Magnificus prof. mr. C.J.J.M. Stolker,
volgens besluit van het College voor Promoties
te verdedigen op woensdag 9 november 2016
klokke 11.15 uur

door

Merlijn Sieward van Deen

geboren te 's-Gravenhage
in 1988

PROMOTOR

prof. dr. M.L. van Hecke

PROMOTIECOMMISSIE

dr. M.L. Manning (*Syracuse University, Syracuse, Verenigde Staten*)
prof. dr. P. Schall (*Universiteit van Amsterdam*)
dr. Z. Zeravcic (*ESPCI, Parijs, Frankrijk*)
prof. dr. J. Aarts
prof. dr. E.R. Eliel
dr. D.J. Kraft
prof. dr. M.A.G.J. Orrit
prof. dr. V. Vitelli

NEDERLANDSE TITEL

Mechanische eigenschappen van schuim:
elasticiteit, vervormbaarheid en herschikkingen.

COVER IMAGE

A 4096 particle packing (with periodic copies) at $P = 10^{-4}$.
Intensity variations indicate variations in the local stress.

Casimir PhD series, Delft-Leiden, 2016-30
ISBN 978-90-8593-274-1
Available on-line at `http://hdl.handle.net/1887/40902`

De waarheid is een raadsel, en dat gaat als volgt:
’t is een goede vriend, maar altijd te laat.

Spinvis, *Smalfilm*.

CONTENTS

CHAPTER 1

INTRODUCTION

Soft disordered materials, such as sand, mayonnaise, toothpaste and foams are all around us. These materials possess a fascinating property: depending on their confinement, they can act like a solid, like a liquid, or like something in between [2–5]. Wet sand is solid enough to build a sand castle (Fig. 1.1(a)) due to the attraction between grains. Walking on the beach plastically deforms it (Fig. 1.1(b)). Dry sand has no attraction, and without external confinement flows as if it were a liquid (Fig. 1.1(c)). In foams, bubbles normally often attract each other, preventing free-flowing states. Nonetheless, we can observe a transition from solid to liquid-like in the system: whipped cream is strong enough to hold its own weight (Fig. 1.2(a)), but we can make it flow by squeezing it out of a piping bag (Fig. 1.2(b)). Fascinatingly, this behavior is reversible: in the absence of forcing, the cream acts like a solid again.

(a) (b) (c)

FIGURE 1.1: Three states of sand: (a) a solid sand castle; (b) plastic deformation under forcing; (c) flow in an hourglass. [1]

(a) (b)

FIGURE 1.2: Whipped cream acts (a) like a solid when unperturbed yet (b) flows when it is forced. [6]

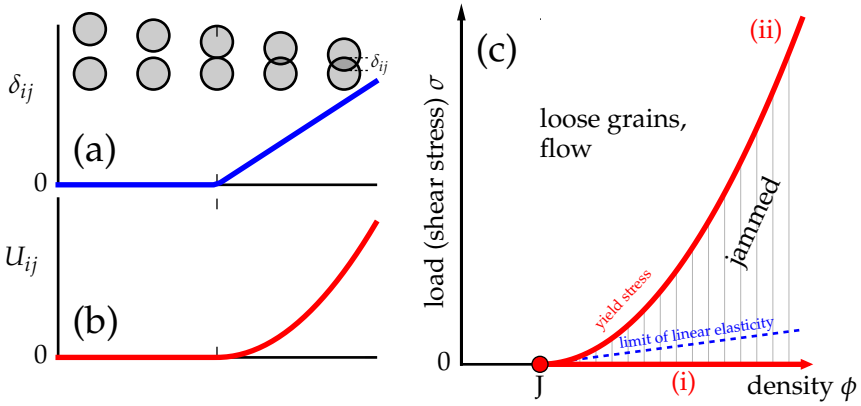

FIGURE 1.3: (a) In simulations, the interaction between particles depends on the *overlap* δ, which is zero if particles are not in contact and ≥ 0 if particles are in contact. (b) The potential for harmonic frictionless particles is quadratic in the overlap δ. (c) The load-density plane of the jamming phase diagram, based on [3, 7]. At the jamming transition (point J), any decrease in density ϕ or increase in shear stress σ will cause the system to unjam and flow. For any density $\phi > \phi_j$, there is a yield stress $\sigma_y(\phi)$ above which the system unjams and flows. Most current work has studied two boundaries in this diagram: (i) the $\sigma = 0$ jamming point, or (ii) the yielding boundary.

Why do sand and foam behave this way? This behavior originates from their particulate nature: the strength of the system as a whole depends on the interactions between the constituent particles, oil droplets or foam bubbles [3, 8]. These interactions can be tuned, for example by varying the wetness of the sand [9, 10], varying the air content of the foam [11, 12] or by varying the external confinement [11, 13–16]. By varying the interactions, a wide range of physical phenomena become accessible. Under high compression, each particle has strong interactions with many neighbors, and these systems act like sand on the beach or the whipped cream on a cake. However, when the particles lose contact, the system loses strength and starts to flow [13, 17, 18] — just like the sand in an hourglass. Finally, if the system is exposed to a high enough load, particles lose contact, and the system also starts to flow [11, 19, 20] — like the whipped cream in a piping bag. Many of the properties of these systems strongly depend on their distance from falling apart — on their distance to the *jamming transition* [7, 21]. This includes not only the load required to make the system flow, the *yield stress*, but also elastic properties such as the shear modulus, and geometric properties such as the average number of neighbors each particle interacts with [3, 5, 8, 13, 21–23]. For example, the yield stress vanishes completely when the system is at the brink of falling apart [11, 24, 25]. In other words, any infinitesimally small stress will push the system over the edge, and will cause the system to yield.

To better understand the behavior of these systems on a microscopic level, they have been modeled using simple models of interacting soft particles, where *(i)* particles are modeled using simple circles or spheres, *(ii)* particles only interact if they are in contact, and *(iii)* their interaction is a function of their *overlap* (Fig. 1.3(a)) [13, 21–23]. This research led to the proposal of a jamming *phase diagram* (Fig. 1.3(b)), where the jamming transition, *point J*, is a critical point [7]. At point J, any increase in load or any decrease in density will cause the system to fall apart. Most research has focused on one of two boundaries in the diagram: First, there is a significant amount of work on the zero-deformation limit, investigating at which density the jamming transition happens, and investigating static properties as a function of the distance to that point [13, 21–23, 26–29]. This includes linear elastic properties such as the shear modulus G and the bulk modulus K, as well as the infinitesimal movement of particles in response to infinitesimal perturbations [28, 30–34]. Second, research has focused on

the yield stress limit. The approach typically taken in simulation work is to investigate energy drops, plasticity and reversibility [35–38]. In contrast, experiments typically focus on the stress response in steady flow [39–42].

In this thesis, we have worked on understanding the behavior in between these two boundaries. First, in chapter 2, we use numerical simulations to probe the first unambiguous deviations from linear elastic response. In chapter 3, we extend this to determine the characteristics of rearrangements, and connect this to the reversibility of the system. Finally, in chapter 4, we probe the microscopic behavior of a foam in response to an external deformation.

In § 1.1 and § 1.2, we will now review earlier work on the behavior of soft amorphous systems. In § 1.1, we focus on numerical simulations, and focus on their relationship to our work in chapters 2 and 3. In § 1.2, we focus on experimental results in foams, emulsions and colloidal suspensions, and relate this to our work in chapter 4.

1.1 Jamming

In this section, we will focus on numerical simulations used to understand the behavior of soft disordered materials. The use of numerical simulations to study the microscopic behavior of materials has a rich history. As early as the 1940s and 1950s, computers were used to study problems in statistical physics using the Monte Carlo [43], Metropolis [44] and Potts [45] methods. Already in 1957, Alder and Wainwright [46] simulated colloidal hard sphere suspensions using event-driven molecular dynamics simulations. Nevertheless, computing power remained a limitation, and only in the 1990s extensive simulations of systems with many interacting particles became possible.

In the early 1990s, Bolton and Weaire [47] and Durian [22, 23] laid the foundations for numerical simulations of soft disordered materials. Bolton and Weaire probed the behavior of disordered foams using a surface tension-driven foam film simulation. Durian extended this work using a simpler model, where the foam bubbles are no longer deformable; instead, bubbles are treated as circles with simple pairwise interactions. In these model systems, both authors found *(i)* a transition from freely flowing behavior to jammed behavior at a critical packing fraction $\phi_c \approx 0.84$, *(ii)* evidence for a shear modulus which strongly depends on the distance to

the jamming transition, and *(iii)* evidence for a yield stress which vanishes at the jamming transition.

O'Hern et al. [13, 21] studied the elastic properties of these systems in detail in their seminal work on jamming: in their model, the particles are frictionless, i.e., there are no viscous interactions, and the only interactions between particles are repulsive contact forces. By and large, we use the same model of bubble interactions in chapters 2 and 3. We will shortly discuss the ingredients of the model here, and will discuss it in more detail in § 2.2.

These systems of frictionless soft particles consist of circles with a simple pairwise interaction under periodic boundary conditions at a fixed volume. The interactions between particle i and j are a simple power law $U_{ij} \sim \delta_{ij}^{\alpha}$, where δ_{ij} is the overlap between particles, as sketched in Fig. 1.3(a). The power α tunes the interaction: for harmonic particles, i.e., where the interactions act like one-sided linear springs, $\alpha = 2$. For Hertzian interactions, typical of grains in 3D, $\alpha = 2.5$ [48]. For foam bubbles in the geometry used in chapter 3, the power $\alpha \approx 2.1$ for small overlaps [49–51]. In our simulation chapters, we will consistently use harmonic interactions, i.e., $\alpha = 2$.

These ingredients are sufficient to uncover a wealth of insights into the behavior of soft disordered materials. For this thesis, the most important of these is the shear modulus G: how easy is it to change the shape of a system? The shear modulus depends on the distance to jamming $\Delta\phi = \phi - \phi_c$ and the interaction parameter α: $G \sim \Delta\phi^{\alpha-1.5}$ [3, 13, 22, 23, 34]. For harmonic interactions, this means $G \sim \sqrt{\Delta\phi}$. However, G is typically calculated for infinitesimal deformations, and the range for which linear response is valid is not known.

In chapter 2, we probe the first deviations from this strict linear elastic response. Our approach follows from the work of Ellenbroek et al. [32]. They showed that, in systems with harmonic interactions, the *value* of the overlap is irrelevant for the elastic response. In other words, the elastic response is defined by the *contact network*, i.e., which particles are in contact and which ones are not. This, then, implies that the elastic behavior will change once the contact network changes. We will therefore investigate when the first change in the contact network occurs, and what effect that change has on the elastic response.

Finally, we focus on what happens after the initial elastic regime. Maloney and Lemaître [52] investigated behavior of the same soft sphere systems under large deformations, and show the behavior is a combination of smooth elastic segments and abrupt plastic stress drops. Other work has, for example, focused on fluctuations in continuous shear [38, 41, 53]. In chapter 3, we will focus on the first sign of plasticity in sheared systems. How can we define plasticity on a microscopic level? Does a system always become irreversible after a plastic event? Can we have irreversibility without plasticity? We will propose a framework for answering these questions, and will show preliminary results.

1.2 Foams

In this section, we focus on existing work on foam experiments. This will provide context for chapter 4, where we probe the behavior of a two-dimensional foam under shear, while varying the packing density.

The behavior of foams under shear has been a subject of significant attention. In contrast to simulations, where most work focuses on the static properties of the packing, foam experiments typically focus on the question of macroscopic flow (rheology). For example, one can wonder about the behavior under continuous shear, [54], cyclic shear [55] or extensional flow [56], investigate the microscopic behavior of the foam films [57] or the effects of chemical composition of the surfactant [58]. These typically focus on the behavior of so-called 'dry' foams, which are highly compressed. The behavior of foam at lower densities has, for example, been studied by Katgert et al. [39], who researched the rate dependent behavior for a low-density foam.

Katgert and van Hecke [26] also measured the *static* properties of foams in detail. They *(i)* determined a relationship between the experimental packing fraction, i.e., the ratio of foam area and total area, and the theoretical packing fraction, which is the ratio of the *undeformed* foam area and total area; *(ii)* confirmed the scaling relationship between the average contact number z and ϕ found in simulations, and *(iii)* found force distributions comparable to those found in experiments. Later, Miedema et al. [49] investigated the scaling of individual bubble interactions, and Siemens [59] measured the jamming transition experimentally. Recent work has shown

that emulsions are also excellently suited for this kind of research, and finds comparable results [60–64].

In chapter 4, we will use a bi-axial compression and shear setup to probe the microscopic behavior of foams under shear deformations. In this setup, we can independently change the packing density ϕ and the shear strain γ, which we use to measure the behavior of the foam at a wide range of densities. We find a smooth transition from behavior dominated by global non-affine motion at low densities to behavior dominated by localized rearrangements at high densities.

CHAPTER 2

CONTACT CHANGES OF SHEARED SYSTEMS

Work presented in this chapter has been published in:

[65] Merlijn S. van Deen, Johannes Simon, Zorana Zeravcic, Simon Dagois-Bohy, Brian P. Tighe, and Martin van Hecke, *Contact Changes near jamming*, Phys. Rev. E **90**: 020202(R) (2014). doi:10.1103/PhysRevE.90.020202

and has been submitted to Phys. Rev. E as:

[66] Merlijn S. van Deen, Brian P. Tighe, and Martin van Hecke, *Contact Changes of Sheared Systems: Scaling, Correlations, and Mechanisms*, arXiv:1606.04799

In this chapter, we investigate contact changes in amorphous, athermal, frictionless particle packings under small shear deformations by means of numerical simulations. We focus on the first contact change, as this is where one expects the first significant deviation from strictly linear response. We will establish a scaling relation between the mean strain at which the first contact change happens and the system size and pressure, and find that this strain can accurately be predicted from linear response. We will investigate the effect of a single contact change on the elastic response, and will show that, although *strict* linear response is no longer valid after a single contact change, the response is still *effectively* linear in the thermodynamic limit. We discuss the underlying microscopic mechanism for contact changes, and reveal subtle correlations between particle motions and overlap, as well as between subsequent contact changes. Finally, we discuss our findings in the light of several recent related studies of contact changes.

2.1 Introduction

The focus of this chapter is on the first contact change in systems under shear deformation. Earlier work on sheared systems has mostly focused on plasticity [52, 67–71], continuous shear [38, 41, 42, 72] or on the linear response limit [21, 34, 73–75] while earlier work on contact changes has focused on vibrations [76–78] or hard particle systems [79, 80]. We instead focus on soft particle systems, as they are descriptive for a wider range of experimentally relevant systems, and focus on experimentally relevant simple shear deformations.

The outline of this chapter is as follows. In § 2.2, we will describe the preparation and deformation of our systems. We focus on the strain at which the first contact change happens in §§ 2.3 and 2.4, and investigate multiple contact changes and the behavior in the thermodynamic limit in § 2.5. Finally, we compare our results to earlier work in § 2.6.

2.2 Method & protocols

For our simulations, we use the standard frictionless soft sphere model [13, 21], which is a simplified version of the viscous model for foam bubbles introduced by Durian [22]. We will shear quasi-statically, so only the elastic interactions between particles are taken into account - there is no inertia, nor is there viscous damping. We will focus on so-called $\varepsilon^{+}_{\text{all}}$ packings [28] that have a positive bulk and shear modulus, as well as zero residual shear stress. This is not guaranteed for a square unit cell [28, 34, 81], and we therefore allow the shape of the cell to change.

In this section, we will describe the precise implementation of the periodic boundaries, the particle interactions and the energy minimization algorithms. Finally, we will describe how we apply a simple shear deformation and how we find individual contact changes.

Boundary conditions. We use periodic boundaries, as this removes the need to model wall-particle interactions. Instead, particles just interact with their neighbors, which may be periodic copies of particles on the other side of the unit cell.

In a periodic system, each particle has periodic copies at

$$\vec{r} = \vec{r_i} + n_x \cdot \overrightarrow{L_x} + n_y \cdot \overrightarrow{L_y}\,, \tag{2.1}$$

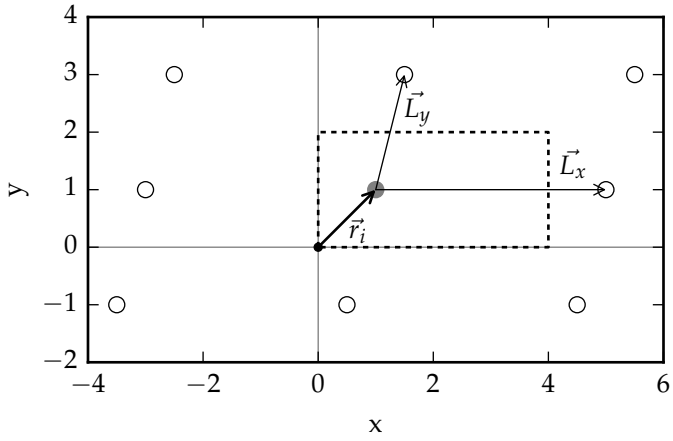

FIGURE 2.1: A particle with canonical position $\vec{r_i} = (1, 1)$ (filled circle) and its periodic copies (circles) in a system with $\overrightarrow{L_x} = (4, 0)$ and $\overrightarrow{L_y} = (\frac{1}{2}, 2)$ ($L^2 = 8$, $\alpha = \frac{1}{8}$ and $\delta = \frac{1}{\sqrt{2}} - 1$). The canonical copy falls within the rectangular unit cell $(0, 0), (4, 2)$ indicated with a dashed line.

where n_x and n_y are integers and $\overrightarrow{L_x} = (L_{xx}, L_{xy})$ and $\overrightarrow{L_y} = (L_{yx}, L_{yy})$ are two vectors that describe the periodic boundaries (Fig. 2.1). $\vec{r_i}$ is the canonical position of the particle, which falls within the rectangular *unit cell* $(0, 0), (L_{xx}, L_{yy})$.

The area of the unit cell is given by

$$L^2 = L_{xx} \cdot L_{yy} \,, \tag{2.2}$$

where L_{xx} and L_{yy} will have closely similar, but not necessarily strictly equal values. The shear is described using a simple shear (Lees-Edwards) parameter

$$\alpha = L_{yx}/L \tag{2.3}$$

and a pure shear (i.e., aspect ratio) parameter

$$\delta = \frac{L_{yy} - L}{L} = \sqrt{L_{yy}/L_{xx}} - 1 \,. \tag{2.4}$$

Traditionally, the unit cell is square, i.e., $\overrightarrow{L_x} = (L, 0)$ and $\overrightarrow{L_y} = (0, L)$, and consequently $\alpha = \delta = 0$ [3, 13, 21], but this leads to systems that are

stable to compression but potentially unstable to shear [28, 34, 81, 82]. In contrast, here we require that the energy is also at a minimum with respect to these degrees of freedom, which guarantees that the shear modulus is positive and that the residual shear stresses are zero [28, 34], as one expects for a physical system at rest. We keep $L_{xy} = 0$ fixed, which fixes the global rotational degree of freedom.

Particles and their interactions. Our system consists of circular particles with repulsive harmonic interactions. We use a bi-disperse mixture, with $N/2$ small particles with $R_s = 1$ and $N/2$ large particles with radius $R_l = 1.4$, to prevent crystallization [3, 21, 137].

The interaction between particles is determined by their overlap

$$\delta_{ij} = \begin{cases} R_i + R_j - |\vec{r_{ij}}| & \text{if } |\vec{r_{ij}}| < R_i + R_j, \\ 0 & \text{otherwise.} \end{cases} \tag{2.5}$$

where $|\vec{r_{ij}}|$ is the distance between particles i and j (Fig. 1.3(a)). Because of the periodic boundaries, this distance is not uniquely defined. The physically relevant value is the *minimum* distance, so we will define the distance as

$$|\vec{r_{ij}}| \equiv \min_{n_x, n_y} \left| [\vec{r_i} - \vec{r_j}] + [n_x \cdot \vec{L_x}] + [n_y \cdot \vec{L_y}] \right|, \tag{2.6}$$

where $\vec{r_i}$ and $\vec{r_j}$ are the canonical particle positions. $n_{x,ij}$ ($n_{y,ij}$) is 0 if the closest copy of j to i is the canonical copy, $+1$ if it is across the right (top) boundary and -1 if it is across the left (bottom) boundary. Contact forces have magnitude $f_{ij} = k\delta_{ij}$, where $k = 1$ is the spring constant, and correspond to the harmonic potential

$$U_{ij} = \frac{k}{2}\delta_{ij}^2 . \tag{2.7}$$

Energy, enthalpy and stresses. From the particle interactions, we can now define the macroscopic state variables. First, we have the internal energy, which is given by the sum of all inter-particle potentials,

$$U = \sum_{i,j} U_{ij} = \sum_{i,j} \frac{k}{2}\delta_{ij}^2 , \tag{2.8}$$

where the sum runs over all particle pairs.

The enthalpy is then given by

$$H = U + P_{\text{ext}} L^2 \,, \tag{2.9}$$

where P_{ext} represents the external pressure on the system.

Finally, we have the boundary stresses: the simple shear stress

$$\sigma_{yx} = \sigma_{xy} \,, \tag{2.10}$$

the deviatoric (pure shear) stress

$$\tau = \frac{1}{2}\left(\sigma_{xx} - \sigma_{yy}\right) \,, \tag{2.11}$$

and the volumetric stress or internal pressure

$$P_{\text{int}} = \frac{1}{2}\left(\sigma_{xx} + \sigma_{yy}\right) \,. \tag{2.12}$$

These are computed using the Born-Huang approximation [83, 84]:

$$\sigma_{ab} = \frac{1}{2L^2} \sum_{i,j} \left[(\vec{r_{ij}} \cdot \hat{a})(\vec{f_{ij}} \cdot \hat{b}) \right] \tag{2.13}$$

where $a, b \in \{x, y\}$ and the sum is over all particle pairs i, j.

Units. The small particle radius R_s and the spring constant k set all units in our system. The length scale is given by the small particle radius R_s, the stress scale is given by the spring constant k and energy is measured in units of kR_s^2.

Preparing a packing. We will now focus on creating a stable packing of particles. Starting with N randomly positioned particles and a predefined external pressure P_{ext} between 10^{-7} and 10^{-2}, we minimize the enthalpy until we end up in a stable state, where the forces on particles and boundaries add up to zero.

We start by placing $N/2$ small particles with $R_s = 1$ and $N/2$ large particles with radius $R_l = 1.4$ at random positions $\vec{r_i}$ within a square box of size

$$L_{\text{init}}^2 = \phi_{\text{init}} \left(\frac{N}{2} \pi R_s^2 + \frac{N}{2} \pi R_l^2 \right) \,, \tag{2.14}$$

where $\phi_{\text{init}} \equiv 0.8$ is chosen to be far below the jamming density $\phi_J \approx 0.84$. We use a combination of the Conjugate Gradient method [85] and the Fast Inertial Relaxation Engine (FIRE) [86] algorithms. The latter is much faster, but becomes unstable when the overlaps between particles are large. We therefore first use the Conjugate Gradient method to resolve the largest overlaps. We keep the boundaries fixed, and minimize the energy until

$$|\Delta U| \leq 10^{-2} \cdot U \, . \tag{2.15}$$

After the large overlaps are resolved, we can safely switch to the FIRE algorithm. We now also allow the boundaries (i.e., L_{xx}, L_{yy}, and L_{yx}) to deform. We relax the system until we reach a state where

$$\begin{aligned} |\Delta H| &\leq 10^{-17} \cdot H \, , \text{ and} \\ |\sigma_{yx}| &\leq 10^{-15} \, . \end{aligned} \tag{2.16}$$

The resulting state has positive shear moduli, vanishingly small shear stresses, and a pressure given by the target pressure P_{ext}.

Simple shear. We are interested in the response to an applied simple shear deformation. We do this by moving the boundaries into a new state

$$\begin{aligned} \overrightarrow{L_x}(\gamma) &= \overrightarrow{L_x}(0) \, , \\ \overrightarrow{L_y}(\gamma) &= \overrightarrow{L_y}(0) + \gamma L \cdot \hat{x} \, , \end{aligned} \tag{2.17}$$

i.e., we change $\alpha \to \alpha + \gamma$, while keeping L^2 and δ constant. The system is now no longer in an enthalpy minimum, so we relax the system, using the FIRE algorithm, but keeping boundaries in the new deformed state. We relax the system until

$$|\Delta H| < 10^{-13} \cdot H \, , \tag{2.18}$$

where we sacrifice a small error in the particle positions for simulation speed. This is accurate enough to detect contact changes and to determine the behavior of stress and energy at the contact change. We find the details of the relaxation requirement do not influence the detection of contact changes, and the *relative* error in σ_{xy} is typically less than 10^{-6}. An example of the resulting particle displacement is shown in Fig. 2.2.

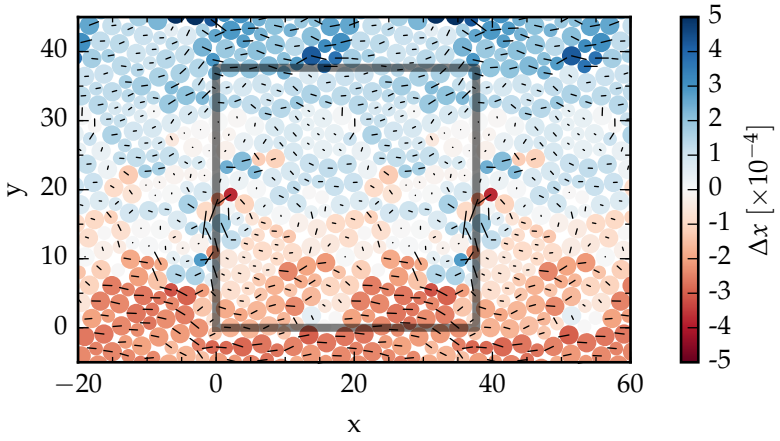

FIGURE 2.2: Particle trajectories in response to a simple shear strain $\gamma = 9.8 \times 10^{-6}$, for the $N = 256$ particle system at $P = 10^{-6}$. Lines indicate displacements (magnified $\times 5000$), color indicates displacement parallel to the applied shear. The unit cell is slightly non-square and marked as a gray box.

The corresponding stress and enthalpy response is shown in Figs. 2.3(c) and 2.3(d).

To detect contact changes, we apply a strain, relax the system, and compare the new overlaps of each particle pair i, j to the initial state, until we detect a change in the contact network ($\delta_{ij} = 0 \leftrightarrow \delta_{ij} > 0$ for any pair i, j). We then use the bisection method to find the contact change strain: we move back to the last state before the contact change, and test a strain between the last known state before and the first state after the contact change. Specifically, we initially apply a strain

$$\gamma = 10^{-9} \cdot 10^{\zeta} \tag{2.19}$$

where we increase $\zeta = 0, 1, \ldots$ until we find that the contact network changed. We then bisect ζ until we have determined the strain at the contact change γ_* up to $\Delta\gamma/\gamma_* < 10^{-6}$, as shown in Figs. 2.3(a) and 2.3(b).

Treatment of rattlers. Rattlers are always a special case in simulations: because they are free to move, their behavior is ill-defined. In our simulations, we encounter rattlers in two distinct ways: first, a particle with three contacts can become a rattler. Because of force balance, all three contacts go to

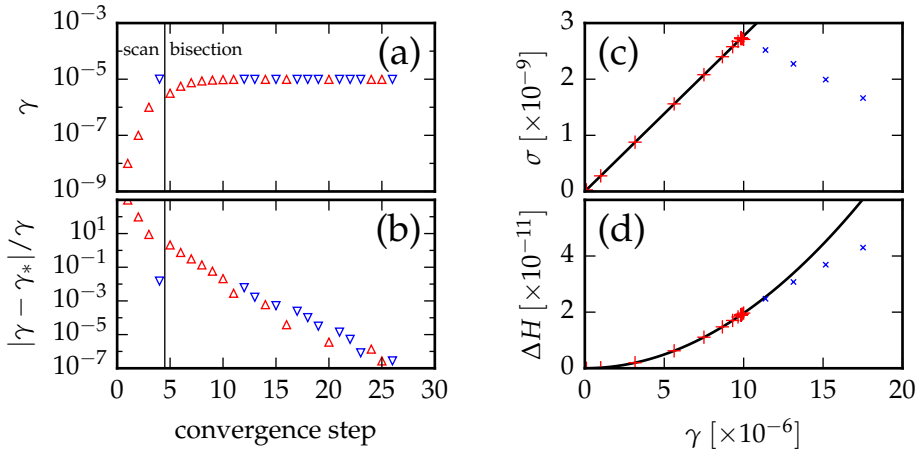

FIGURE 2.3: Convergence to the first contact change for the system shown in Fig. 2.2 ($N = 256$, $P = 10^{-6}$). (a) Contact change detection algorithm. Red $\triangle$ indicate states without a contact change ($\gamma < \gamma_*$), blue $\triangledown$ states have had at least one contact change ($\gamma > \gamma_*$). We rapidly scan shear space until we find a state with a changed contact network (step 4). We then bisect the strain space to determine γ_*. (b) The bisection algorithm continues until $\Delta\gamma/\gamma_* < 10^{-6}$. (c) The stress response before the first contact change (red pluses) is linear as a function of γ. After the contact change (blue crosses) the response changes drastically. (d) The enthalpy change during deformation. Because of the linear stress response, the enthalpy change is quadratic in γ.

zero overlap together. This is detected correctly in our simulations, and the event is recorded as a *single* event in which three contacts are lost (Fig. 2.4).

The case of a rattler becoming part of the load-bearing network is different. Before the rattler gains three contacts, it's fully free to move, and we can therefore not determine the strain at which it becomes part of the network again accurately — if another algorithm had been used, the path of the particle and therefore also the joining strain could be different. We will therefore not include these contact making events in our analysis of the first contact change.

One might worry that this biases the mean strain and the statistics of breaking or closing a contact. Indeed, we find that, in our simulations, contact changes in which a rattler annihilates happen at a relatively small strain (typically $50 - 80\%$ of the mean strain). At the same time, these events

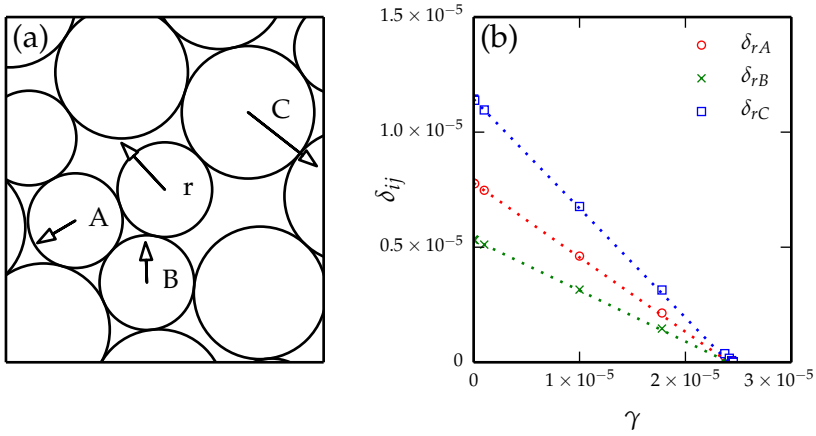

FIGURE 2.4: (a) Zoom-in of a packing where particle r becomes a rattler after the first contact change ($N = 22$, $P = 1.5 \cdot 10^{-5}$). Neighboring particles A, B and C are indicated. (b) Overlap of r with the neighboring particles A, B and C as a function of strain γ. Symbols are our results from simulations, while the lines indicate predictions using linear response. The simulation finds $\gamma_*^{\mathrm{DNS}} = 2.45 \cdot 10^{-5}$, while linear response predicts $\gamma_*^{\mathrm{LR}} = 2.41 \cdot 10^{-5}$.

are rare: We find they are most prevalent in large systems at intermediate pressures, but even there they only make up a few percent of the events. We find that the overall effect on the mean strain is also limited to a few percent, while we measure changes in the mean strain over multiple orders of magnitude. The probability of the first contact being a contact making event decreases somewhat, as 5–15% of making events involve a rattler re-joining the contact network. Because we are interested in the scaling behavior, we are comfortable ignoring these events.

Simulation range. As we will study changes in individual contacts, and in particular probe the strain at which the first contact change takes place, we anticipate that we need to study finite size effects, i.e. the role of the number of particles N in tandem with the role of the pressure P. Moreover, we anticipate that many quantities will rescale with N^2P [28, 33, 65]. We have therefore prepared various *ensembles* — groups of sheared systems with the same number of particles and pressure. Most ensembles contain 100

systems; some larger ensembles contain up to 5000 systems. The following ensembles were prepared:

- To characterize the behavior at the first contact change, we created a set of ensembles having N and P on a log-spaced grid, with $N = 16, 32, \ldots, 1024$ and $P = 10^{-7}, 10^{-6\frac{5}{6}}, \ldots 10^{-2}$, and a set at intermediate $N = 22, 45, \ldots 724$ for $P = 10^{-2}$ and 10^{-7}. These are sheared until we find at least one contact change.

- To characterize the effects of multiple contact changes (§ 2.5.2), we sheared the ensembles at $N = 16$, $P = 10^{-6}$, $N = 1024$, $P = 10^{-6}$ and $N = 1024$, $P = 10^{-2}$ up to 25 contact changes.

- To investigate anisotropy, ensembles with $N = 16, 256, 1024$ particles at $P = 10^{-3}$ and $N = 16$, $P = 10^{-6}$ were sheared in the inverse direction.

2.3 Numerical results

In this section, we will first discuss at which strain γ_* the first contact change occurs, the relative prevalence of making or breaking a contact, and the anisotropy in the type of events. We will then discuss the distribution of γ_* within an ensemble at fixed N and P, and will discuss how the ensemble average $\gamma_{cc} = \langle \gamma_* \rangle$ scales with N and P.

2.3.1 The first contact change

For each packing in an (N, P) ensemble, we determine the strain of the first contact change γ_*, as described in § 2.2. Within a single ensemble, typically consisting of 100 realizations, we find that γ_* can vary over three orders of magnitude. In Fig. 2.5(a) we show the cumulative distribution function (CDF) of γ_* for $N = 256$ ensembles at various pressures. We observe two important properties: First, the typical scale of the strain γ_* increases with pressure P. Second, we find that, although the distributions are wide, their shape is mostly independent of P. In § 2.3.2, we will take a detailed look at these distributions and their scaling.

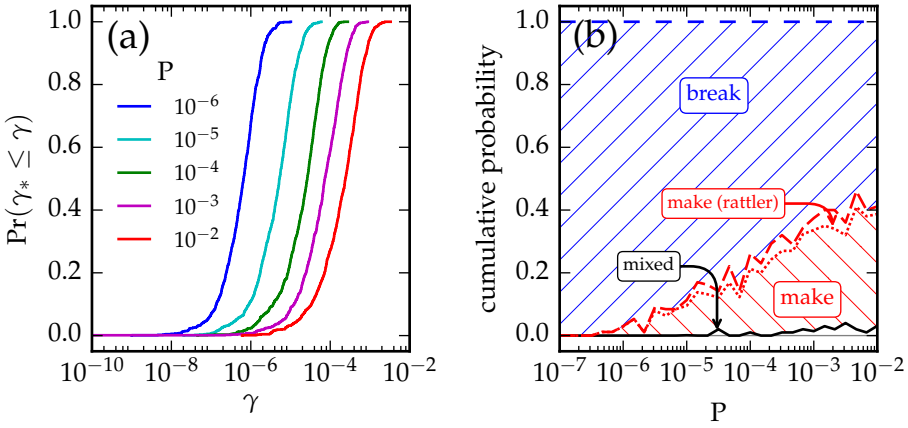

FIGURE 2.5: (a) Cumulative distribution functions (CDF) $\Pr(\gamma_* < \gamma)$ of the contact change strain γ_* for ensembles with $N = 256$ particles at various pressures. The horizontal shift between curves shows that the characteristic strain increases with P. (b) Stacked probabilities for the first contact change being a break event (blue striped), a make event (red striped), a make event involving rattlers (red) or a mixed event, where contacts are both broken and created (black), again for $N = 256$ ensembles. A small amount of new contacts involve a rattler becoming part of the contact network. At low pressures, all contact changes involve a contact being broken. The probability of the contact change being a new contact increases with pressure, up to 40% at $P = 10^{-2}$. Both mixed events and new contacts involving a rattler are very rare.

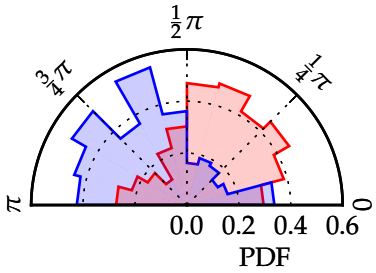

FIGURE 2.6: Radial distribution function $\rho(\theta)$ of the contact orientation for making (blue) and breaking (red) events, for $N = 256$, $P = 10^{-3}$. New contacts are created along $\theta = 3\pi/4$, while contacts are broken along $\theta = \pi/4$.

Making and breaking. In Fig. 2.5(b), we show a stacked probability graph of the different contact change types. We distinguish events where one or more contacts are broken (*break*), events where one or more contacts are created (*make*) and events where contacts are both broken and created (*mixed*). Within the *make* class, we can distinguish events where a particle which originally was a rattler now becomes part of the contact network (*make (rattler)*).

At low pressures, we find that the vast majority of events consists of contacts being broken. This probability decreases with increasing pressure, to 59% at $P = 10^{-2}$. At this pressure, we find that 38% of events create a new contact. In § 2.4.4, we will show how these probabilities vary as a function of N^2P.

Of all *make* events, $5 - 15\%$ involve rattlers. This is consistent between ensembles, with no clear dependence on either N or P. Finally, the number of mixed events increases with pressure, but is $< 5\%$, independent of N.

In the following sections, we will focus on the simple *make* and *break* cases; we will not include *make (rattler)* or *mixed* events. We remove the first because the behavior of rattlers creating new contacts is ill-defined, as discussed in § 2.2. Mixed events are not included because of their relative scarcity.

Anisotropy in bond direction. When we shear our system, we expect anisotropy to build up [87]. We measure the anisotropy by measuring the contact orientation θ for each contact that is created or broken. θ characterizes the direction for the connection vector $\vec{r_{ij}}$ between the two particles, and is π-periodic.

A simple shear deformation along the x ($\theta = 0$) axis compresses the system along $\theta \approx \frac{3}{4}\pi$ and extends it along $\theta \approx \frac{1}{4}\pi$. We therefore expect breaking contacts to cluster around $\theta \approx \frac{1}{4}\pi$, while new contacts should cluster around $\theta \approx \frac{3}{4}\pi$.

In Fig. 2.6 we show the resulting radial distribution function $\rho(\theta)$ for broken and created contacts. We indeed observe the majority of making events have $\frac{1}{2}\pi \leq \theta < \pi$, while the majority of breaking events have $0 \leq \theta < \frac{1}{2}\pi$. This shows that anisotropy is relevant already at the first contact change.

	$\gamma\uparrow$ bk	$\gamma\uparrow$ mk	***total***	$\mathbf{Pr}(\gamma\uparrow \text{bk}\|\cdot)$
$\gamma\downarrow$ bk	412	239	*651*	0.63
$\gamma\downarrow$ mk	198	129	*327*	0.61
total	*610*	*368*	978	

TABLE 2.1: Relative prevalence of making and breaking under forward and backward shear strain for $N = 256$, $P = 10^{-3}$.

Anisotropy in making and breaking. Finally, we investigated whether the type of contact change and the direction of shear are correlated: If we break a contact when we shear a packing in the forwards direction, are we more likely to *make* a contact when we shear in the *backwards* direction, and vice versa? To test this, we have determined the prevalence for making and breaking under forward ($\gamma\uparrow$) and backward ($\gamma\downarrow$) shear for an ensemble of 978 packings at $N = 256$ and $P = 10^{-3}$. In Table 2.1, we show counts of the four possible combinations of making and breaking under forward and backward shear. Our data supports the notion that the type of contact changes in one shear direction is uncorrelated to the type in the other direction. For example, $\Pr(\gamma\uparrow \text{bk}|\gamma\downarrow \text{bk}) \approx \Pr(\gamma\uparrow \text{bk}|\gamma\downarrow \text{mk}) \approx 0.62$.

More formally, we calculated the Pearson's chi-square statistic,

$$\chi^2 = \sum (O - E)^2 / E \tag{2.20}$$

where the sum runs over all four observations O, and E is the expected number of observations in the case of independence, e.g.,

$$O_{\text{bk,bk}} = 412\,, \tag{2.21}$$

$$E_{\text{bk,bk}} = 978 \cdot \Pr(\gamma\uparrow \text{bk}) \cdot \Pr(\gamma\downarrow \text{bk}) = 406.0\,, \tag{2.22}$$

and find $\chi^2 = 0.689$. The cutoff typically used for significant deviations ($p = 0.05$, 1 degree of freedom) is $\chi^2 > \chi^2_{.05} = 3.841$. We find $\chi^2 \ll \chi^2_{.05}$, supporting our observation of independence.

2.3.2 Strain distributions

We will now take a more detailed look at the distribution of the strain at the first contact change, to show that contact changes can essentially be

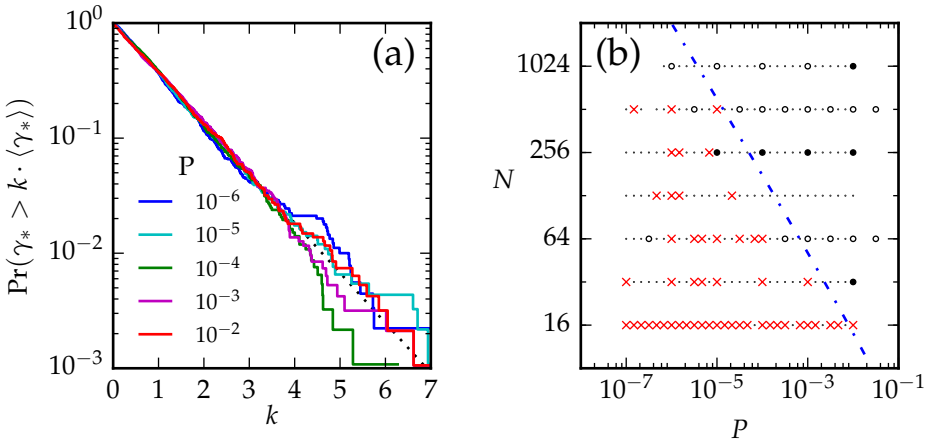

FIGURE 2.7: (a) Rescaled complementary cumulative distribution functions (CCDF) for the same data as in Fig. 2.5(a). The dotted line gives the CCDF for an exponential distribution. (b) Result of the Anderson-Darling test on each ensemble. Ensembles where the null hypothesis "these values of γ_* were drawn from an exponential distribution" was rejected are indicated with a red $\times$. Other ensembles are indicated with a black $\cdot$ (≤ 100 samples), $\circ$ ($100 - 1000$ samples) or $\bullet$ (≥ 1000 samples). The blue dot-dashed line indicates the finite size threshold $N^2 P \ \log(N)^{-0.7} = 1$ (see § 2.3.3)

described as a Poisson process. For large systems, the shape of the CDF closely resembles that of an exponential distribution, whose CDF is given by

$$\Pr(\gamma_* \leq \gamma) = \begin{cases} 1 - e^{-\gamma/\beta} & (\gamma \geq 0), \\ 0 & (\gamma < 0), \end{cases} \tag{2.23}$$

where β is the mean of the distribution. To emphasize the resemblance between our numerical distributions and the exponential distribution, we show *complementary* CDFs (tail distributions) of γ_*, rescaled by the ensemble mean $\langle\gamma_*\rangle$, i.e. $\Pr(\gamma_* \geq k \cdot \langle\gamma_*\rangle)$. For an exponential distribution, the CCDF is thus given by

$$\Pr(\gamma_* > k \cdot \langle\gamma_*\rangle) = e^{-k} \quad (k \geq 0), \tag{2.24}$$

In Fig. 2.7(a) we plot the rescaled CCDFs for an exponential distribution (dotted black curve) and for our simulation data (colored curves), and we find our data indeed closely corresponds to an exponential distribution.

As a formal means of checking conformance to an exponential distribution, we used the *Anderson-Darling test* [88, §1.3.5.14], with which we test the hypothesis "these values of γ_* were drawn from an exponential distribution". We use a 5% confidence interval, i.e., there is a 5% probability we reject the hypothesis for samples that *were* drawn from an exponential distribution.

In Fig. 2.7(b), we graphically show the results of the test. For $N = 256$, we observe the distributions at $P \geq 10^{-5}$ are indistinguishable from an exponential distribution. This is consistent with a Poisson process, where contact changes are independent of each other.

Nevertheless, we observe deviations for small systems and low pressures. This is not surprising: it seems unlikely for contact changes to be independent of each other if there are only a limited number of contacts. The boundary between rejection and non-rejection corresponds to the transition to extended systems for $N^2P\ \log_{10}(N)^{-0.7} > 1$ [28, 34], indicated with a blue curve (§ 2.3.3).

Note that the $N^2P\ \log_{10}(N)^{-0.7} < 1$ region also includes many ensembles where the hypothesis is *not* rejected. This does not, however, imply the data set has been drawn from an exponential distribution; it merely indicates the data is indistinguishable from a set drawn from an exponential distribution. In these cases, we are dealing with small sample sizes (≤ 100 samples), which makes it hard to distinguish the measured distribution from that of an exponential distribution.

For larger sample sizes, this explanation is no longer satisfactory, and taking the underlying distribution to be exponential is a more reasonable interpretation. We observe that large ensembles where the hypothesis was not rejected all have $N^2P\ \log_{10}(N)^{-0.7} \gg 1$. We conclude that the transition to extended systems also governs where the distribution of γ_{cc} is well-described by an exponential distribution and, therefore, where the contact breaking is a Poisson process.

We can now inspect what kind of distribution describes small systems at low pressures. In Fig. 2.8(a), we show rescaled CCDFs for $N = 16$ systems at various pressures, and notice clear deviations from exponential. The most significant deviation is at low k, where we find $\Pr(\gamma_* > k \cdot \langle\gamma_*\rangle)$ is

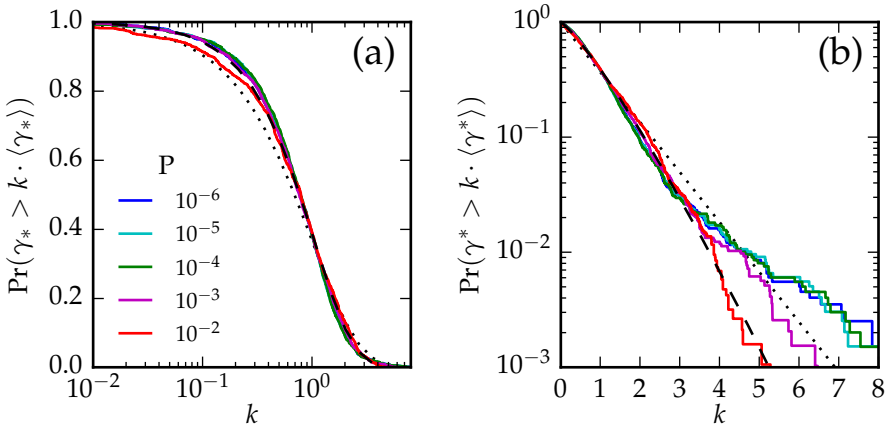

FIGURE 2.8: (a) Rescaled complementary cumulative distribution functions (CCDF) for $N = 16$ systems at various pressures, on log k and linear Pr axes. The dotted line gives the CCDF for an exponential distribution, while the dashed line gives the CCDF for a Weibull distribution with shape $c = 1.2$. For most of the curve, the Weibull distribution matches the data well. (b) Same as (a), on linear k and log Pr axes. For high k, neither the exponential nor the Weibull distribution matches the data well.

larger than expected for an exponential distribution. As $\Pr(\gamma_* > k \cdot \langle\gamma_*\rangle)$ is the *survival probability*, this indicates a lack of events at small strain. At higher pressures, this effect seems to disappear. In Fig. 2.8(b), we show the same data, but now focusing on the behavior at large k.

As an alternative to an exponential distributions, we fit a Weibull distribution to our data. Whereas the exponential distribution describes the amount of strain before failure if the failure rate h (number of events per unit strain) is constant, the Weibull distribution describes the strain before failure if the failure rate depends on the applied strain as $h \sim \gamma^{c-1}$. The CDF of the distribution is given by

$$\Pr(\gamma_* \leq \gamma) = \begin{cases} 1 - e^{(-\gamma/\lambda)^c} & (\gamma \geq 0), \\ 0 & (\gamma < 0), \end{cases} \tag{2.25}$$

where λ determines the scale, and c the shape of the distribution. The mean is given by $\langle\gamma_*\rangle\lambda\Gamma(1 + 1/c)$ [89], where Γ is the gamma function. The

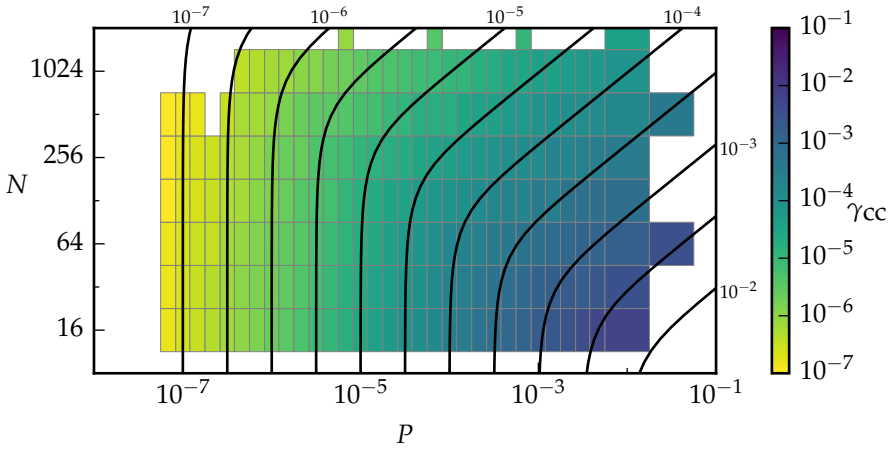

FIGURE 2.9: Color map of γ_{cc} as a function of N and P. The inset curves have constant γ_{cc}, as indicated by the values at the edge. The shape is based on the scaling discussed in § 2.3.3.

rescaled complementary distribution is thus given by

$$\Pr(\gamma_* > k \cdot \langle \gamma_* \rangle) = e^{(-k/\Gamma(1+1/c))^c} \quad (k \geq 0). \tag{2.26}$$

Using maximum likelihood estimation, we fit our data to a Weibull distribution, and find $c \approx 1.2$ for $P \leq 10^{-3}$. In Fig. 2.8(a), we find this gives a much better fit to the data than an exponential distribution. To interpret this, when $c > 1$, the distribution is skewed to higher values of k, as the failure rate $h \sim k^{c-1}$ increases with k. We find relatively few values at low k and relatively many values at high k — hence events at small strain are suppressed.

2.3.3 Scaling

We now discuss the variation of the mean contact change strain $\gamma_{cc} = \langle \gamma_* \rangle$ with N and P. Even when the distributions are not purely exponential, their mean is well-defined. We have also seen that γ_{cc} depends on P. What kind of scaling for γ_{cc} with N and P should we expect?

In Fig. 2.9, we show γ_{cc} as function of both pressure and system size. The data suggests that there are two regimes: one where γ_{cc} depends solely on pressure and not on packing size, and a second regime where γ_{cc}

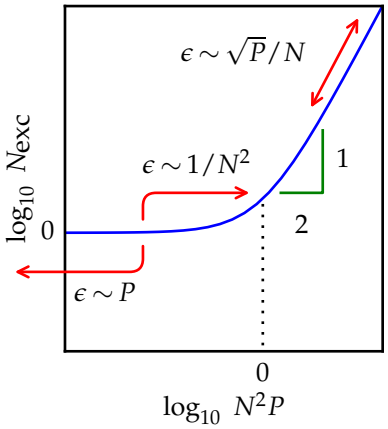

FIGURE 2.10: Excess number of contacts $N_{\text{exc}} = N\Delta z/2$ as a function of N^2P (blue curve, based on [28, 33, 34]). Arrows indicate volumetric strains corresponding to a single contact change.

depends on both. We observe γ_{cc} increases with pressure in both regimes, but decreases with increasing packing size in the second regime. This is not unexpected: contacts are easier to break if the confining pressure is small, and if there are more contacts, you are more likely to encounter a single weak contact.

In the following subsections, we will introduce two closely related scaling arguments, which both lead to the same prediction for the relation between γ_* and N and P: a direct argument for *compressive* strain and a stress-based argument for shear strain. We will then compare the predicted scalings to our computational data.

Compression. We start with a compressional argument, based on estimating the strain scale for making and breaking a contact under compression. There is a clear relationship between compression and the number of contacts: we gain contacts if we compress the system and we lose contacts if we expand the system. The scaling that relates the excess contact number $N_{\text{exc}} = \Delta z/2$ to N and P is well-known from earlier work [28, 33, 34], and is shown in Fig. 2.10. There are two branches: a plateau $N_{\text{exc}} \sim 1$ at low

pressures and a square root pressure dependence $N_{\text{exc}} \sim \sqrt{N^2 P}$ at higher pressures.

How far do we need to expand or compress a system at given N and P to induce a contact change? In the high-pressure regime, we can take the derivative $\pm\frac{\partial}{\partial P}\left(\sqrt{N^2 P}\right) \sim \pm N/\sqrt{P}$, which gives us the number of contacts changed due to unit pressure change. Its inverse, $\delta P \sim \pm\sqrt{P}/N$, then gives us the pressure change needed for a single contact change. The compressional strain is the pressure change divided by the bulk modulus K: $\varepsilon_{\text{cc}} \sim \pm\delta P/K$. As K is independent of N and P [21], we simply find $\varepsilon_{\text{cc}} \sim \pm\sqrt{P}/N$.

In the low-pressure finite size regime, the number of contacts is independent of pressure. Can we then still determine the pressure change required for a contact change? We can, because the plateau has a finite length. On the one hand, the plateau ends at $P = 0$, as we unjam our system and lose all contacts. On the other hand, the plateau ends when we enter the large system size regime at $N^2 P \sim 1$ and gain one new contact.

The scales for making and breaking a contact are thus no longer the same in the finite size regime: To break a contact, we unjam the system by reducing the pressure with $\delta P \sim P$, and we find $\varepsilon_{\text{bk}} \sim -P$. To create a contact, we increase pressure up to the beginning of the large system regime, at $P_{\text{target}} = 1/N^2$. As we are initially in the small system regime, the current pressure $P \ll 1/N^2$ and can be neglected, and the pressure change $\delta P = P_{\text{target}} - P \approx -1/N^2$. We thus need to apply a strain $\varepsilon_{\text{mk}} \sim -1/N^2$. The contact *change* strain will be given by the minimum of the absolute making and breaking strains. As $P \ll 1/N^2$, we thus expect $\varepsilon^{\text{cc}} \sim P$.

Summarized, this argument leads to these characteristic strains for contact changes under compression:

$$\varepsilon \sim \begin{cases} \begin{matrix} \varepsilon_{\text{bk}} & \varepsilon_{\text{mk}} & \varepsilon_{\text{cc}} \end{matrix} & \\ \begin{matrix} -P & 1/N^2 & P \end{matrix} & \text{for } N^2 P \ll 1, \\ \begin{matrix} -\sqrt{P}/N & \sqrt{P}/N & \sqrt{P}/N \end{matrix} & \text{for } N^2 P \gg 1. \end{cases} \tag{2.27}$$

As we will see, arguments based on shear, as well as our numerical results, find the same scaling for these strains.

Shear. We can also formulate an argument for the scaling of γ_{cc} under *shear* from dimensional analysis. Other than taking γ_{cc} constant, there is no clear

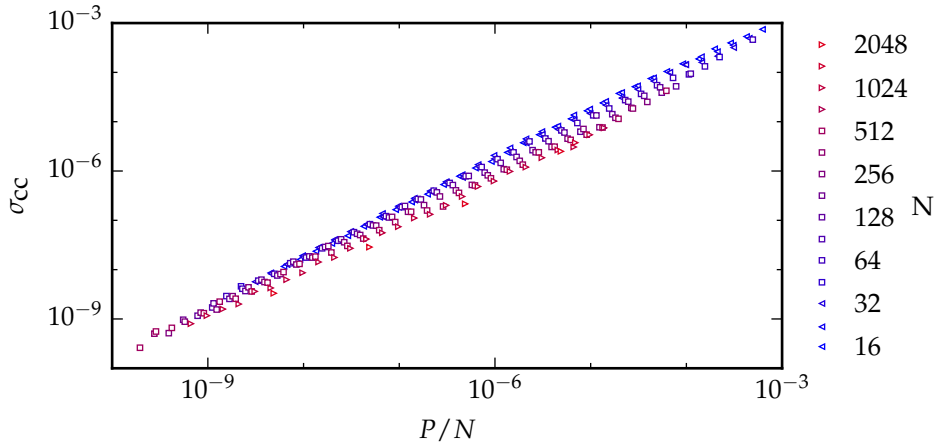

FIGURE 2.11: $\sigma_{cc} = \langle \sigma_* \rangle$ as a function of P/N. Colors and symbols indicate system size. The data supports an overall scaling $\sigma_{cc} \sim P/N$, but the lack of a good collapse suggests this does not describe the entire behavior.

strain scale, so we will construct the argument using stress instead. We will start by determining the mean contact change stress in an ensemble, $\sigma_{cc} = \langle \sigma_* \rangle$.

There are three stress scales in the system: the confining pressure P, the bulk modulus K and the shear modulus G. As we are describing shear, it seems unlikely that K is relevant. If the mean stress σ_{cc} would scale with G, we would end up with a constant strain, and we have already seen that γ_{cc} is not constant. This suggests that the only relevant stress scale is the confining pressure P, so we will take $\sigma_{cc} \sim P$.

The stress scale will also depend on the system size. Say we have a packing with N particles, which has a contact change at $\sigma = \sigma_{cc}$. If we duplicate this system, we will have $2N$ particles, and two contact changes will have happened at the same stress σ_{cc}, so we expect that $\sigma_{cc} \sim 1/N$.

Combining these two scalings suggests the following scaling:

$$\sigma_{cc} \sim P/N \,, \tag{2.28}$$

which is not strongly inconsistent with our data (Fig. 2.11). Next, we determine the strain scale γ_{cc} via the shear modulus $G = \sigma/\gamma$. From earlier

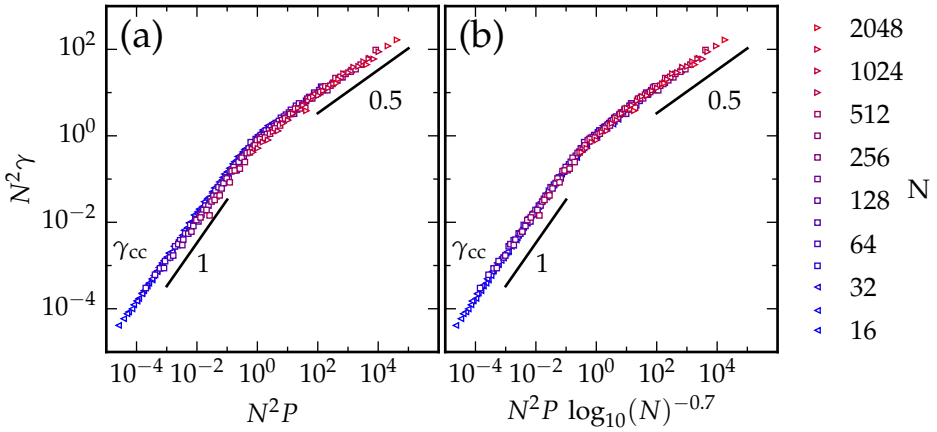

FIGURE 2.12: (a) Scaling of the strain at first contact change γ^{cc} as function of N and P. Symbols and colors indicate packing sizes. Lines indicate power law functions with exponent 1 (lower branch) and 0.5 (upper branch). (b) Log corrections improve the collapse.

work [22, 33, 34], we know G scales as

$$G \sim \begin{cases} \sqrt{P} & \text{for } N^2P \gg 1, \\ 1/N & \text{for } N^2P \ll 1, \end{cases} \tag{2.29}$$

which, combined with the stress scaling we derived, suggests the following scaling for γ_{cc}:

$$\gamma_{cc} \sim \sigma_{cc}/G \sim \begin{cases} (P/N)/\sqrt{P} & \sim \sqrt{P}/N & \text{for } N^2P \gg 1, \\ (P/N)/(1/N) & \sim P & \text{for } N^2P \ll 1. \end{cases} \tag{2.30}$$

This argument does not distinguish between making and breaking contacts. The choice of P as stress scale is consistent with the breaking of contacts, as the overlap $\delta \sim P$. When we compare the scaling to the compressional argument (Eq. (2.27)), we find it is indeed consistent with the breaking case, but not with the making case. Nonetheless, the argument is still consistent with the overall scaling, because the behavior is dominated by breaking contacts.

Numerical results. We can now compare our numerical results to the scaling relationship predicted by the arguments given above. We will initially not distinguish between the making and breaking of contacts because making events become exceedingly rare at low P, leading to poor statistics. In § 2.4.3, we will use linear response to take a more detailed look at the different types of events, including the difference between the making and breaking of contacts.

The suggested scaling in Eq. (2.30) implies that plotting $N^2\gamma_{cc}$ as a function of N^2P should collapse all numerical data:

$$N^2\gamma_{cc} \sim \begin{cases} N\sqrt{P} = (N^2P)^{0.5} & \text{for } N^2P \gg 1, \\ N^2P = (N^2P)^1 & \text{for } N^2P \ll 1. \end{cases} \tag{2.31}$$

We have plotted our numerical results in Fig. 2.12(a) and get a good (but not great) collapse. We retrieve the expected scaling behavior from Eq. (2.31), but we still find a minor dependence on system size. It has been suggested that the upper critical dimension for jamming is two, which implies logarithmic corrections in system size [28]. Using the form suggested in [28], we find a very good collapse (Fig. 2.12(b)). Consistently with what was recently found for the contact number and for the elastic moduli [28], also contact making and breaking under shear follows finite size scaling, with two distinct scaling regimes.

2.4 Linear response

We will now show that many properties of the first contact change can be deduced from the rest state at $\gamma = 0$ using linear response. Instead of using a direct numerical simulation (DNS), we estimate the trajectories of (non-rattler) particles from their linear elastic response: $\vec{x_i}(\gamma) = \vec{x_i}(0) + \vec{u_i}(0) \cdot \gamma$, where $\vec{u_i}(0) = [\partial\vec{x_i}/\partial\gamma](0)$ is calculated directly from the rest state. This strategy not only allows us to obtain the correct strains for the first contact change, but also gives us insight into the microscopic mechanisms. In particular, linear response allows us to probe the closing of contacts in detail, which is difficult in DNS simulations since, at low N^2P, it becomes exceedingly rare for the first contact change to be a contact making event (Figs. 2.5(b) and 2.17(b)).

Why are we allowed to assume that the response remains linear up to the first contact change? In essence, we will show that the nonlinear behavior of jammed packings emerges due to the cumulative effects of many contact changes. In contrast, between contact changes, the stress-strain response is essentially linear (§ 2.4.1). After calculating the linear response for our systems (§ 2.4.2), we will show that it predicts the contact change strains with surprising accuracy (§ 2.4.3): Linear response predicts its own demise! Finally, we investigate the breaking and closing of contacts independently (§ 2.4.4) and find that their characteristic strains scale differently. From these strains, we then accurately predict how often the first contact change is a contact making event in the DNS simulations.

2.4.1 Stress response

First, we will show that the stress-strain response of our systems is essentially linear in the DNS simulations. From the simulations, we find the shear stress $\sigma(\gamma)$ at various strains before the first contact change (Fig. 2.13(a)). We then fit this response with a second-order polynomial $\sigma = G^{\text{fit}}\gamma + \lambda\gamma^2$, and quantify the relative contribution of the quadratic component.

We quantify the contribution by calculating the ratio between the quadratic and linear contributions to σ at the contact change strain γ_*:

$$Q = \left| \frac{\lambda {\gamma^*}^2}{G^{\text{fit}}\gamma_*} \right| = \left| \frac{\lambda\gamma_*}{G^{\text{fit}}} \right| . \tag{2.32}$$

For the typical example in Fig. 2.13(a), we find $Q = 0.014$. We also show an extreme example with $Q = 0.267$ in Fig. 2.13(b). In Fig. 2.13(c), we have plotted the CDF of Q for four ensembles. We find the largest deviations from linear response for small systems at high pressure ($N = 16$, $P = 10^{-2}$), but even there the quadratic term is small compared to the linear term, with $\langle Q \rangle = 1.4 \cdot 10^{-2}$.

In Fig. 2.14(a), we plot Q as function of N and P. The most important observation is that Q remains small: in the vast majority of cases, $Q < 10^{-3}$, and the nonlinear case shown in Fig. 2.13(b) is truly exceptional. The two regions where Q appears to be the largest are for small N and large P, and for large N and small P. The origins for these deviations are different. For large systems at low pressure, the larger deviation is caused by inherent nonlinearities in the system, as indicated by the high median squared

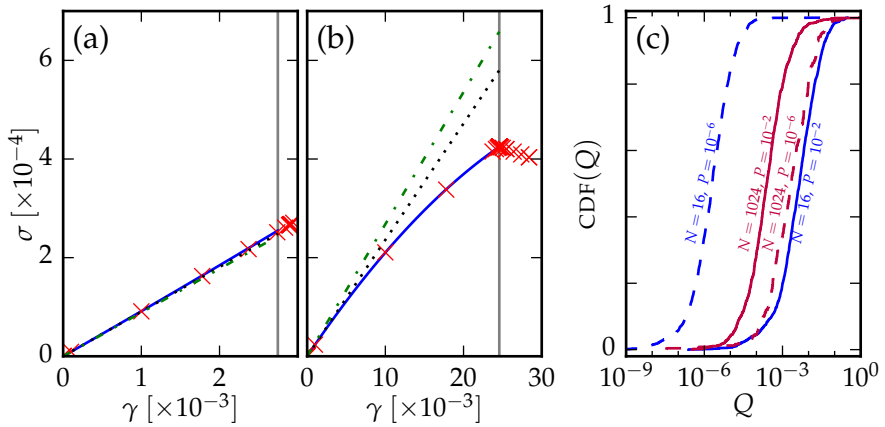

FIGURE 2.13: Stress response for (a) a packing with a typical deviation from linear $Q = 0.014$ and (b) a packing with a very large deviation $Q = 0.267$ (both $N = 16, P = 10^{-2}$). The simulation data (red $\times$) is fitted with the second-order polynomial (blue solid curves) $\sigma = G^{\text{fit}}\gamma + \lambda\gamma^2$, from which we determine $Q = |\lambda\gamma_*/G^{\text{fit}}|$. The black dotted curves are the linear contribution $\sigma = G^{\text{fit}}\gamma$; the green dash-dotted curves are the linear response predictions $\sigma = G^{\text{LR}}\gamma$. The gray vertical lines indicate the strain at the first contact change γ_*. (c) CDF of Q for various ensembles. There is no clear trend with either N or P. For the curve with largest mean ($N = 16, P = 10^{-2}$), we find that the mean $\langle Q\rangle = 1.4 \cdot 10^{-2}$ and standard deviation $s_Q = 2.8 \cdot 10^{-2}$ are both much smaller than 1 — hence linear response captures the majority of stress-strain curves very well.

quadratic component $[\lambda^2]_{0.5}$ of the stress-strain relation (Fig. 2.14(b)), where we use the median due to the large influence of outliers on the mean $\langle\lambda^2\rangle$. Small systems at high pressures exhibit a small quadratic component, but due to the larger strains involved, the deviation from linear response becomes significant in this regime. Nevertheless, the quadratic contribution to the stress is always small compared to the linear contribution, and we therefore expect to be able to predict the response of the system directly from linear response.

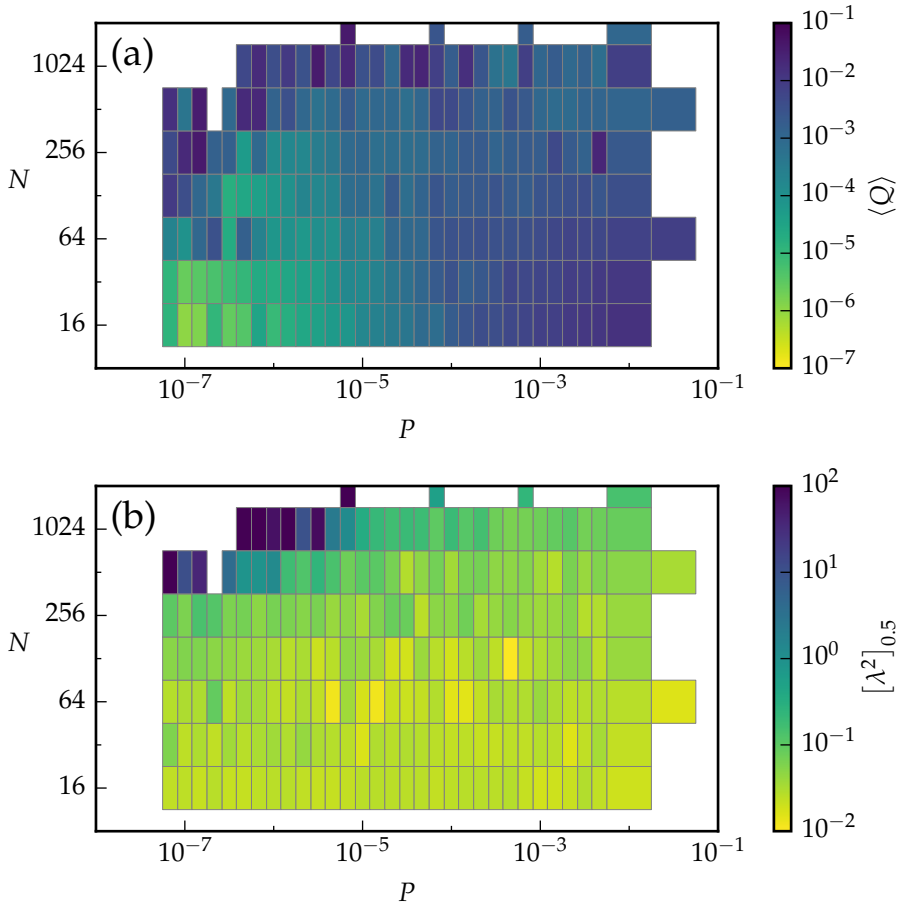

FIGURE 2.14: (a) Mean deviation from linear response at the first contact change for different ensembles. Strains are very well described by linear response for small systems at low pressures. Significant deviations only occur for small systems at high pressures and large systems at low pressures. (b) Median squared quadratic component $[\lambda^2]_{0.5}$. The component is of the order 10^{-2} in most cases, but grows to 10^2 for large systems at low pressure (close to jamming).

2.4.2 Calculating the linear response

In this section we will briefly review how, based on the initial particle positions, box size and box shape, we determine the linear response of the system. Given an applied deformation of the box, we can determine the resulting particle motion, forces and energy cost [21, 24, 28, 30, 34].

The state of the system can be described as a vector

$$|q\rangle = |q_x, q_b\rangle = |\{x_1 \dots x_N, y_1 \dots y_N\}, \{L_{xx}, L_{xy}, L_{yx}, L_{yy}\}\rangle \tag{2.33}$$

where (x_i, y_i) is the position of particle i and the four parameters L_{ab} describe the box size and shape. We only include particles that are part of the load bearing network (non-rattlers).

We then prescribe a displacement $|\Delta q\rangle$. We determine the energy in the new state $|q + \Delta q\rangle$ by expanding U up to second order:

$$U(|q + \Delta q\rangle) = U(|q\rangle) + \langle J_q|\Delta q\rangle + \frac{1}{2}\langle \Delta q|\boldsymbol{H_q}|\Delta q\rangle + O(\Delta q^3) \tag{2.34}$$

where

$$\langle J_q| = \langle \frac{\partial U}{\partial x_1}, \cdots, \frac{\partial U}{\partial L_{yy}}| \tag{2.35}$$

is the Jacobian and

$$\boldsymbol{H_q} = \begin{pmatrix} \frac{\partial^2 U}{\partial x_1 \partial x_1} & \cdots & \frac{\partial^2 U}{\partial x_1 \partial L_{yy}} \\ \vdots & \ddots & \end{pmatrix} \tag{2.36}$$

the extended Hessian at state $\langle q|$ [24, 34, 90]. Because the initial state is at an energy minimum, the Jacobian term is zero, and the leading contribution to the energy is quadratic and comes from the extended Hessian.

For a given displacement, the energy cost is thus given by

$$\Delta U = \frac{1}{2}\langle \Delta q|\boldsymbol{H_q}|\Delta q\rangle \ , \tag{2.37}$$

and the resulting forces on particles and boundaries are

$$|f\rangle = \boldsymbol{H_q}\,|\Delta q\rangle \ . \tag{2.38}$$

Typically, however, we do not know the displacement of each particle. Instead, we wish to calculate the displacement of the particles given a

change in the boundaries, i.e., find a state where, given the new boundaries, the sum of forces on each particle is zero. To find this state, we split the extended Hessian into four parts:

$$\boldsymbol{H} = \begin{pmatrix} \boldsymbol{H_{xx}} & \boldsymbol{H_{bx}^T} \\ \boldsymbol{H_{bx}} & \boldsymbol{H_{bb}} \end{pmatrix} , \tag{2.39}$$

where the ordinary Hessian $\boldsymbol{H_{xx}}$ describes the particle-particle interactions, $\boldsymbol{H_{bx}}$ the interactions between boundaries and particles, and $\boldsymbol{H_{bb}}$ those between different boundaries. We can then rewrite Eq. (2.38) as follows:

$$\begin{pmatrix} |\Delta f_x\rangle \\ |\Delta f_b\rangle \end{pmatrix} = \begin{pmatrix} \boldsymbol{H_{xx}} & \boldsymbol{H_{bx}^T} \\ \boldsymbol{H_{bx}} & \boldsymbol{H_{bb}} \end{pmatrix} \begin{pmatrix} |\Delta q_x\rangle \\ |\Delta q_b\rangle \end{pmatrix} . \tag{2.40}$$

where $|\Delta q_x\rangle$ and $|\Delta q_b\rangle$ are the displacements of particles and boundaries, and $|\Delta f_x\rangle$ and $|\Delta f_b\rangle$ the corresponding forces. Setting the forces on the particles to zero, we find

$$|\Delta f_x\rangle = \boldsymbol{H_{xx}} |\Delta q_x\rangle + \boldsymbol{H_{bx}^T} |\Delta q_b\rangle = 0. \tag{2.41}$$

Solving for $|\Delta q_x\rangle$ gives us particle displacements as a function of the deformation of the simulation box

$$|\Delta q_x\rangle = -\boldsymbol{H_{xx}^{-1}} \boldsymbol{H_{bx}^T} |\Delta q_b\rangle . \tag{2.42}$$

Unfortunately, $\boldsymbol{H_{xx}^{-1}}$ cannot be calculated due to the two zero-energy translational modes. Instead, we choose to use the Moore-Penrose pseudoinverse $\boldsymbol{H_{xx}^{+}}$, which fixes the zero-energy translational modes in place [91, §6.4]:

$$|\Delta q_x\rangle = -\boldsymbol{H_{xx}^{+}} \boldsymbol{H_{bx}^T} |\Delta q_b\rangle \ . \tag{2.43}$$

The full displacement vector is then given by

$$|\Delta q\rangle = \begin{pmatrix} -\boldsymbol{H_{xx}^{+}} \boldsymbol{H_{bx}^T} |\Delta q_b\rangle \\ |\Delta q_b\rangle \end{pmatrix} . \tag{2.44}$$

To calculate the energy cost and the stress on the boundary, we use Eq. (2.40), and find

$$|\Delta f_b\rangle = \boldsymbol{H_{bx}} |\Delta q_x\rangle + \boldsymbol{H_{bb}} |\Delta q_b\rangle = (\boldsymbol{H_{bb}} - \boldsymbol{H_{bx}} \boldsymbol{H_{xx}^{+}} \boldsymbol{H_{bx}^T}) |\Delta q_b\rangle \ . \tag{2.45}$$

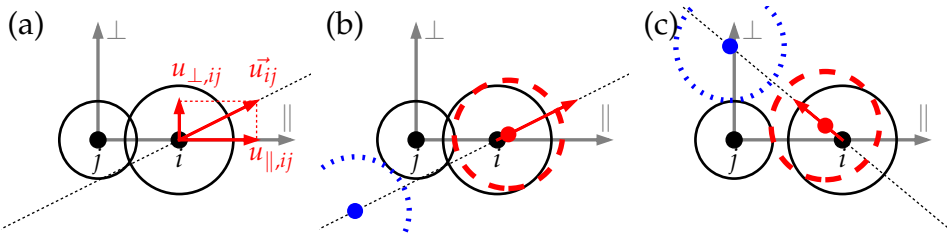

FIGURE 2.15: (a) Inter-particle motion between particle i and j, where particle j is fixed in the origin. (b) For most trajectories, there are two solutions (red dashed and blue dotted circles) where the particle overlap $\delta = 0$, but only the solution with positive strain (red dashed) is physically relevant solution. (c) In the case of a closing contact, there are two positive solutions, where the minimum strain is the physically relevant solution.

The corresponding stress can be calculated as

$$|\Delta\sigma_b\rangle = |\frac{\Delta f_{xx}}{L_{xx}}, \frac{\Delta f_{xy}}{L_{xx}}, \frac{\Delta f_{yx}}{L_{yy}}, \frac{\Delta f_{yy}}{L_{yy}}\rangle \ , \tag{2.46}$$

but in practice, it is more convenient to calculate the stress by using the Born-Huang approximation (Eq. (2.13)) on the new particle positions $|q_x'\rangle = |q_x\rangle + |\Delta q_x\rangle$. The stress also allows us to determine the elastic modulus corresponding to a given boundary deformation

$$c_q = \langle \Delta\sigma_b | \Delta q_b \rangle \ / \ \langle \Delta q_b | \Delta q_b \rangle \ . \tag{2.47}$$

For the resulting energy change we use $|\Delta f_x\rangle \equiv 0$ to find

$$\Delta U = \frac{1}{2} \langle \Delta q_b | \Delta f_b \rangle = \frac{1}{2} \langle \Delta q_b | \left(\boldsymbol{H_{bb}} - \boldsymbol{H_{bx}} \boldsymbol{H_{xx}^{+}} \boldsymbol{H_{bx}^{T}} \right) | \Delta q_b \rangle \ . \tag{2.48}$$

We now have all ingredients in place to calculate, for a given boundary deformation, the particle displacements, stress response and energy change from linear response. In the next section, we will use this to calculate the strain at the first contact change.

2.4.3 Contact change strains

In this section, we will describe how we calculate the contact change strains from linear response, and we will compare their values to the results from

direct numerical simulations. First, for each particle pair i, j, we determine the contact change strain γ_{ij}, defined as the strain where the particles, assuming linear trajectories, break contact or make a new contact. By minimizing over all strains, we then calculate *(i)* the strain at which the first new contact is made $\gamma^{\mathrm{LR}}_{*,\mathrm{mk}}$, *(ii)* the strain at which the first contact breaks $\gamma^{\mathrm{LR}}_{*,\mathrm{bk}}$, and *(iii)* the strain at the first contact change γ^{LR}_{*}, which is the minimum of $\gamma^{\mathrm{LR}}_{*,\mathrm{mk}}$ and $\gamma^{\mathrm{LR}}_{*,\mathrm{bk}}$. We can then, for each packing, compare these values of the strain to their counterparts obtained by simulation.

Calculating γ^{LR}_{*}. For each particle pair i, j, we determine the velocity

$$\vec{u_i} = \partial \vec{x_i} / \partial \gamma \, . \tag{2.49}$$

by evaluating Eq. (2.43) with the unit simple shear deformation $|\Delta q_b\rangle = L\hat{L}_{xy}$. The inter-particle velocities are then given by

$$\vec{u_{ij}} = \vec{u_i} - \vec{u_j} - n_{y,ij} L \hat{x} \, , \tag{2.50}$$

where the last term incorporates the velocity between the copies of the periodic box. Combining these, we can solve

$$|\vec{r_{ij}} + \gamma_{ij} \vec{u_{ij}}| = R_i + R_j \tag{2.51}$$

for γ_{ij} to determine when the overlap $\delta_{ij} = 0$. There are, in general, two solutions for γ_{ij}, but only one of them is physically relevant, as indicated in Fig. 2.15(b) and (c): the physically relevant value is the minimal positive strain.

The first contact change for the entire system is then determined by taking the minimum of the strain over all particle pairs i, j:

$$\gamma^{\mathrm{LR}}_{*} \equiv \min(\gamma_{ij}) \, . \tag{2.52}$$

We can also limit ourselves to breaking and making strains to determine the first broken and the first new contact independently:

$$\gamma^{\mathrm{LR}}_{*,\mathrm{bk}} \equiv \min_{i,j \text{ in contact}} \gamma_{ij} \, , \tag{2.53}$$

$$\gamma^{\mathrm{LR}}_{*,\mathrm{mk}} \equiv \min_{i,j \text{ not in contact}} \gamma_{ij} \, . \tag{2.54}$$

This allows us to study closing events directly, which is difficult in DNS simulations due to their rarity at low pressures.

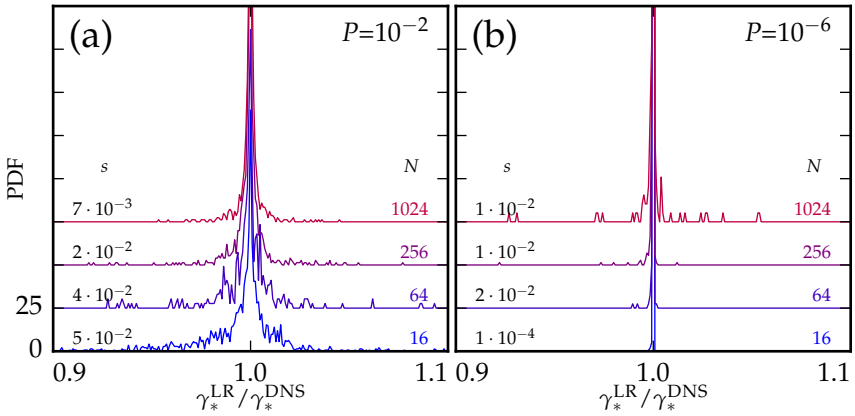

FIGURE 2.16: PDFs of $\gamma_*^{\mathrm{LR}}/\gamma_*^{\mathrm{DNS}}$ for various system sizes at (a) $P = 10^{-2}$ and (b) $P = 10^{-6}$. For each PDF, the standard deviation s is indicated. We observe that γ_*^{LR} is a good predictor for γ_*^{DNS}, with standard deviations on the order of 5% for small systems and 1% for large systems.

Comparison with numerical simulations. We now show that linear response accurately predicts the contact change strain. For each individual system, we compare the linear response value γ_*^{LR} to the corresponding strain γ_*^{DNS} from the DNS simulation. In Fig. 2.16, we plot PDFs of $\gamma_*^{\mathrm{LR}}/\gamma_*^{\mathrm{DNS}}$ to quantify the relative deviation from the simulation. We observe that γ_*^{LR} is a good predictor for γ_*^{DNS}. First, these distributions are peaked around 1, which shows the mean strain found in linear response matches that of the simulations very well. Second, the standard deviation of the distributions, s, is of the order of 5% for small systems and 1% for large systems. At $P = 10^{-2}$, the largest packings have a standard deviation of 7×10^{-3}, which increases to 5×10^{-2} for small systems. The largest standard deviation is obtained for very small systems ($N = 16$) at high P (10^{-2}). We find a strong dependency on pressure: for $P = 10^{-6}$, the distributions become very narrow around 1. The standard deviations remains on the order of 10^{-2} due to outliers. We conclude that for all parameters considered, the differences between the strains obtained by linear response and direct numerical simulation are small. In addition to determining the right contact change *strain*, we found that in over 90% of

cases linear response also correctly identifies the contact i, j where the first contact change takes place.

In conclusion, linear response provides us with a powerful tool to predict the behavior of packings. It allows us to predict the first contact change correctly, as well as determining microscopic properties unavailable in the DNS simulations. We note in passing that the correct prediction of contact changes suggests that shearing jammed packings might also be implemented in terms of a *discrete event simulation*, where, instead of slowly stepping through strain space, we immediately jump from contact change to contact change.

Rattlers. In § 2.2, we discussed the effect of rattlers in the DNS simulations. We will now focus on their effect in linear response. The creation of a rattler, i.e., a particle losing all its contacts, is also well-defined in linear response. In Fig. 2.4, we show a packing at the verge of creating a rattler (a), and show the overlap δ_{ri} of particle r with its neighbors A, B and C as a function of strain γ (b). In the simulations (symbols), we find the overlaps smoothly go to zero while approaching the contact change strain γ_*. In linear response, we find a slightly different contact change strain for each contact, but they are within $|\Delta\gamma/\gamma_*| < 10^{-4}$. As in § 2.2, we do not include systems where a rattler becomes part of the contact network in our analysis.

2.4.4 Scaling of ensemble averages obtained in linear response

Now that we have established that we can predict contact changes using linear response, we will study the making and closing strains in detail. Based on Eq. (2.27), we expect three scaling regimes for the contact change strains: for low N^2P, $\gamma_{\mathrm{mk}} \sim 1/N^2$ and $\gamma_{\mathrm{bk}} \sim P$, while for high N^2P, both γ_{bk} and γ_{mk} are expected to scale as $\sqrt{P/N^2}$. As before, these scalings suggest scaling collapse if we plot $N^2\gamma$ as a function of N^2P:

$$N^2\gamma \sim \begin{cases} N\sqrt{P} &= (N^2P)^{0.5} \quad \text{for } N^2P \gg 1, \\ N^2P &= (N^2P)^{1} \quad \text{for bk, } N^2P \ll 1, \\ 1 &= (N^2P)^{0} \quad \text{for mk, } N^2P \ll 1. \end{cases} \tag{2.55}$$

In Fig. 2.17(a), we plot our linear response data using this rescaling. As in § 2.3.3, applying log corrections [28] improves the collapse (Fig. 2.17(b)).

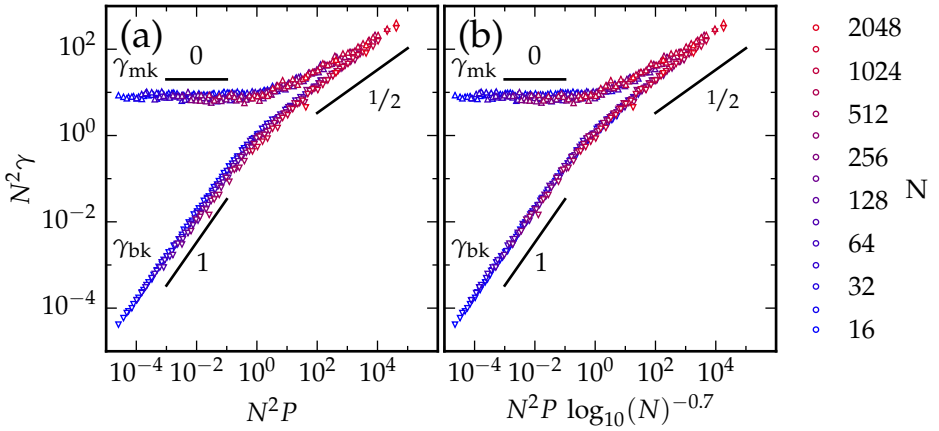

FIGURE 2.17: (a) Scaling of ensemble averaged breaking ($\triangledown$) and making ($\triangle$) strains $\gamma_{bk}^{LR} = \langle \gamma_{*,bk}^{LR} \rangle$ and $\gamma_{mk}^{LR} = \langle \gamma_{*,mk}^{LR} \rangle$ from linear response. (b) As in Fig. 2.12, log corrections significantly improve the quality of the collapse.

For low N^2P, we find that the data is well described by the expected power laws, but for high N^2P, we find that neither branch cleanly scales as $\gamma \sim \sqrt{P}/N$, even though the branches *combined* do appear to scale that way. The branches slowly converge, and join around $N^2P \sim 10^{-4}$. We expect that for larger systems, for which N^2P can be large while P remains small, the clean square root scaling will be recovered for both branches.

What do these different scalings imply for properties that we can measure in the DNS simulation, specifically for the contact change strain γ_{cc} and the prevalence of making versus breaking events? Starting with the exponential CDFs (Eq. (2.23)) for making and breaking,

$$\Pr(\gamma_{*,mk} \leq \gamma) = 1 - e^{-\gamma/\beta_{mk}} \qquad \gamma \geq 0, \tag{2.56}$$

$$\Pr(\gamma_{*,bk} \leq \gamma) = 1 - e^{-\gamma/\beta_{bk}} \qquad \gamma \geq 0, \tag{2.57}$$

where β is the mean value of the distribution, we can derive the CDF for the minimum of the distributions, assuming $\gamma \geq 0$:

$$\begin{aligned} \Pr(\min\{\gamma_{*,mk}, \gamma_{*,bk}\} \leq \gamma) &= \Pr(\left[\gamma_{*,mk} \leq \gamma\right] \vee \left[\gamma_{*,bk} \leq \gamma\right]) \\ &= 1 - e^{-\gamma/\beta_{mk}} e^{-\gamma/\beta_{bk}} \\ &= 1 - e^{-\gamma/\beta_{cc}}\,, \end{aligned} \tag{2.58}$$

so the mean *contact change* strain becomes

$$\beta_{\mathrm{cc}} = \frac{1}{1/\beta_{\mathrm{bk}} + 1/\beta_{\mathrm{mk}}} \,. \tag{2.59}$$

We can also derive the probabilities of the first change being a breaking or making event. We will derive $\Pr(\mathrm{mk}) = 1 - \Pr(\mathrm{bk})$ rather than $\Pr(\mathrm{bk})$, as the former vanishes for $N^2 P \to 0$.

$$\begin{aligned}
\Pr(\mathrm{mk})^{\mathrm{LR}} &= \int_0^\infty \Pr(\left[\gamma_{*,\mathrm{mk}} = \gamma\right] \wedge \left[\gamma_{*,\mathrm{bk}} > \gamma\right]) \, d\gamma \\
&= \int_0^\infty \left[(1/\beta_{\mathrm{mk}}) e^{-\gamma/\beta_{\mathrm{mk}}}\right] \cdot \left[e^{-\gamma/\beta_{\mathrm{bk}}}\right]) \, d\gamma \\
&= -\frac{1/\beta_{\mathrm{mk}}}{1/\beta_{\mathrm{mk}} + 1/\beta_{\mathrm{bk}}} e^{-\gamma \cdot (1/\beta_{\mathrm{mk}} + 1/\beta_{\mathrm{bk}})} \Big|_0^\infty \\
&= \frac{1}{1 + \beta_{\mathrm{mk}}/\beta_{\mathrm{bk}}} \,.
\end{aligned} \tag{2.60}$$

For $N^2 P \gg 1$, we found that in linear response $\beta_{\mathrm{mk}} \sim \beta_{\mathrm{bk}} \sim \sqrt{P/N^2}$. This means that breaking and making a contact are equally likely, and the mean strain β_{cc} is half that of the individual strains. For $N^2 P \ll 1$, the behavior is different. In this regime, $\beta_{\mathrm{bk}} \ll \beta_{\mathrm{mk}}$, so the combined average strain β_{cc} is dominated by β_{bk}:

$$\beta_{\mathrm{cc}} = \frac{1}{1/\beta_{\mathrm{bk}} + 1/\beta_{\mathrm{mk}}} \approx \beta_{\mathrm{bk}} \,, \tag{2.61}$$

i.e., the mean contact change strain is given by the mean breaking strain. The probability of making a contact in this regime is much smaller than breaking one:

$$\Pr(\mathrm{mk})^{\mathrm{LR}} = \frac{1}{1 + \beta_{\mathrm{mk}}/\beta_{\mathrm{bk}}} \sim \frac{1}{1 + 1/N^2 P} \approx N^2 P \ll 1 \,. \tag{2.62}$$

In Fig. 2.18(a), we show $\Pr(\mathrm{mk})^{\mathrm{LR}}$ as a function of $N^2 P$ for each ensemble, and find the derived scaling: $\Pr(\mathrm{mk}) \sim N^2 P$ for small $N^2 P$ and $\Pr(\mathrm{mk}) \sim 1/2$ for high $N^2 P$. We then fit our data with a simple scaling function to ease comparison with the numerical data.

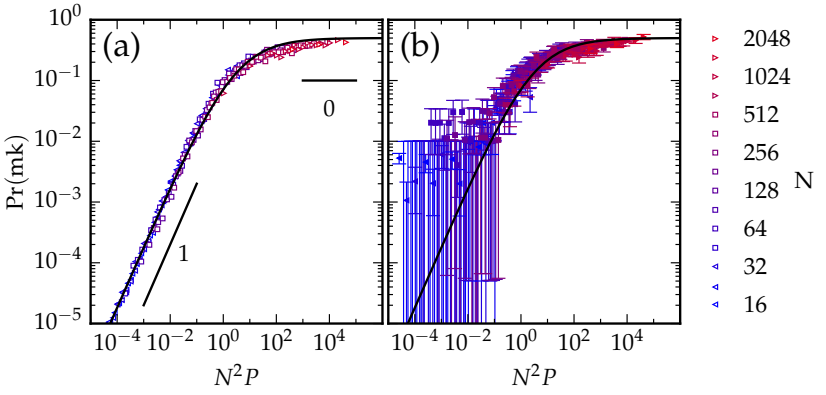

FIGURE 2.18: (a) Scaling of $\mathrm{Pr(mk)}^{\mathrm{LR}} = \beta_{\mathrm{mk}}/(\beta_{\mathrm{mk}} + \beta_{\mathrm{bk}})$ using the average making and breaking strain from linear response. The curve is a fit to $\mathrm{Pr(mk)} = \frac{b}{2}N^2P/(1 + \sqrt{b \cdot N^2P})^2$ with $b = 0.35 \pm 0.01$. (b) Scaling of the frequentist probability $\mathrm{Pr(mk)}^{\mathrm{DNS}} = N^{\mathrm{mk}}/N$ from DNS simulation data. Because of the limited ensemble size ($100 - 2000$), the error bars are large, especially for low Pr. The curve is the same as in (a). Error bars without symbols indicate ensembles without making events.

To compare the results to numerical simulations, we determine the frequentist probability

$$\mathrm{Pr(mk)}^{\mathrm{DNS}} = N_{\mathrm{mk}}/N_{\mathrm{total}}\,. \tag{2.63}$$

We then plot this probability against N^2P in Fig. 2.18(b). To get an error estimate, we model the system as Poissonian [92, A1], and use

$$s = \sqrt{N(\mathrm{Pr})(1-\mathrm{Pr})}/N\,, \tag{2.64}$$

as standard deviation, where we take $\mathrm{Pr} = \mathrm{Pr(mk)}^{\mathrm{DNS}}$. If $\mathrm{Pr(mk)}^{\mathrm{DNS}} = 0$, we take $\mathrm{Pr} = 1/N_{\mathrm{total}}$.

We find the scaling describes our data reasonably well for medium to high N^2P, but at lower N^2P, we find a large number of outliers on a plateau around $\mathrm{Pr(mk)}^{\mathrm{DNS}} \approx 5 \cdot 10^{-3}$. We propose this deviation is caused by difference in the distributions of γ_{mk} and γ_{bk}. In Fig. 2.19, we plot the distributions of γ_{mk} and γ_{bk}. As we have seen in § 2.3.2, the distribution of γ_{cc} deviates from exponential for $N^2P \ll 1$, but here we

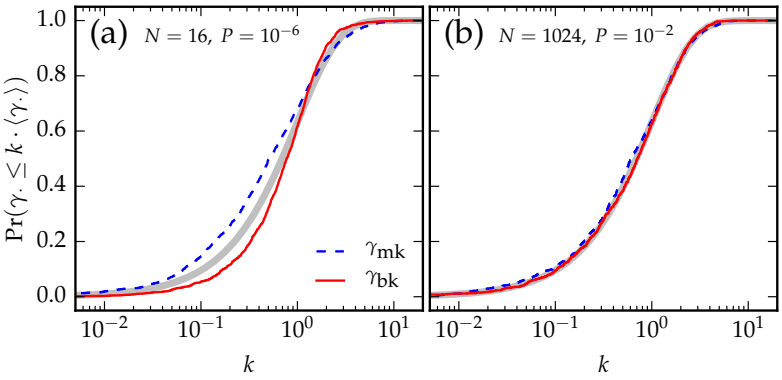

FIGURE 2.19: Rescaled CDFs for the first breaking event strain $\Pr(\gamma_{bk} \leq k \cdot \langle\gamma_{bk}\rangle)$ (red line) and the first making event strain $\Pr(\gamma_{mk} \leq k \cdot \langle\gamma_{mk}\rangle)$ (blue dashes) for (a) $N = 16$, $P = 10^{-6}$ and (b) $N = 1024$, $P = 10^{-2}$. For high N^2P, both CDFs are well-described with an exponential (light gray background curve), but for low N^2P, both CDFs diverge from an exponential. The distribution of γ_{mk} gets more weight at low values, while the distribution of γ_{bk} gets more weight at higher values.

find that the distributions for γ_{mk} and γ_{bk} deviate from exponential in a different way. For γ_{mk}, there is a bias towards lower strains, explaining the relative abundance of making events.

We have seen that linear response provides us with a powerful tool to understand what happens in the DNS simulations. We not only predict the first contact change with surprising accuracy, we can also predict the prevalence of different types of events.

2.5 Multiple contact changes

In this section, we will discuss the behavior of our systems when strained beyond the first contact change. We will discuss the implications of contact changes for continuum elasticity, and will take a look at the effects of switching from free boundaries at zero strain to fixed boundaries in systems at finite strain.

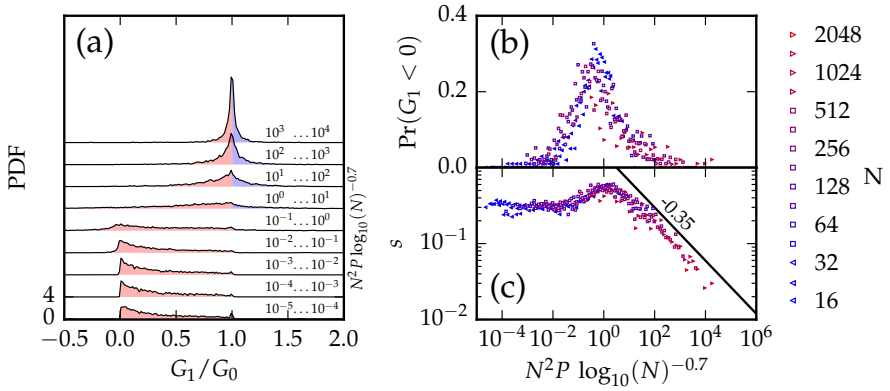

FIGURE 2.20: (a) Probability distribution functions of G_1/G_0, the relative shear modulus after the first contact change, for different values of $N^2 P \log_{10}(N)^{-0.7}$. For small systems at low pressures (bottom), we find $0 \leq G_1/G_0 \leq 1$. For intermediate systems, we find G_1/G_0 is typically smaller than 1, but can become negative (indicating an unstable system). For large systems at high pressures (top), we find $G_1/G_0 \approx 1$. The creation of contacts (blue) correlates with an increase in G, while the breaking of contacts (red) correlates with a decrease in G. (b) The fraction of events where $G_1 < 0$ peaks around $N^2 P \log_{10}(N)^{-0.7} \approx 1$. (c) The standard deviation of G_1/G_0. For small systems at low pressures, $s \approx 0.3$, whereas for large systems $s \sim (N^2 P)^{-\beta}$ with $\beta = 0.35 \pm 0.01$.

2.5.1 Shear modulus

As we have seen, the first contact change happens at lower and lower strains as systems get larger. Schreck et al. [76] suggested that this implies that linear response is no longer valid for disordered systems at large N. It is clear that changing a single contact can have a large effect on small systems, but one would expect the effect to vanish in larger systems: in the thermodynamic limit, systems are expected to behave increasingly like an elastic solid, and this apparent paradox lead to a lively debate [77, 78, 93].

Here we show how the effect of a single contact change on the shear modulus becomes smaller and smaller when the system size is increased. We note that, as long as the shear modulus does not change significantly, we can consider the system to have an *effective* linear response, even though it is no longer *strictly* linear. To quantify the effect of a single contact change, we calculated the shear modulus before (G_0) and after (G_1) the first contact

change using Eq. (2.47). For each value of N and P, we have calculated the probability distributions $\rho(G_1/G_0)$. From these, we determine in particular $\Pr(G_1 < 0)$ (Fig. 2.20(a)) and the width of these distributions (Fig. 2.20(c)). We find that the shape of these distributions varies strongly and that we can organize our data using the finite size parameter $N^2P\ \log_{10}(N)^{-0.7}$, and as function of this parameter we distinguish three regimes.

(i) $N^2P\ \log_{10}(N)^{-0.7} \ll 1$. In the small system size limit, we find that $\rho(G_1/G_0)$ is a strongly asymmetric distribution, with most weight around zero. We find that the mean $\langle G_1/G_0\rangle \approx 0.2$, and that $0 < G_1 < G_0$. To understand this, we note that in this regime, the first contact change is a breaking event, which weakens the system. We find that G_1 is significantly smaller than G_0 because, in this regime, there is typically only a single excess contact (Fig. 2.10). Surprisingly, the system does not unjam immediately, for reasons we will discuss in § 2.5.2.

(ii) $N^2P\ \log_{10}(N)^{-0.7} \approx 1$. In the intermediate regime, the number of excess contacts remains small, contact changes are predominantly contact breaking events, and we observe that $G_1 < G_0$. However, the probability that $G_1 < 0$ becomes finite, in contrast to the behavior in regime *(i)*. This follows from the variation of forces on the contacts between particles, the *prestress*: without prestress, G has to be non-negative [28, 94], but as P increases in regime *(ii)* there is sufficient prestress to allow for negative values of G_1, and this happens in up to 35% of cases (Fig. 2.20(b)).

(iii) $N^2P\ \log_{10}(N)^{-0.7} \gg 1$. For large systems, we enter the continuum regime, where the distribution $\rho(G_1/G_0)$ peaks around one and becomes increasingly symmetric and narrow. Hence $G_1 \approx G_0$, and this is the essence of the solution of the apparent paradox. The symmetry of the distribution is consistent with out observation that contact creation and contact breaking becomes equally likely in this regime.

Types of events. We observe a strong correlation between the *type* of events and the behavior of G_1/G_0, where, in the vast majority of cases, $G_1 < G_0$ is linked to broken contacts, and $G_1 > G_0$ to created contacts (Fig. 2.20(a)). In a minority of breaking events ($\approx 0.5\%$), we find $G_1 < G_0$, but a close inspection of anomalous events systematically reveals that for these events,

rearrangements happen at very nearby strains, or $G_1 \approx G_0$, which suggest that their small probability is a measure of numerical noise, and does not contain significant physics.

Effective linear response. A simple scaling argument for the width of the distribution of G_1/G_0 can be obtained from combining the scaling of G with P, $G \sim \Delta z \sim \sqrt{P}$ with the observation that making and breaking of contacts is equally likely. As a single contact change modifies Δz by $\pm 1/N$, we thus expect $G_1^{\pm} \sim \Delta z_0 \pm 1/N$. The width of this distribution scales as

$$s \sim \frac{G_1^+ - G_1^-}{G_0} \sim \frac{1/N}{\Delta z_0} \sim \frac{1/N}{\sqrt{P}} = \frac{1}{\sqrt{N^2 P}}. \tag{2.65}$$

However, when we measure the width of the distribution using the standard deviation s, we observe it vanishes as $(N^2 P \log_{10}(N)^{-0.7})^{-\beta}$ with $\beta = 0.35 \pm 0.01$ (Fig. 2.20(c)). We suggest that the contacts changed under a shear deformation have a relatively large impact on the shear modulus - a relatively small number of contacts contribute disproportionately to the elastic moduli [95].

Nevertheless, the observed diminishing of the width of the distribution $\rho(G_1/G_0)$ is sufficiently strong to be consistent with an effective linear response picture. We call a material *effectively linear* if, for a small fixed deformation γ_t, the standard deviation of $G(\gamma_t)$ vanishes for $N \to \infty$. In terms of contact changes, we need to establish how the number of contact changes experienced up to γ_t grows with N, and how the effect of a single contact change decreases with N. We estimate the number of contact changes between $\gamma = 0$ and the test strain γ_t as

$$n = \gamma_t / \gamma_{cc} = \gamma_t / (\sqrt{P}/N) \,. \tag{2.66}$$

We then assume that all contact changes are independent of each other, and assume each contact change causes a change in G drawn from the distribution $\rho(G_1/G_0)$ with standard deviation $s \sim (N^2 P)^{-\beta}$. The central limit theorem then states that the standard deviation after n contact changes is given by

$$s_n \sim \sqrt{n} (N^2 P)^{-\beta} \,. \tag{2.67}$$

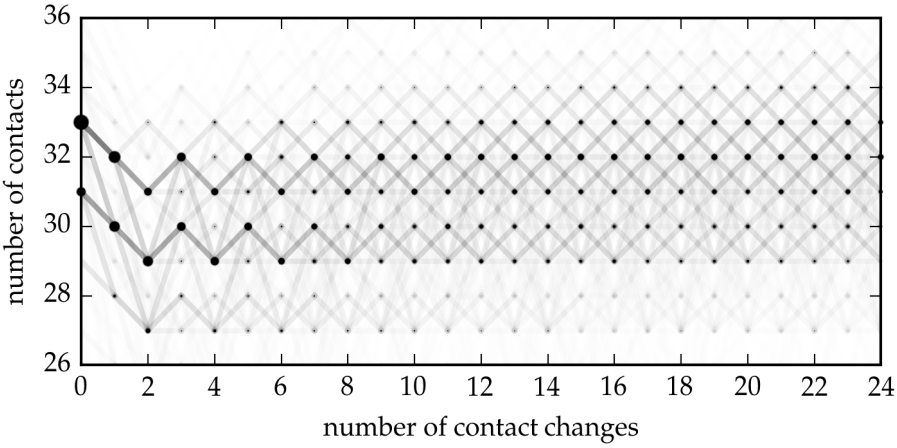

FIGURE 2.21: The number of contacts for systems with $N = 16$ particles at $P = 10^{-6}$. The circle area represents the fraction of systems with a given number of contacts; the thickness of the lines represent transition probabilities. Initially, the systems start off with the minimum number of contacts $2N + 1 = 33$ (31 or 29 when there are one or two rattlers, respectively). In the first and second contact change, the system loses one contact (three when a rattler is created). In the following events, the system alternately gains and loses a contact.

Combining these, we find that the standard deviation after a strain γ_t is given by

$$s_{\gamma_t} \sim \sqrt{\gamma_t/(\sqrt{P}/N)}\left(N^2P\right)^{-\beta} \sim \sqrt{\gamma_t} \cdot N^{\frac{1}{2}-2\beta}P^{-\frac{1}{4}-\beta}\,, \tag{2.68}$$

which vanishes for large N as long as $\frac{1}{2} - 2\beta < 0$, or

$$\beta > 1/4. \tag{2.69}$$

Clearly, $0.35 > 1/4$, so, for $N \to \infty$, our systems approach the continuum limit. This is consistent with the picture where, for large N, the effective value of G depends on the applied shear γ rather than the number of contact changes n [96, 97].

2.5.2 Alternating contact changes

Here, we investigate correlations between consecutive contact changes. In Fig. 2.21, we show the number of contacts in the system as a function

of the number of contact changes for systems with $N = 16$ particles, at $P = 10^{-6}$. Initially, systems have $2N + 1$ contacts, i.e., 33 if all particles are part of the contact network, 31 if there is one rattler and 29 if there are two rattlers. Surprisingly, we observe the first two contact changes are breaking events, bringing the contact number to $2N - 1$. The system then alternately gains and loses a contact, switching between $2N - 1$ and $2N$ contacts. This behavior stays apparent at least until the 10^{th} contact change. This evidences correlations between subsequent events. In addition, we note that the same contact is often involved in multiple contact changes, although typically not in *subsequent* contact changes.

The subtle role of boundary conditions. One question this poses is why the system is allowed to lose contacts in the first place: after all, we are on the brink of losing rigidity, and a single broken contact should unjam the system. However, that does not take into account the change in boundary conditions between the initial relaxation and the strained state. In the initial relaxation, we require

$$F_x = F_y = 0 \tag{2.70}$$

for all particles, and

$$\begin{aligned} \sigma_{yx} = \sigma_{xy} &= 0 \,, \\ \tau = \tfrac{1}{2}(\sigma_{xx} - \sigma_{yy}) &= 0 \,, \\ P_{\text{int}} = \tfrac{1}{2}(\sigma_{xx} + \sigma_{yy}) &= P_{\text{ext}} \,, \end{aligned} \tag{2.71}$$

for the boundaries. This gives us $2N + 3$ degrees of freedom. Two of these degrees are constrained by requiring zero global translation, and the other $2N + 1$ need to be constrained by at least $N_c = 2N + 1$ contacts between particles to be jammed [28, 33]. When we strain the system, this changes. Instead of requiring a fixed *stress* on the boundaries, we require a fixed *deformation*

$$L_{yx}(\gamma) = L_{yx}(0) + \gamma \cdot L(0) \,, \tag{2.72}$$

$$L_{xx}(\gamma) = L_{xx}(0) \,, \text{ and} \tag{2.73}$$

$$L_{yy}(\gamma) = L_{yy}(0) \,. \tag{2.74}$$

Of the initial $2N + 3$ degrees of freedom, we now only have $2N$ left, which means we need just $2N - 2$ contacts for stability: our system is suddenly

overconstrained, and we expect we need to break *four* contacts to unjam. Surprisingly, we find that the system only loses *two* contacts before gaining a new contact, and that diving below $2N - 1$ contacts already unjams the system.

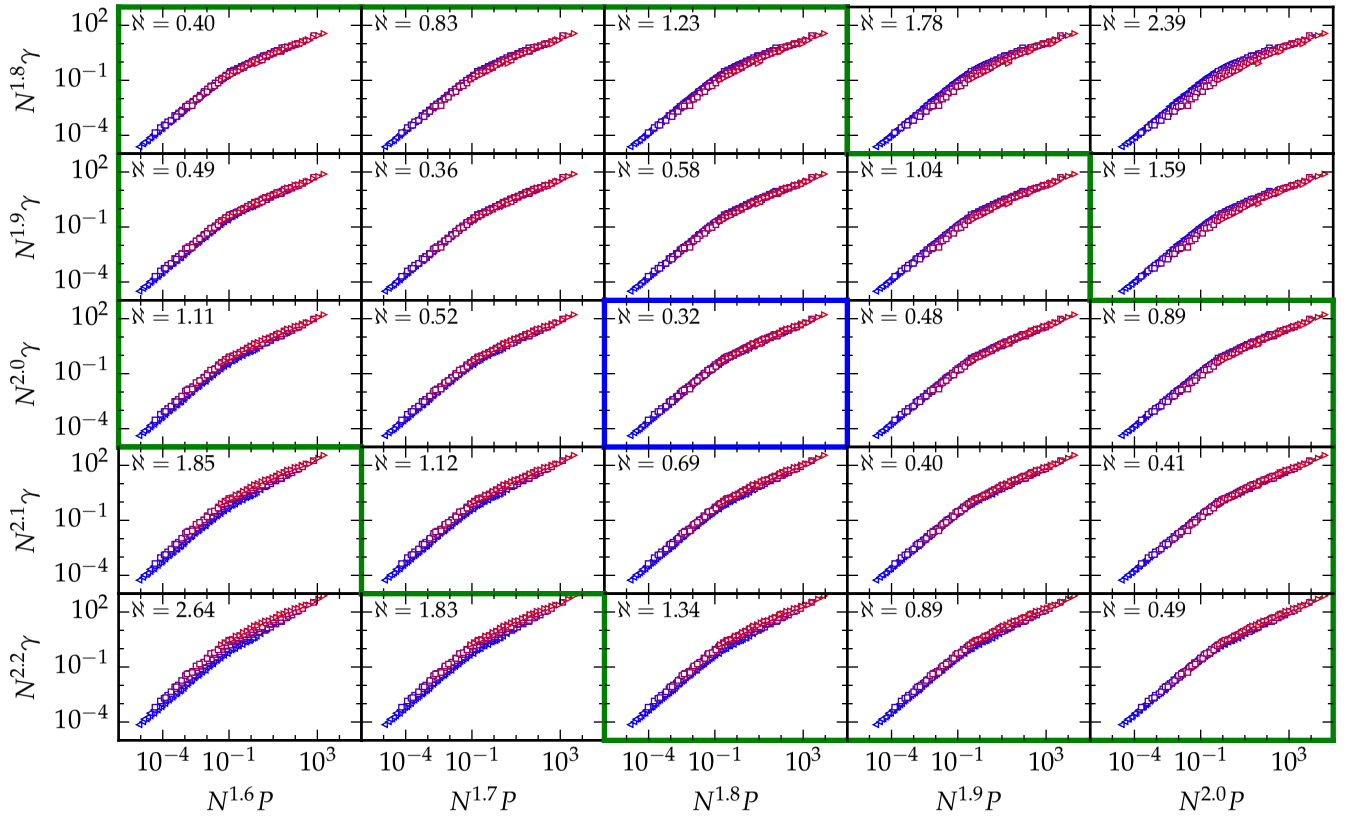

FIGURE 2.22: Alternate scaling plots for $N^q\gamma \sim F(N^rP)$, with $q = 1.8 \ldots 2.2$ (vertical) and $r = 1.6 \ldots 2.0$ (horizontal). $\aleph$ is a measure for collapse quality (see text), and the best collapse is found for $N^2\gamma \sim F(N^{1.8}P)$ (blue border), and all collapses with $0 \leq r - q \leq 0.4$ are reasonable (green border).

2.6 Alternative scaling models

In this section, we will discuss our findings in the light of alternative scaling approaches that have surfaced in the literature recently. First, we will investigate how accurately we can determine the power laws via scaling collapse of our data, and will compare the log corrections we applied in § 2.3.3 to power law corrections. Then, we will compare our results to work on contact changes in closely related model systems. Schreck et al. [76] have investigated nonlinearities in jammed packings at finite temperature, and found a different scaling law for the onset of contact changes that we attribute to their averaging over modes. Combe and Roux [79] and Lerner et al. [80] have approached the problem from a hard particle perspective, and found a scaling law very close to the behavior we find close to jamming. Finally, we will approach the problem from a statistical perspective. Starting from the distribution of γ_* of all contacts in all packings, we apply extreme value analysis to find the expected mean first contact change. We find that this does not yield a good prediction for the measured value, and determine that this cannot be explained by a few weak contacts, but rather points to correlations involving the whole system — i.e., the statistics of the first n contact changes in a system are different from the statistics of the *first* contact change in n systems.

Best collapse. Before describing the scaling functions found in other work, we will first investigate the range of scaling functions that gives an acceptable match to our data.

In § 2.3.3, we provided two arguments that predict the following scaling for the first contact change strain γ_{cc}:

$$N^2\gamma_{cc} \sim F\left(N^2P\right) \tag{2.75}$$

where $F(x) \sim x$ for small N^2P and $F(x) \sim x^{0.5}$ for large N^2P. In the same section, we have seen the results from the simulation collapse when plotted on these axes. Furthermore, we have seen that the collapse improves significantly by using the log correction

$$N^2\gamma_{cc} \sim F\left(N^2P\log_{10}(N)^{-0.7}\right) , \tag{2.76}$$

with the same $F(x)$.

First, we investigate for which exponents in N the collapse, without the log correction, is satisfactory, i.e., for what values of q and r does

$$N^q \gamma_{cc} \sim F\left(N^r P\right) \tag{2.77}$$

give an acceptable collapse? To make this quantitative, we measure the running maximum M (starting at low $N^r P$) and the running minimum m (starting at high $N^r P$), and calculate the effective area between the curves

$$\aleph = \int \left[\log_{10}(M(N^r P)) - \log_{10}(m(N^r P))\right] d\log_{10}(N^r P) \,, \tag{2.78}$$

where

$$M(x) = \max(N^q \gamma_{cc} | N^r P \leq x) \,, \tag{2.79}$$
$$m(x) = \min(N^q \gamma_{cc} | N^r P > x) \,. \tag{2.80}$$

In Fig. 2.22, we show collapse plots for $q = 1.8 \ldots 2.2$ and $r = 1.6 \ldots 2.0$. We observe that all plots with

$$r \leq q \leq r + 0.4 \tag{2.81}$$

are reasonable ($\aleph \lessapprox 1$), and that $N^2\gamma \sim F\left(N^{1.8}P\right)$ has the best overall scaling collapse ($\aleph = 0.32$). Our log-corrected collapse is very close to this, with $\aleph = 0.37$.

Second, we can wonder about the correct asymptotic behavior of $F(x)$. To find this behavior, we fit $F(x) = C \cdot x^\beta$ separately for both the upper ($N^{1.8}P > 10$) and lower ($N^{1.8}P < 0.1$) branches (Fig. 2.23(a)), and find

$$F(x) = \begin{cases} (1.7 \pm 0.1) \cdot x^{0.50 \pm 0.01} & (x \ll 1) \\ (2.7 \pm 0.3) \cdot x^{1.00 \pm 0.01} & (x \gg 1) \end{cases} \,, \tag{2.82}$$

which means that the best overall scaling of γ becomes

$$\gamma = \begin{cases} (1.7 \pm 0.1) \cdot P^{0.5} N^{-1.1} & (N^2 P \ll 1) \\ (2.7 \pm 0.3) \cdot P^1 N^{-0.2} & (N^2 P \gg 1) \end{cases} \,. \tag{2.83}$$

The error bars are given by the variation of the parameters when the fit range is increased or decreased by a decade. When p and q are varied within the collapse region, the exponents vary by $\sim \pm 0.05$.

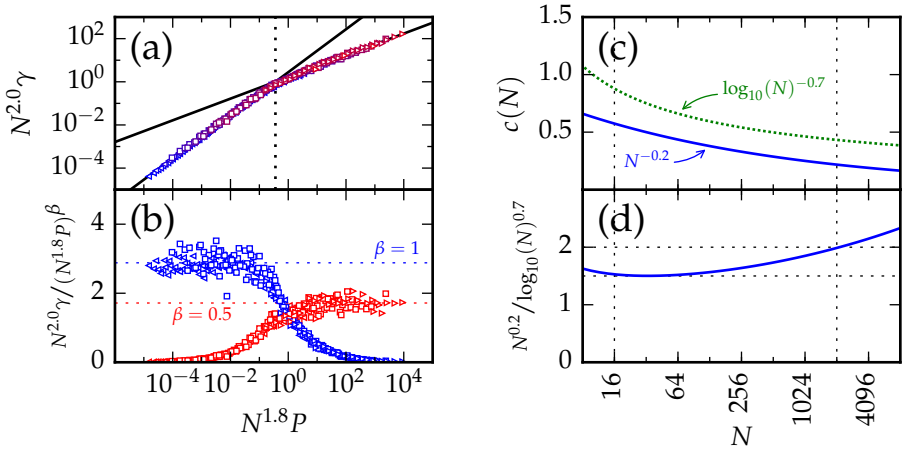

FIGURE 2.23: (a) Asymptotic behavior of $F(x)$. Black lines show the result from the power law fit: $F(x) \sim x^{1.0}$ for small x and $F(x) \sim x^{0.5}$ for large x. The crossover between the two regimes is at $x = 0.4$. (b) Residual plot $F(x)/x^{1.0}$ (blue) and $F(x)/x^{0.5}$ (red) show the fitted power laws match the behavior very well in their respective regimes, as they scatter around a constant value. (c) Log-correction $c(N) = \log_{10}(N)^{-0.7}$ and power law correction $c(N) = N^2/N^{1.8} = N^{-0.2}$ as function of system size N. Both vary roughly by a factor of two in the range of N we probe. (d) The ratio of the two varies by less than 35%.

When we compare the power laws to our expected scaling (Eq. (2.31)), we find the scaling of γ with P is as expected, but note two differences from the expected scaling of γ with N. First, we observe γ decreases as $N^{-0.2}$ for small systems, instead of the independence of N our scaling model predicted. Second, for large systems, we observe γ_{cc} scales as $N^{-1.1}$ instead of N^{-1}.

Comparison between power law and log corrections. We can interpret the 1.8 exponent in N as a correction to the predicted N^2P scaling: $N^{1.8}P = N^{-0.2}(N^2P)$. In Fig. 2.23(c), we compare this correction to the log correction described in § 2.3.3. We observe the corrections produce largely the same effect in the range of N that our simulations cover. When we plot the ratio of the two (Fig. 2.23(d)), we observe that the deviations between

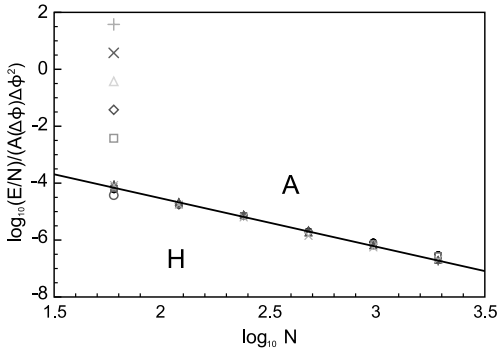

FIGURE 2.24: "The total energy per particle required to break a single contact averaged over k (scaled by $A(\Delta\phi)(\Delta\phi)^2$, where $A(\Delta\phi)$ is only weakly dependent on $\Delta\phi$) versus N for $\Delta\phi = 10^{-2}$ (crosses), 10^{-3} (pluses), 10^{-4} (triangles), 10^{-5} (diamonds), 10^{-6} (squares), and 10^{-7} (circles). The solid line has slope -1.7."
From Schreck et al. [76, Fig. 3(b)]; copyright 2011 by The American Physical Society.

both corrections are less than 35%, over a range where N^2 changes by three orders of magnitude.

It is thus very difficult to distinguish log corrections from power law corrections to scaling in 2D. To achieve a measurable difference of a factor three, systems of at least 60 000 particles are required. Alternatively, simulations can be performed in three dimensions, in which case log corrections will disappear [28].

To conclude, we find our deviations from the expected scaling can be described by both a log correction and a power law correction. Much larger systems or three-dimensional simulations are required to fully distinguish the two corrections.

2.6.1 Excited eigenmodes

We now turn to comparing our results to other work on contact changes in amorphous systems. We first focus on work by Schreck et al. [76], who investigated contact breaking in jammed sphere packings using excited eigenmodes. They displace particles along an eigenmode:

$$\vec{r} = \vec{r_0} + \sqrt{N}\delta\hat{e}_k \,, \tag{2.84}$$

where $\vec{r_0}$ is the original state, $\vec{r}$ the excited state, N the system size, $\hat{e}_k$ the eigenvector for eigenmode k, and δ the excitation amplitude. The system is then allowed to evolve at fixed energy. For small excitations δ, the system oscillates around a base state, and most energy is contained in the initial eigenmode. However, for excitations larger than a critical excitation amplitude $\delta_c(k)$ there is a sharp increase in how much energy spreads into the other eigenmodes of the system. Schreck et al. find that δ_c is directly related to the first contact change in the system. Surprisingly, they find that contacts only *break*, even for large systems ($N = 1920$) at high densities ($\Delta\phi = 10^{-2}$).

For each system, $\delta_c(k)$ is calculated for every eigenmode k. The authors then measure the average energy required to break a contact

$$E = \langle (\omega_k \delta_c(k))^2 \rangle_k \,, \tag{2.85}$$

where ω_k is the eigenfrequency of eigenmode k and the mean is taken over all eigenmodes.

Fig. 2.24 shows the scaling of the energy per particle E/N as a function of density $\Delta\phi$ and system size N. Schreck et al. find a relationship

$$\frac{E/N}{A(\Delta\phi)\cdot(\Delta\phi)^2} \sim N^{-\beta} \,, \tag{2.86}$$

"where $A(\Delta\phi)$ is only weakly dependent on $\Delta\phi$ and $\beta \approx 1.7$" [76]. Close to jamming ($N\Delta z = 0 \ldots 2$), they find $A(\Delta\phi)$ is constant and $\beta = 1 \ldots 2$ [98]. When we rewrite Eq. (2.86) in terms of E, take $A(\Delta\phi)$ as constant and use $\Delta\phi \sim P$, we find

$$E \sim N^{1-\beta}(\Delta\phi)^2 \sim N^{1-\beta}P^2 \,. \tag{2.87}$$

To compare this with our results, we note that

$$E \sim \sigma\gamma L^2 \sim \sigma\gamma N \sim GN\gamma^2 \,, \tag{2.88}$$

so

$$\gamma \sim \sqrt{E/GN} \sim N^{-\beta/2}PG^{-1/2} \,. \tag{2.89}$$

Using the known finite-size scaling of G [34], we then find

$$\gamma \sim \begin{cases} PN^{(1-\beta)/2} & (N^2P \ll 1) \\ P^{0.75}N^{-\beta/2} & (N^2P \gg 1) \end{cases} \,, \tag{2.90}$$

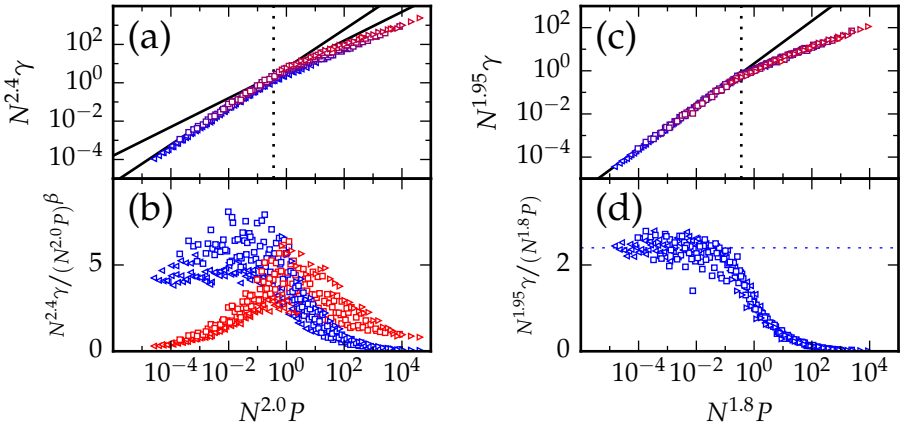

FIGURE 2.25: (a) Our data rescaled as in Schreck et al. [76] (Eq. (2.90)). Black lines indicate power laws with exponent 1 and 0.75. (b) The residuals $F(x)/x^{1.0}$ (blue) and $F(x)/x^{0.75}$ (red) do not have a plateau, indicating these power laws do not well describe the data. (c,d) Same, but with data rescaled as in Wyart [99] (Eq. (2.94)), where we have chosen $r = 1.8$, as in our best collapse. The corresponding $q = 1.8 + 0.15 = 1.95$ is indistinguishable from our best choice $q = 2.0$.

To test whether this matches the data, we plot $N^{(\beta+3)/2}\gamma$ as a function of N^2P in Fig. 2.25(a), using the published value $\beta = 1.7$. We find, firstly, that the collapse is not very good. Secondly, we find the 0.75 power law for the upper branch overestimates the actual strains. To a lesser extent, the lower branch also deviates from Eq. (2.90). This is also reflected in the residuals in Fig. 2.25(b) — neither branch collapses onto a constant value.

We expect these differences arise because Eq. (2.85) calculates the energy as an *average* over $2N$ modes within the same system. In § 2.6.3, we will see that averaging over all contacts loses many of the features we find for the first contact change.

2.6.2 Hard particle systems

The question of contact breaking and plasticity has also been studied in systems of hard particles. These systems are isostatic [100], which means a contact change is always a breaking event, and each breaking event will

cause the system to unjam. Contact changes are therefore directly connected to plastic events. Isostaticity also implies that the force distribution is unique, and can be derived directly from the contact network [101]. Because the systems are isostatic, the results can only describe the $N^2P \ll 1$ limit of soft particle systems.

Combe and Roux [79] investigated the prevalence of and distance between strain jumps in a system under uniaxial stress-controlled compression. The system is deformed by increasing σ_{yy} while keeping σ_{xx} constant. Combe and Roux find that the spacing between events is described by an exponential distribution in $\delta q(N/1024)^{1.16}$, where δq is the relative uniaxial stress increment $\Delta\sigma_{yy}/P$. This is consistent with modeling events as a Poisson process.

Because the mean of the distribution

$$\langle \delta q(N/1024)^{1.16} \rangle = \langle \Delta\sigma \rangle (1/P)(N/1024)^{1.16} \sim \text{constant} \tag{2.91}$$

is independent of N and P, the mean stress required to break the first contact scales as

$$\langle \Delta\sigma \rangle \sim P\langle \Delta q \rangle \sim P/N^{1.16} \,. \tag{2.92}$$

We can then calculate the γ_{bk} using the uniaxial compression modulus E. Using that $K \sim 1$ and $G \sim 1/N \ll K$ near jamming, E is given by [102]

$$E = \frac{4}{1/K + 1/G} \sim G \sim \frac{1}{N} \tag{2.93}$$

and the expected mean strain to break the first contact is thus given by

$$\gamma_{\text{bk}} \sim \langle \Delta\sigma \rangle / E \sim P/N^{0.16} \,, \tag{2.94}$$

which is very close to the $P/N^{0.20}$ scaling we found by fitting our data to a pure power law (Eq. (2.83)).

A theoretical argument for this power law, based on the concept of "weak" contacts that connect to local motion, and "strong" contacts that are connected to global motion, was introduced by Lerner et al. [80]. Wyart [99] uses this to predict that the strain for the first contact change should scale as

$$\gamma \sim P/N^{0.15} \,, \tag{2.95}$$

which is close to the value found by Combe and Roux [79].

In Fig. 2.25(c), we show this scaling also provides a good match to our data — the 0.15 exponent can be seen as a power law correction to our initial $\gamma \sim P$ scaling near jamming, and is essentially indistinguishable from either log or 0.2 power law corrections.

2.6.3 Extremal value scaling

In this section we probe whether we can predict the scaling of γ_{cc} and distribution of γ_* based on the distribution of all contact change strains $\rho(\gamma_{ij})$ for a given ensemble (N, P). Note that before (§§ 2.3 and 2.4), we have determined the scaling of γ_{cc} by determining γ_* *for each packing*, and averaging over those values. We found that the distribution of γ_* is close to a exponential distribution. Assuming that large enough packings are statistically similar, it should be possible to predict γ_{cc} from the distribution of $\rho(\gamma_{ij})$ using extremal statistics. In particular, one might expect that $\rho(\gamma_{ij})$ takes on a simple form for sufficiently large N, possibly even amenable to a theoretical description. Deviations from this picture may point to lack of self-averaging or other subtleties, and as such provide important information for developing a deeper theoretical understanding for the characteristic strains of the first contact change. Before starting, we note that for contact creation, it is difficult to establish which potential contacts should be considered, and we therefore focus on the breaking of contacts only, using $\gamma^{\mathrm{LR}}_{*,\mathrm{bk}}$ from linear response. We will also limit our discussion to contacts that break under shear in the positive direction, i.e., $\gamma > 0$. As a first probe of the usefulness of extremal value statistics for contact breaking, we compare the results of two distinct methods of calculating the mean contact breaking strain. First, we define $\gamma^{\mathrm{LR}}_{\mathrm{bk}} = \langle \gamma^{\mathrm{LR}}_{*,\mathrm{bk}} \rangle$, the mean of the contact breaking strains determined for an ensemble of packings, as we have done in § 2.4. Second, we determine $\gamma^{\mathrm{dist}}_{\mathrm{bk}}$ from the distribution of positive contact change strains $\rho(\gamma^{\dagger}_{ij})$ by solving

$$\frac{1}{\langle N_{\mathrm{bk}} \rangle} = \int_0^{\gamma^{\mathrm{dist}}_{\mathrm{bk}}} \rho(\gamma^{\dagger}_{ij}) d\gamma^{\dagger}_{ij} \, . \tag{2.96}$$

To implement this, we first compute the numerical CDF $\Pr(\gamma^{\dagger}_{ij} < \gamma)$ based on the breaking strain γ_{ij} for *every* contact in *every* packing in the ensemble and then solve

$$\Pr(\gamma^{\dagger}_{ij} < \gamma^{\mathrm{dist}}_{\mathrm{bk}}) = 1/\langle N_{\mathrm{bk}} \rangle \, , \tag{2.97}$$

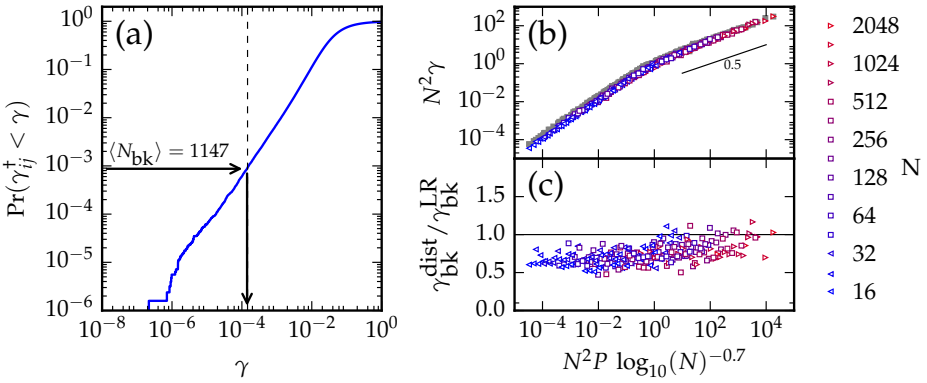

FIGURE 2.26: (a) CDF of $\gamma_{ij}^\dagger$ for every contact for every packing in the $N = 1024$, $P = 10^{-2}$ ensemble. The strain at which $\Pr(\gamma_{ij}^\dagger < \gamma_{\rm bk}^{\rm dist}) = 1/\langle N_c\rangle$ is the expected contact breaking strain for this ensemble: $\gamma_{\rm bk}^{\rm dist} = 1.4 \times 10^{-4}$. The mean breaking strain from linear response is $\gamma_{\rm bk}^{\rm LR} = 1.5 \times 10^{-4}$, and is indicated with the dashed line. (b) Colored symbols: resulting scaling of $\gamma_{\rm bk}^{\rm dist}$. Gray background: scaling of $\gamma_{\rm bk}^{\rm LR}$, as in Fig. 2.17(b). (c) The ratio $\gamma_{\rm bk}^{\rm dist}/\gamma_{\rm bk}^{\rm LR}$ varies slowly with $N^2P\ \log_{10}(N)^{-0.7}$, from $\gamma_{\rm bk}^{\rm dist}/\gamma_{\rm bk}^{\rm LR} \approx 0.5$ to $\gamma_{\rm bk}^{\rm dist}/\gamma_{\rm bk}^{\rm LR} \approx 1.0$.

where $\langle N_{\rm bk}\rangle \approx 0.5\langle N_c\rangle$ is the mean number of contacts that break under positive strain, for which we take the numerical ensemble average. This procedure is illustrated in Fig. 2.26(a) for the $N = 1024$, $P = 10^{-2}$ ensemble, where $\langle N_{\rm bk}\rangle = 1147$. For this particular example we find that $\gamma_{\rm bk}^{\rm LR} = 1.5 \times 10^{-4}$ whereas $\gamma_{\rm bk}^{\rm dist} = 1.4 \times 10^{-4}$. These values are close but distinct ($\gamma_{\rm bk}^{\rm dist}/\gamma_{\rm bk}^{\rm LR} = 0.93$) — as we will show below, there are systematic deviations between these numbers which provide insight into the statistics of contact breaking.

As comparison, we repeat this procedure for a synthetic ensemble of systems where all contacts are uncorrelated. To build this ensemble, we draw $N_{\rm bk} = 1147$ contacts for each of $N_s = 1000$ systems from the measured frequentist distribution of contact breaking strains $\rho(\gamma_{ij}^\dagger)$ of the $N = 1024$, $P = 10^{-2}$ ensemble (bootstrapping). For each system, we calculate the minimum strain γ_*. We then compare the mean breaking strain $\gamma_{\rm bk} = \langle\gamma_*\rangle = (1.34 \pm 0.04) \times 10^{-4}$ to $\gamma_{\rm bk}^{\rm dist} = 1.4 \times 10^{-4}$, and find

$\gamma_{\rm bk}^{\rm dist}/\gamma_{\rm bk} = 1.05 \pm 0.04 > 1$. Values below 1 thus indicate significant deviations from uncorrelated systems.

Distribution of strains. We now probe the *distribution* of strains of first contact breaks. Consider an ensemble of M packings of N particles, each with $N_{\rm bk}(m)$ contacts for which we calculate the breaking strains $\gamma_{ij}^{\dagger}$. This yields a total of $\Sigma_{m=1}^{M} N_{\rm bk}(m) \equiv M\langle N_{\rm bk}\rangle$ samples (values of $\gamma_{ij}^{\dagger}$), as illustrated in Fig. 2.27 for a synthetic data set, as well as for two data sets at fixed P and N. First, we can collect all breaking strains in a distribution $\rho(\gamma_{ij}^{\dagger})$ (black curves in panels b,e,h). As illustrated in Fig. 2.27 there are now two operations we can perform. Equivalent to what we do to determine $\gamma_{\rm bk}^{\rm LR}$ in linear response, we can determine the minimum breaking strain for each of the M packings, obtaining M breaking strains (red crosses in panels a,d,g) and the corresponding distribution $\rho(\gamma_{*,\rm bk}^{\rm LR})$ (shown as red curves in panels b,e,h, as a fraction of $\rho(\gamma_{ij}^{\dagger})$). Alternatively, we may also consider the M smallest values out of $M\langle N_{\rm bk}\rangle$ samples taken out of the distribution $\rho(\gamma_{ij}^{\dagger})$ (blue circles), which yields the distribution $\rho(\gamma_{<}) := \rho(\gamma|\gamma \leq \gamma_{\rm bk}^{\rm dist})$ (blue curve). The mean values considered above are related to these distributions as follows: $\gamma_{\rm bk}^{\rm LR}$ is the mean of the $\rho(\gamma_{*,\rm bk}^{\rm LR})$, whereas $\gamma_{\rm bk}^{\rm dist}$ is the *maximum* value of $\gamma_{<}$ in $\rho(\gamma_{<})$. Clearly, the distributions $\rho(\gamma_{*,\rm bk}^{\rm LR})$ and $\rho(\gamma_{<})$ in general will be different, but if the different packings are statistically indistinguishable and large enough to allow for self-averaging, so that $\gamma_{\rm bk}^{\rm LR} \approx \gamma_{\rm bk}^{\rm dist}$, these distributions are directly related (see below), which yields a statistical test on the nature of the contact breaking strains.

Results. We have determined $\gamma_{\rm bk}$ and $\gamma_{\rm bk}^{\rm dist}$ for all (N, P) ensembles. In Fig. 2.26(b) we plot $N^2\gamma_{\rm bk}^{\rm dist}$ vs $N^2 P\ \log_{10}(N)^{-0.7}$, and in Fig. 2.26(c) we plot the ratio $\gamma_{\rm bk}^{\rm dist}/\gamma_{\rm bk}^{\rm LR}$ vs $N^2 P\ \log_{10}(N)^{-0.7}$. At low $N^2 P\ \log_{10}(N)^{-0.7}$, we find that $\gamma_{\rm bk}^{\rm dist}$ and $\gamma_{\rm bk}^{\rm LR}$ exhibit similar scaling with $N^2 P\ \log_{10}(N)^{-0.7}$, but that their ratio $\gamma_{\rm bk}^{\rm dist}/\gamma_{\rm bk}^{\rm LR} \approx 0.6 < 1.05 \pm 0.05$ points to deviations from self-averaging. At very high $N^2 P\ \log_{10}(N)^{-0.7}$, $\gamma_{\rm bk}^{\rm dist}$ increases faster than $\gamma_{\rm bk}^{\rm LR}$ and appears to reach equality for the highest values of $N^2 P$ — we suggest that here the packings are large enough to be self-averaging.

To further characterize the origins of this breakdown of self averaging in small systems, we take a closer look at the distributions $\rho(\gamma_{*,\rm bk})$ and

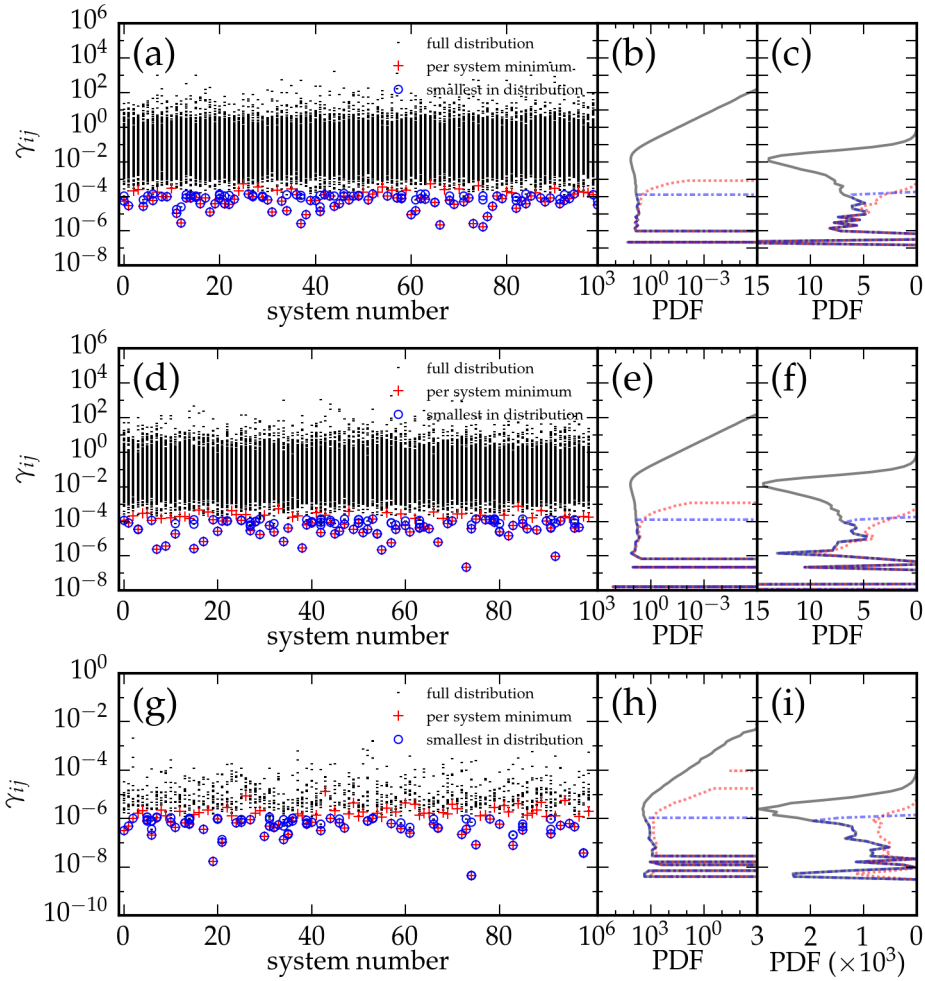

FIGURE 2.27: (a) Scatter plot of each positive contact breaking strain $\gamma_{ij}^{\dagger}$ for 100 synthetic systems drawn (bootstrapped) from the distribution $\rho(\gamma_{ij}^{\dagger})$ for $N = 1024$, $P = 10^{-2}$ (black dots). For each system, $\gamma_* \equiv \min \gamma_{ij}^{\dagger}$ is indicated with a red $+$. All values below the $1/N_c$ percentile are indicated with a blue $\circ$. (b) The PDF $\rho(x_{ij})$ (black). The distribution of per system minima ($\rho(\gamma_*)/M$, red dashed) and values below the $1/N_c$ percentile ($\rho(\gamma_<)/M$, blue dash-dotted) as part of the whole are indicated. (c) Same as (b), but with a linear PDF axis. (d,e,f) Same as (a,b,c), with numerical data from the $N = 1024$, $P = 10^{-2}$ ensemble. (g,h,i) Same, with numerical data from the $N = 16$, $P = 10^{-6}$ ensemble.

$\rho(\gamma_<)$ in Fig. 2.27 and 2.28. In Fig. 2.27(a–c), we plot each value of $\gamma_{ij}^\dagger$ for the first 100 systems in the synthetic ensemble described above. When we compare the PDFs of the per system $\rho(\gamma_{*,\mathrm{bk}})$ (red curves in panel b) and distribution minima $\rho(\gamma_<)$ (blue curves in panel b), we note they are similar for small values of $\gamma_{ij}^\dagger$, but different for larger values of $\gamma_{ij}^\dagger$.

In Fig. 2.28(a) we compare the CDF of the per system minima to the CDF of the whole distribution. In the synthetic data, we can deduce that the inverse CDF of minima $\Pr(\gamma_* \geq \gamma)$ relates to the CDF of the distribution $\Pr(\gamma_{ij} < \gamma)$ as

$$\begin{aligned}
\Pr(\gamma_* \geq \gamma) &= (1 - \Pr(\gamma_{ij} < \gamma))^{\langle N_{\mathrm{bk}} \rangle} \\
&= \left[1 - \frac{\#_{\gamma_{ij}<\gamma}}{N_s \langle N_{\mathrm{bk}} \rangle}\right]^{\langle N_{\mathrm{bk}} \rangle} \\
&\approx \exp(-\frac{\#_{\gamma_{ij}<\gamma}}{N_s}) \\
&= \exp(-\langle N_{\mathrm{bk}} \rangle \Pr(\gamma_{ij} < \gamma)) \,, \qquad (2.98)
\end{aligned}$$

for large enough $\langle N_{\mathrm{bk}} \rangle$ for a given $\langle N_{\mathrm{bk}} \rangle \Pr(\gamma_{ij} < \gamma)$. In Fig. 2.28(a), we plot $\Pr(\gamma_* \geq \gamma)$ as a function of $\langle N_{\mathrm{bk}} \rangle \Pr(\gamma_{ij} < \gamma)$ for both the synthetic distribution described above, as well as for a synthetic distribution with small $\langle N_{\mathrm{bk}} \rangle$. We observe the exponential scaling predicted in Eq. (2.98) for both. Hence, one expects 63% of the N_s per-system minima γ_* to be present in the set of N_s global minima $\gamma_<$.

In Fig. 2.27(d–f), we plot each value of $\gamma_{ij}^\dagger$ for the first 100 systems, taken from the $N = 1024$, $P = 10^{-2}$ ensemble. The relation between the PDFs of the per system $\rho(\gamma_{\mathrm{bk}}^{\mathrm{LR}})$ (red curves in panel e) and distribution minima $\rho(\gamma_<)$ (blue curves in panel e) are similar to those of the synthetic data, and $\gamma_{\mathrm{bk}}^{\mathrm{dist}} = 1.4 \times 10^{-4}$ and $\gamma_{\mathrm{bk}}^{\mathrm{LR}} = 1.5 \times 10^{-4}$ are quite similar. Consistent with this, a plot of $\Pr(\gamma_* \geq \gamma)$ as a function of $\langle N_{\mathrm{bk}} \rangle \Pr(\gamma_{ij} < \gamma)$ is approximately exponential, although slight deviations can be seen in the tails of these distributions (Fig. 2.28(b)).

In Fig. 2.27(g–i), we plot each value of γ_{ij} for the first 100 systems, taken from the $N = 16$, $P = 10^{-6}$ ensemble. The differences between the PDFs of the per system $\rho(\gamma_{\mathrm{bk}})$ (red curves in panel h) and distribution minima $\rho_<(\gamma_{\mathrm{bk}}^{\mathrm{dist}})$ (blue curves in panel h) are more significant, and $\gamma_{\mathrm{bk}} = 1.6 \times 10^{-6}$

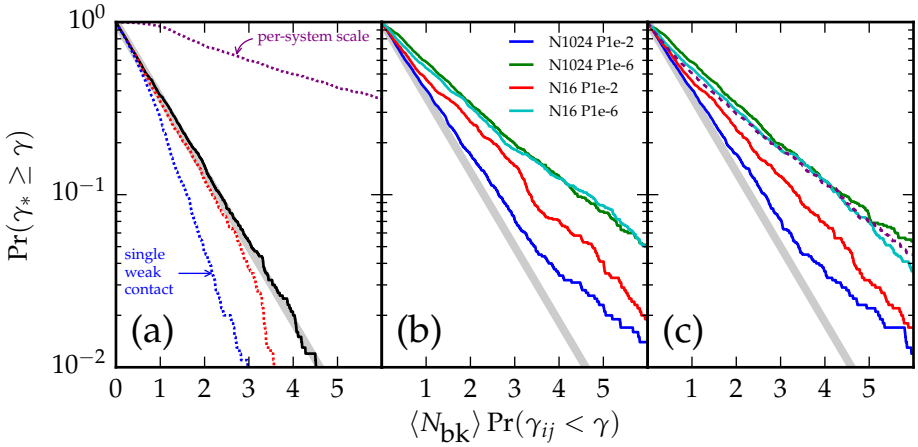

FIGURE 2.28: $\Pr(\gamma_* \geq \gamma)$ as a function of $\langle N_{\rm bk} \rangle \Pr(\gamma_{ij} < \gamma)$ (see text). (a) Solid black curve: Synthetic data, drawn from $\rho(\gamma_{ij}^{\dagger})$ in the $N = 1024$, $P = 10^{-2}$ ensemble ($\langle N_{\rm bk} \rangle = 1147$). For the same ensemble, data with a single value from a distribution with lower mean (dot-dashed blue curve) and for systems with an overall per-system scale (dashed purple curve) are also shown. Dotted red curve: Synthetic data, from $\rho(\gamma_{ij}^{\dagger})$ in the $N = 16$, $P = 10^{-6}$ ensemble ($\langle N_{\rm bk} \rangle = 16$). The gray line indicates $\Pr(\gamma_* \geq \gamma) = \exp(-\langle N_{\rm bk} \rangle \Pr(\gamma_{ij} < \gamma))$. (b) Data from our simulations. We observe the curves decay *slower* than exponential, indicating correlations between contacts. (c) Data from (b), but with all strains rescaled to the mean of strains within one system. This reduces the effect of a per-system scale (dashed purple curve), but does not completely negate it. The behavior for the packing-derived data is unchanged as compared to (b).

and $\gamma_{\rm bk}^{\rm dist} = 1.1 \times 10^{-6}$ are quite distinct. Consistent with this, a plot of $\Pr(\gamma_* \geq \gamma)$ as a function of $\langle N_{\rm bk} \rangle \Pr(\gamma_{ij} < \gamma)$ deviates significantly from an exponential (Fig. 2.28(b)). This deviation points to a lack of self-averaging in small systems.

Interpretation. We now discuss two possible scenarios to explain the deviations for small $N^2 P \log_{10}(N)^{-0.7}$. First, each finite packing could have a different distribution of γ_{ij}, but between packings these distributions are related by an overall scale factor. The data shown in Fig. 2.27(g) suggests that this is possible. To understand the effect of such 'overall scale factor' for the statistics, we draw an overall system scale from a uniform distribution

$\mathcal{U}(0,1)$ for each of the synthetic systems, and multiply the strains for each system with this scale factor. The resulting behavior is shown in Fig. 2.28(a), where we see the decay is much slower than for uncorrelated systems. The reason for this is that packings with a low minimum will typically come from a system which contains other low strains. This saturates the low strain region of the overall distribution with strains that are not system minima. The data extracted from our direct simulations (Fig. 2.28(b)) show a similar decay, slower than exponential, with slower decays for lower pressures. To directly check whether a per-system scale *can* explain the behavior, we divide all strains by the mean strain for each system, and show the results in Fig. 2.28(c). In the case of a simple scale incorporated in synthetic data, this brings the behavior closer to the simple exponential (dashed purple line). The behavior is still not purely exponential because this normalization step overcorrects deviations. Nevertheless, we note that the rescaling has very little effect on the contact change strains shown in Fig. 2.28(b). We therefore conclude the correlations cannot be simply explained by an overall system scale.

Second, inspired by Lerner et al. [103], we now investigate whether we can recover the behavior of $\gamma_{\mathrm{bk}}^{\mathrm{LR}}$ using extremal value statistics by assuming that most contacts are drawn from a distribution with mean k, but a limited number of 'weak' contacts are drawn from a distribution with mean $k' \ll k$. In the case of one extraordinarily weak contact in each packing, we expect most of the k system minima to show up in the lowest k values of the entire set of strains. We have simulated this by dividing one strain in each of the synthetic packings by 10^3. As we see in Fig. 2.28(a), $\Pr(\gamma_* \geq \gamma)$ decreases much more rapidly than exponential, and drops to $\Pr(\gamma_* \geq \gamma) = 0$ around $\langle N_{\mathrm{bk}} \rangle \Pr(\gamma_{ij} < \gamma) \approx 3$ — in other words, the k minima are all found in the lowest $3k$ values of the full set. The exact point of intersection depends on how weak the contact is, and on how many weak samples are in the packing. However, our data for actual packings shows a *slower* than exponential decay, thus discounting the 'weak contact' hypothesis as source for the correlations in our systems.

Hence, in conclusion: for sufficiently large systems, packings are self averaging, and extremal value statistics may be sufficient to determine the mean value and distribution for the first contact break strains. For small systems, correlations between contacts need to be taken into account for a correct prediction.

Appendix

2.A Finite size scaling of $\rho(u_\parallel)$ and $\rho(u_\perp)$

In this appendix, we will discuss the distributions of $u_\parallel$ and $u_\perp$, which provide a continuum description of the inter-particle motion. For each particle pair i, j, we split the inter particle velocity $\overrightarrow{u_{ij}} = \partial\overrightarrow{x_{ij}}/\partial\gamma$ in components parallel and perpendicular to the contact:

$$u_{\parallel,ij} = \overrightarrow{u_{ij}} \cdot \hat{r}_{ij} \,, \tag{2.99}$$

$$u_{\perp,ij} = \sqrt{u_{ij}^2 - u_{\parallel,ij}^2} \,. \tag{2.100}$$

Using every contact in every packing in an ensemble, we then build the frequentist distributions $\rho(u_\parallel)$ and $\rho(u_\perp)$.

In the following, we will discuss the relationship between the shape and scale of these distributions and N and P. Earlier work [31] has focused on Hertzian systems at intermediate to high pressure ($P^{2/3} \sim \langle\delta\rangle \geq 3 \cdot 10^{-4}$). They find the shape of the distribution does not depend on P, and find a simple single scaling of the overall scale with P. We extend this with harmonic systems much closer to jamming ($P \sim \langle\delta\rangle \geq 10^{-7}$). At high pressures, we recover the same behavior, but close to jamming, we find *(i)* the shape of the distributions depends on the pressure P, and *(ii)* the widths of the distributions scale with N^2P, with two distinct scaling regimes.

Shape of distributions. In Fig. 2.29, we plot the probability density functions of $u_\parallel$ and $u_\perp$, rescaled by their standard deviations $s_\parallel$ and $s_\perp$, for ensembles with different system sizes and pressures. We note that, even though the different distributions cannot be collapsed with a single scale parameter, the majority of the behavior is captured in the standard deviation s. For both distributions, we observe the distributions become increasingly peaked near 0, and, although neither PDF diverges, their peaks appears to develop a sharp kink for small pressures. We observe the shape changes with P, and, for large enough N, is largely independent of N — N^2P is not the relevant scaling parameter here. Surprisingly, this means the overabundant low values are still present for large systems at $P \approx 10^{-3}$, which would normally not be considered 'close to jamming'.

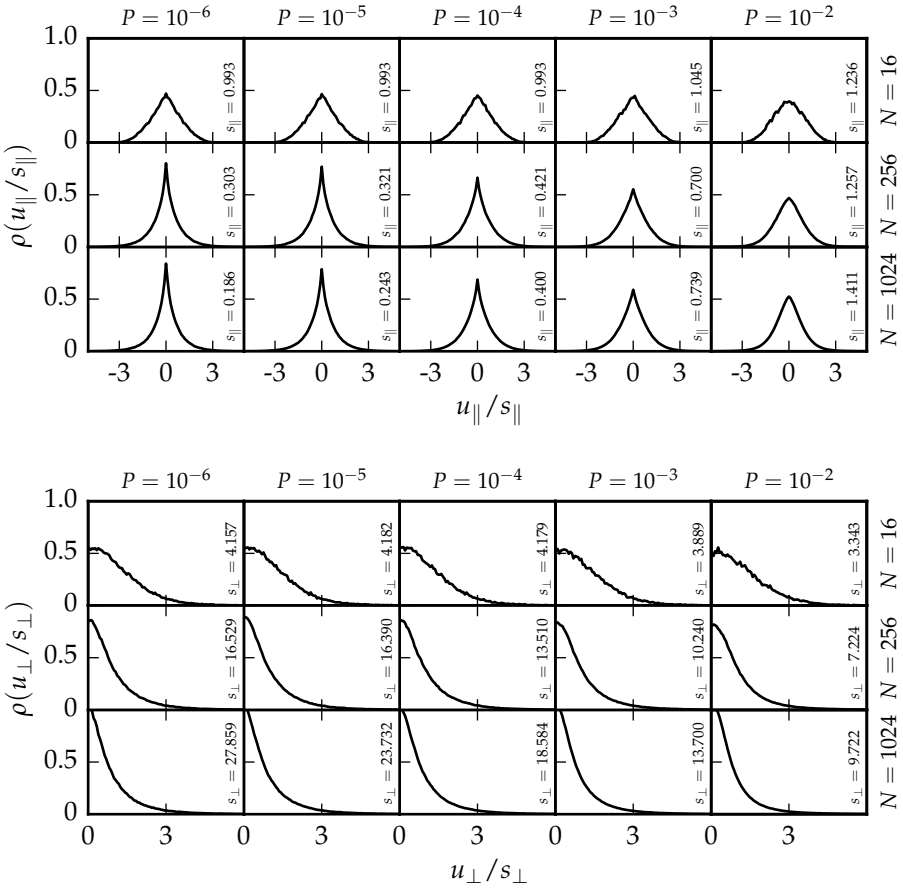

FIGURE 2.29: (top) Distributions of $u_\parallel$, rescaled by their standard deviation $s_\parallel$, for ensembles with $N = 16$, 256, or 1024 particles at $P = 10^{-6} \ldots 10^{-1}$. $s_\parallel$ is indicated in each figure. The distributions develop a sharp kink around 0 for low pressures, and become smooth for $P \gtrapprox 10^{-2}$. There is a weak dependence on N, with the distribution becoming more peaked for high N. (bottom) Same, for $u_\perp$. Here, the distributions depend less on N and P, although also here the distribution gains weight near 0 for decreasing P.

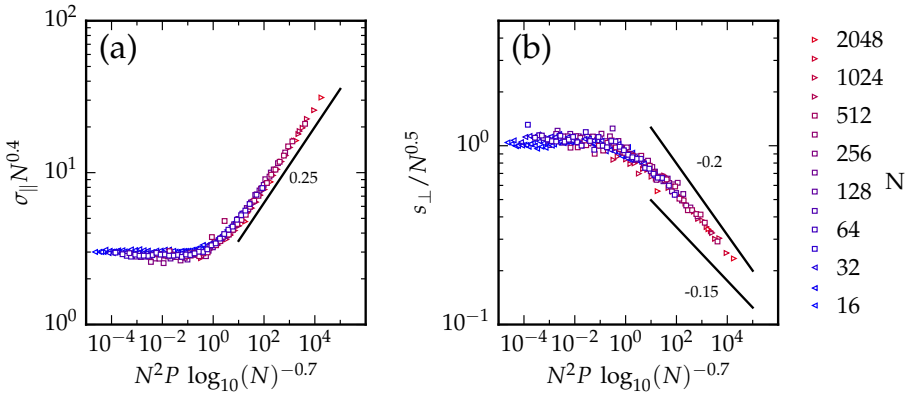

FIGURE 2.30: (a) Scaling of the standard deviation $s_\parallel$ as a function of N and P. At low N^2P, $s_\parallel$ is independent of pressure and at high N^2P we recover $s_\parallel \sim \delta^{0.25}$, consistent with [31]. (b) Same, for $s_\perp$. At low N^2P, $s_\parallel$ is independent of pressure. At high pressure we find a scaling $s_\parallel \sim \delta^{-0.2\ldots-0.15}$, somewhat slower than the $\delta^{-0.25}$ found in [31].

Scaling of standard deviations. Ellenbroek et al. [31] find the width of the distributions scale as

$$s_\parallel \sim \langle\delta\rangle^{1/4}\,, \tag{2.101}$$

$$s_\perp \sim \langle\delta\rangle^{-1/4}\,, \tag{2.102}$$

where $\langle\delta\rangle$ is the mean overlap between pairs of particles in contact in the ensemble. If we assume *(i)* the standard deviations will scale with N^2P and *(ii)* the distributions are independent of N for large N, Eq. (2.101) and Eq. (2.102) suggest plotting

$$N^{0.5} s_\parallel \sim F(N^2P)\,, \tag{2.103}$$

$$N^{-0.5} s_\perp \sim F(N^2P)\,, \tag{2.104}$$

should collapse our data. We note that, because the shape of the distribution varies, the choice of the measurement (e.g. a percentile rather than the standard deviation) can have a rather large effect on the collapse (which can reach ± 0.2 in the scaling exponent), and we therefore do not expect a perfect match.

In Fig. 2.30(a), we find the best scaling collapse for $s_\parallel$ is close but not equal to the expected scaling: we find $s_\parallel \sim N^{-0.4}$ at low N^2P rather than $s_\parallel \sim N^{-0.5}$. Nonetheless, we suggest that the scaling is close enough to be consistent with the proposed scaling. At low pressures, we find that $s_\parallel$ only depends on N, and no longer depends on P. For $N^2P \gg 1$, we find the expected $s_\parallel \sim P^{0.25}$ power law.

For $s_\perp$, we find Eq. (2.104) provides a rather good collapse (Fig. 2.30(b)). At low N^2P, we find $s_\perp$ becomes independent of P, and at high N^2P, we find behavior similar, but different from the expected $s_\perp \sim P^{-0.25}$ power law.

Surprisingly, we find both $s_\perp$ and $s_\parallel$ reach a pressure-independent plateau for low N^2P. This has important implications for the behavior close to jamming — in contrast to what is generally assumed, $s_\perp/s_\parallel$ does *not* diverge for low pressures, but reaches a plateau whose value diverges as $s_\perp/s_\parallel \sim N^{0.9}$ in the thermodynamic limit.

CHAPTER 3

REARRANGEMENTS IN SHEARED DISORDERED SOLIDS

A paper based on the work presented in this chapter is in preparation as:

[104] Merlijn S. van Deen, Sven Wijtmans, M. Lisa Manning and Martin van Hecke *Rearrangements in Sheared Disordered Solids*.

In this chapter, we propose a framework for investigating the characteristics of plasticity in amorphous, athermal, frictionless packings using numerical simulations. Using quasi-static shear under constant packing fraction, we have started investigating the nature of non-smooth events and their reversibility. We will discuss three properties of plasticity. First, contact change events can be classified into network events, where the particle motion is continuous but not smooth, and rearrangements, associated with discontinuous jumps in position, energy and stress. Second, events can be classified as line reversible, loop reversible or irreversible under cyclic strain. Finally, we propose classifying the behavior under stress relaxation, i.e., whether the system relaxes back to the same zero stress state before and after an event. We predict a strong relationship between the type of event, i.e., network events or rearrangements, and the (ir)reversibility of the event. We will show preliminary data on the classification of events in network events and rearrangements, and will propose steps to connect the event classification to reversibility measures.

3.1 Introduction

All solids will fail and flow if a large enough shear stress is applied. In disordered solids such as granular materials, foams, and dense colloids, a wide range of different failure type phenomena have been observed, depending on material preparation, packing fraction, pressure and applied stress. These range from gradual weakening phenomena [65, 97], to failure via localized rearrangements [75], large-scale avalanches [52, 69, 105] and the formation of shear bands [106–110]. To make predictions about failure, many continuum models [111–115] make assumptions about the statistics of a solid's complex potential energy landscape and how shear drives the system to explore mechanically stable minima within that landscape. However, there is no universally-accepted definition of which events take a particle packing to a "different state". It is thus critically important to characterize the elementary events that allow a solid to explore different mechanically stable states.

What elementary events can one observe in sheared disordered solids? In systems where the interaction potential is zero if two particles are not touching, changes to the load bearing particle contact network define one class of events [65, 116, 117]. Whether contact changes alone are sufficient to explore distinct minima in the potential energy landscape [116, 117] is not clear, but it is known that contact changes are not necessarily sufficient to drive the system towards the type of instability which causes discontinuous particle rearrangements and stress drops [35, 52, 116, 118, 119], and these instabilities therefore constitute a distinct type of event. Moreover, the precise nature of the (ir)reversibility of these events is subtle. Simulations and experiments under periodic strain have revealed that rearrangements can be *(a)* irreversible: particles end up in a different position from where they started, *(b)* loop reversible: particles end up in the same position but go back via a different path, or *(c)* line reversible: particles end up in the same position and traverse the same path [35]. Crucially, macroscopic properties, as well as the ability to encode memories [87, 120] depend on whether rearrangements are reversible or not [20, 35, 121]. It is however not immediately clear how to connect (ir)reversibility to the difference between contact changes and rearrangements. Finally, the phenomenology of fluctuations, plastic events and failure appears to change significantly between fragile systems close to jamming and more elasto-plastic systems

far away from jamming [38, 42, 97]. However, the effect of pressure on the nature and prevalence of different events is unexplored.

In this chapter, we focus on unambiguously classifying events in a simple model granular solid. We would like to understand the properties of these events, and how the frequency of each type depends on distance to jamming. We propose two major categories of events involving contact changes, which we denote network events and rearrangements. Rearrangements are associated with measurably non-zero changes in shear stress, energy, and particle positions. Network events correspond to changes in the contact network, with no associated discontinuity in the stress, energy, or particle positions.

To classify reversibility, there are several natural strategies. From an experimental point of view, relaxing to zero strain or to zero stress are obvious candidates. From the view of contact changes, one can consider shearing back to the previous contact change, or to the last plastic event. In this chapter, we will discuss reversibility under two different protocols: we will first discuss shearing back to the previous contact change, and will then discuss relaxing to zero stress.

3.2 Methods

We will now discuss the numerical simulations used to find contact changes at various pressures. We use the same simulation code as described in § 2.2. However, we now continue our simulations beyond the first contact change, until we find 25 events (up to 50 events at the lowest pressures). For each event i, we store the particle positions before ($\vec{r}_i^{\,-}$) and after ($\vec{r}_i^{\,+}$) the event, as well as the energy (U_i^-, U_i^+) and shear stress ($\sigma_{xy,i}^-$, $\sigma_{xy,i}^+$). We will show that these can be used to classify events as either a network event, where these are all continuous, or a rearrangement, where these are all discontinuous. We have generated 100 packings of $N_p = 512$ particles for a range of pressures $P = 10^{-7}$ to 2×10^{-1}, for a total of 2500–5000 events per ensemble. We use a larger range in pressure than before, as we expect an influence of localized behavior far from jamming. To probe reversibility under stress and strain controlled protocols, we use a different set of boundary conditions with the same energy minimization routines. We will describe these algorithms in detail in the sections on reversibility.

	continuity as function of γ			
	$\vec{r_i}$	U	σ_{xy}	G
between events	C^∞	C^∞	C^∞	C^∞
network event	C^0	C^1	C^0	$-$
rearrangement	$-$	$-$	$-$	$-$

TABLE 3.1: Classification of events based on continuity of extensive variables. In between events, all variables are smooth (C^∞). At a network event, the particle positions and σ_{xy} are continuous but non-differentiable (C^0), while the energy, a quadratic function of overlaps, is once differentiable (C^1). $G = \partial\sigma_{xy}/\partial\gamma$ is discontinuous. Finally, during a rearrangement, all variables are discontinuous.

3.3 Classification of contact changes

We now focus on the classification of contact changes: which differences do we expect between simple, continuous contact changes, *network events*, and discontinuous events, *rearrangements*? First, we investigate which behavior we expect from theoretical considerations. In § 3.5, we will show preliminary numerical data on the distinction.

We start by noting that the energy is a smooth function of the overlaps δ_{ij}:

$$U = \sum_{i,j} \frac{k}{2} \delta_{ij}^2 \,, \tag{3.1}$$

which implies that discontinuities in U correspond to discontinuities in δ_{ij}. δ_{ij} can be discontinuous for two reasons. First,

$$\delta_{ij} = \begin{cases} R_i + R_j - |\vec{r_{ij}}| & \text{if } |\vec{r_{ij}}| < R_i + R_j, \\ 0 & \text{otherwise.} \end{cases}$$

is inherently non-differentiable but continuous (C_0) at $|\vec{r_{ij}}| = R_i + R_j$, i.e., at a contact change. Secondly, δ_{ij} can be discontinuous when $\vec{r_{ij}}$ is discontinuous, i.e., if at least one of the particles i and j moves discontinuously as a function of strain γ.

Once we know the behavior of the particles, the behavior of U, σ and G follows directly — see Table 3.1. *(i)* In the absence of contact changes, particle positions are completely smooth and differentiable (C^∞), and so are

the overlaps, energy, stress and shear modulus. We have confirmed this to be the case in our simulations. *(ii)* At a network event, $|\vec{r_{ij}}| = R_i + R_j$, and δ_{ij} is non-differentiable (C_0). We therefore expect U to be singly differentiable (C_1), σ_{xy} to be non-differentiable, and $G = \frac{\partial}{\partial\gamma}\sigma_{xy}(\gamma)$ to be discontinuous. This is consistent with our observations in § 2.5.1. Although there is no a priori requirement for particle positions to be non-smooth, we observe they are also C_0. This makes sense, as the creation or disappearance of a contact discontinuously changes the eigenmodes, and therefore also the particle motion in response to (shear) deformation. *(iii)* It is also conceivable that the energy is continuous but not differentiable, which implies that the particles, stress and shear modulus are discontinuous. We believe there is no physical situation corresponding to this, as U is not the integrand of δ_{ij}, but the sum of δ_{ij}^2 — the square of a discontinuous function is still discontinuous. *(iv)* Finally, at a rearrangement, the discontinuity stems from discontinuous particle positions. As a consequence, δ_{ij}, U, σ_{xy} and G will all be discontinuous. Inversely, we have seen that U and σ_{xy} *cannot* be discontinuous at a network event, and a discontinuous jump in energy or stress is therefore a clear indication of a rearrangement event.

3.4 Reversibility

In sections 3.4.1 and 3.4.2 below, we will discuss two methods to classify (ir)reversibility. We can understand the behavior under forwards shear as a sequence of events connected by energy branches. At an event, the system can jump from one branch to another (Fig. 3.1), and this is where we expect to see irreversibility.

First, we will focus on reversibility under strain cycling. To probe the reversibility of event i, we start just after the last event before i, i.e., at γ_{i-1}^{+}. We then strain forwards, via γ_i, to just before the next event, i.e., to γ_{i+1}^{-}, and record the particle positions at discrete values of γ. From there, we strain back to γ_{i-1}^{+}, passing by the exact same strain values. We can then distinguish three different behaviors: (i) line reversible behavior, where the system follows the exact same path back, (ii) loop reversible behavior, where the system follows a different path, but returns to the original path, or (iii) irreversible, where the system never returns to the original path. In § 3.4.1, we will discuss this protocol in more detail.

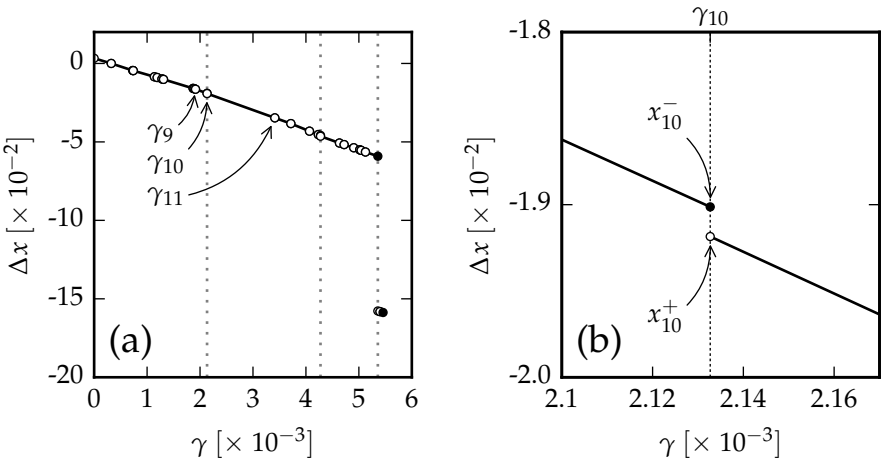

FIGURE 3.1: A single particle coordinate as function of strain during forward shear. Each event is indicated by a pair of circles: the closed circle indicates the position before the event and the open circle indicates the position after the event. For a network event, these circles coincide, and the closed circle is obscured by the open circle. (a) All 25 events for a system at $P = 10^{-2}$. Three rearrangements are indicated with dotted lines. The first rearrangement (event 10) is indicated, as well as the last event before and the first event after the rearrangement. (b) Zoom-in on the first rearrangement at $\gamma_{10} \approx 2.13 \times 10^{-3}$. We observe a clear discontinuous jump between the particle position before (x_{10}^-) and after (x_{10}^+) the event.

In § 3.4.2, we focus on reversibility under stress relaxation. One of the most natural concepts of plasticity is yielding: will the system move back when it is 'let go'? To determine whether a system yields at an event, we determine the reversibility under stress relaxation. Instead of prescribing the strain γ, we let the simulation minimize the energy also with respect to γ, which will relax the shear strain [34]. This will typically involve larger strains than strain reversal, and we therefore expect some events to be classified as strain irreversible, yet stress reversible.

With these protocols in place to test strain and stress reversibility, it becomes possible to correlate the event type, i.e. network events and rearrangements, to reversibility, and to map the relative prevalence of reversible and irreversible events for each, and this is the focus for future work.

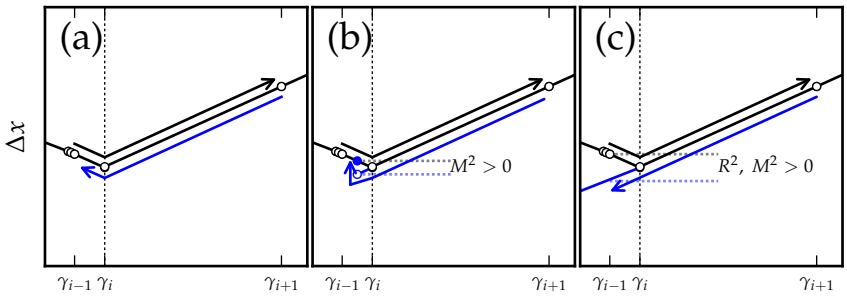

FIGURE 3.2: A single particle coordinate as function of strain during the strain cycle around event i (marked with a black dotted line). We start at γ_{i-1}^{+}, strain forwards until γ_{i+1}^{-} (black arrow), and strain back to γ_{i-1}^{+} (blue arrow). (a) In the case of a line reversible event, we follow exactly the same path forwards and backwards. Here, both $R_{i,\gamma}^2$ and $M_{i,\gamma}^2$ are small. (b) In a loop reversible event, the system jumps to a different branch, and returns back to the original branch between γ_i^{-} and γ_{i-1}^{+}. The maximum distance $M_{i,\gamma}^2$ is large, but the final distance $R_{i,\gamma}^2$ is small again. (c) An irreversible event does not return to the original branch. Here both $R_{i,\gamma}^2$ and $M_{i,\gamma}^2$ are large. Note that this figure is not meant to imply that Δx is smooth at γ_i — as a matter of fact, we expect non-smoothness for loop reversible and irreversible events (b and c).

3.4.1 Strain cycle reversibility

In this section, we will propose a protocol to probe reversibility of events using a strain cycle. Straining in a loop around γ_i, we accurately record the followed paths, and distinguish loop and line reversible events from irreversible events. The detailed procedure for the strain cycle is illustrated in Fig. 3.2. To probe the reversibility of an event i, we start just after event $(i-1)$, at $(\gamma_{i-1}^{+}, \overrightarrow{r_{i-1}}^{+})$. We then strain forwards, passing γ_i and continuing to γ_{i+1}^{-}, i.e., just before the next event. From there, we strain back, passing over exact the same strain values. For each event i, this provides us with a forwards path $\vec{r}_{\uparrow}(\gamma)$ and a backwards path $\vec{r}_{\downarrow}(\gamma)$ for each particle. We now calculate two quantities. First, we calculate the mean squared displacement between the forwards and backwards paths at the initial strain γ_{i-1}^{+}

$$R_{i,\gamma}^2 = \left\langle |\vec{r}_{\uparrow}(\gamma_{i-1}^{+}) - \vec{r}_{\downarrow}(\gamma_{i-1}^{+})|^2 \right\rangle , \tag{3.2}$$

where the average is taken over all particles. We use $R^2_{i,\gamma}$ as a measure of overall reversibility: we have returned to the same initial state if $R^2_{i,\gamma} = 0$. In practice, we have to define a finite cutoff due to numerical noise. Second, we calculate the maximum mean squared displacement during the full cycle

$$M^2_{i,\gamma} = \max_{\gamma^+_{i-1} \le \gamma \le \gamma^-_{i+1}} \left\langle |\vec{r}_\uparrow(\gamma) - \vec{r}_\downarrow(\gamma)|^2 \right\rangle , \tag{3.3}$$

which we use to distinguish line reversible from loop reversible events: if the event is line reversible, the maximum distance is $M^2_{i,\gamma} = 0$ (up to numerical noise), while it is finite for a loop reversible event. Combined, we define three categories: (i) line reversible, where both R^2 and M^2 are small, (ii) loop reversible, where R^2 is small, but M^2 is large, and (iii) irreversible, where both R^2 and M^2 are large.

To correlate the type of event to the reversibility, we return to our discussion on the continuity of particle motion. In the case of network events, particle motion is fully continuous, and it is hard to imagine that they would be irreversible. We thus expect network events to be line reversible. At the same time, discontinuities are normally associated with hysteresis: the instability of the system at γ^-_i that leads to a jump towards a new state at γ^+_i should not cause the state at γ^+_i to be similarly unstable under backwards shear. We thus expect all rearrangements to be either loop reversible or irreversible.

3.4.2 Reversibility under stress

In this section, we explain how to determine whether the system is stress reversible, i.e., whether the relaxation of the system to zero shear stress brings us to a different state depending on whether we start just before or just after the event. If we find a different relaxed state, we can say that the system has yielded at the event.

We use our numerical simulations to determine the stress relaxation. Starting at a given γ and $\vec{r}$, we find a minimum in energy with respect to both the particle positions *and* strain γ. The other boundary conditions, i.e., the box size L^2 and the pure shear parameter δ, are kept constant (see § 2.2). In this way, we find a corresponding relaxed state with $\sigma_{xy} = 0$ for each given state. For each pre-event state $(\gamma^-_i, \vec{r}^{\,-}_i)$, we calculate the corresponding relaxed state $(\gamma^{-,R}_i, \vec{r}^{\,-,R}_i)$, as shown in Fig. 3.3. To

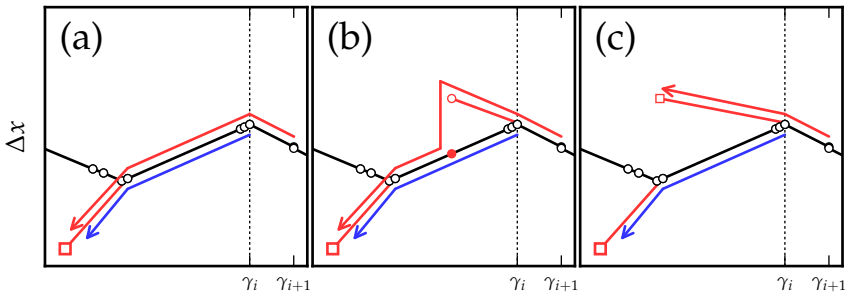

FIGURE 3.3: A single particle coordinate as function of strain while probing the stress relaxation of event i (marked with the black dotted line). During stress relaxation, the system relaxed to a state with zero shear stress (red square). The zero shear stress state does not have to lie on the original forwards path. When starting at γ_i^-, the system relaxes to the state in the bottom left corner (blue arrow). We show three cases for relaxation when starting at event γ_{i+1}^- (red arrow). (a) If the system is line reversible, we follow the exact same path. (b) In the case of loop reversibility, the system initially follows a different paths, but jumps back to the same branch and ends up at the same zero stress state. (c) In the case of irreversibility, the system relaxes to a different zero stress state (small red square). Cases (a) and (b) relax into the same zero-stress state and are marked *reversible*; (c) relaxes into a different state and is marked *irreversible*.

determine whether event i is reversible under stress, we compare the relaxed state when starting just before the event to the relaxed state when starting just before the *next* event, and calculate the mean squared distance between the two:

$$R^2_{i,\sigma} = \left\langle |\overrightarrow{r_{i+1}}^{-,R} - \vec{r}_i^{-,R}|^2 \right\rangle \ , \tag{3.4}$$

where the average is taken over all particles. As before, this allows us to distinguish reversible from irreversible events. Distinguishing between line reversible and loop reversible is not easy, because the stress relaxation algorithm does not follow the same strain increments for different relaxations. Nonetheless, we sketch the resulting behavior in these three categories in Fig. 3.3.

3.5 Preliminary results

In this section, we will present and discuss preliminary work on the classification of contact changes. Afterwards, we will discuss our expectations for reversibility and their connection to the different event types.

3.5.1 Classification of events

We will now focus on the classification of events into *network events* and *rearrangements*. As discussed in § 3.3, we expect that the particle positions, energy and shear stress are continuous for a network event, while they will be discontinuous for a rearrangement.

For each event, we have determined the particle positions $\vec{r}^{\,-}$ and $\vec{r}^{\,+}$, the energies U^- and U^+ and the shear stresses σ_{xy}^- and σ_{xy}^+ before and after the event. With these, we define the mean squared distance

$$R^2 = \left\langle |\vec{r_i^+} - \vec{r_i^-}|^2 \right\rangle \ , \tag{3.5}$$

where the average is taken over all particles, the relative energy change

$$\widetilde{\Delta U} = (U_i^+ - U_i^-)/U_i^- \ , \tag{3.6}$$

and the relative shear stress change

$$\widetilde{\Delta\sigma} = (\sigma_{xy,i}^+ - \sigma_{xy,i}^-)/\sigma_{xy,i}^- \ . \tag{3.7}$$

With these, we can calculate a 3D histogram $(R^2, -\widetilde{\Delta U}, |\widetilde{\Delta\sigma}|)$, where we only includes events with a *drop* in energy — as we will discuss later, rearrangements cannot increase the energy of the system. We plot 2D projections of this histogram in Fig. 3.4 for $N = 512$ ensembles at $P = 10^{-6}$ and $P = 10^{-2}$. For $P = 10^{-2}$, we observe a clear separation into two clusters: one at high R^2, $-\widetilde{\Delta U}$ and $|\widetilde{\Delta\sigma}|$, consisting of rearrangements, and one cluster at low R^2, $-\widetilde{\Delta U}$ and $|\widetilde{\Delta\sigma}|$, corresponding to network events. This cluster appears at small, but finite, values of R^2, $-\widetilde{\Delta U}$ and $|\widetilde{\Delta\sigma}|$, due to the small, but finite, strain step $\Delta\gamma = \gamma^+ - \gamma^-$. This step is defined by the bisection algorithm, which continues until $\Delta\gamma/\gamma^- < 10^{-6}$. We have repeated simulations with a higher tolerance, i.e., stopping the bisection at $\Delta\gamma/\gamma^- < 10^{-5}$, and found the values of R^2, $-\widetilde{\Delta U}$ and $|\widetilde{\Delta\sigma}|$ for network

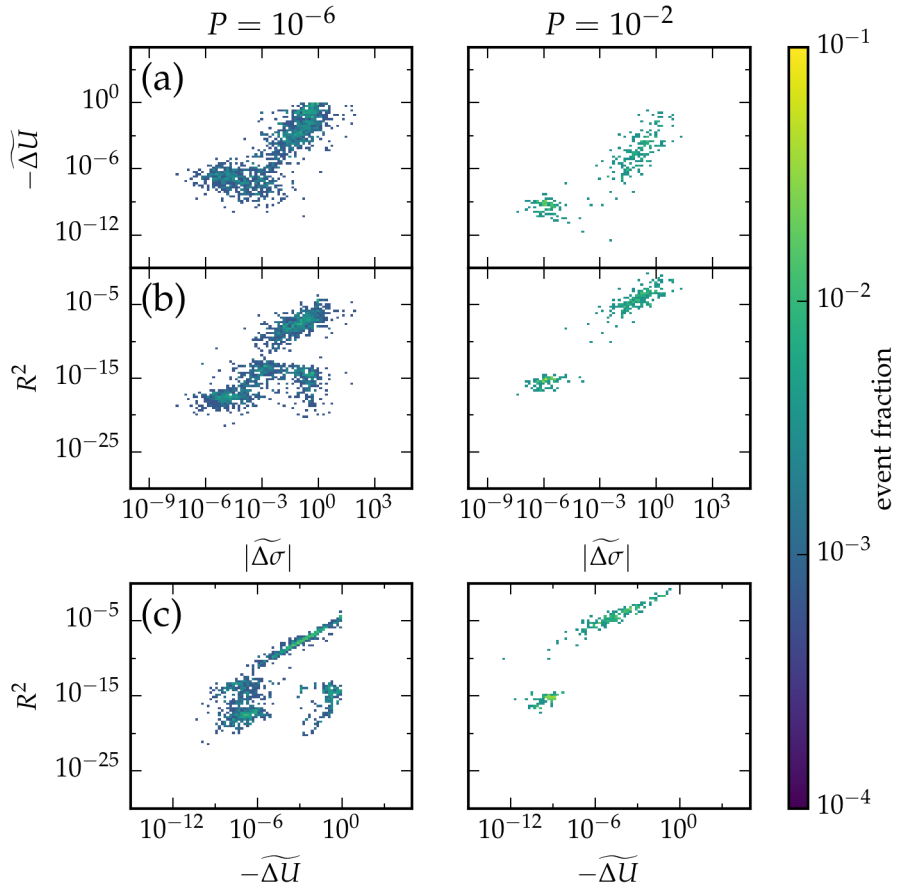

FIGURE 3.4: 2D projections of a 3D histogram of the particle displacements R^2, relative energy drop $\widetilde{\Delta U}$ and relative stress change $\widetilde{\Delta\sigma}$ for $P = 10^{-6}$ (5000 events) and $P = 10^{-2}$ (2500 events). We sort events into 100 log-spaced bins on each axis: R^2 from 10^{-30} to 10^{0}, $\widetilde{\Delta U}$ from 10^{-15} to 10^{5} and $\widetilde{\Delta\sigma}$ from 10^{-10} to 10^{5}. The colorbar represents the fraction of events in each bin; white indicates bins without events. For $P = 10^{-2}$, the data shows a clear separation, with R^2 and $\widetilde{\Delta\sigma}$ providing the cleanest distinction. For $P = 10^{-6}$, the separation is less clear: there is now a much wider spread in R^2 and $\widetilde{\Delta\sigma}$, and $\widetilde{\Delta U}$ now seems to provide the clearest separation.

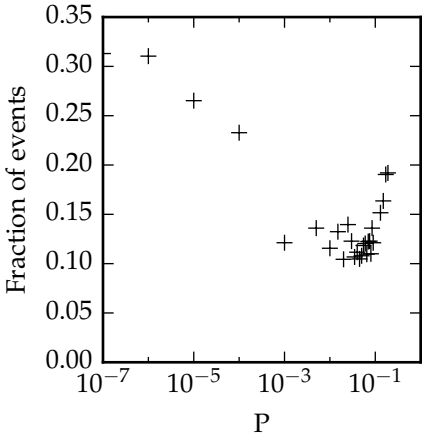

FIGURE 3.5: Fraction of events with $U^+ \leq U^-$.

events depend strongly on this tolerance, while events in the rearrangement cluster are unaffected.

For $P = 10^{-6}$, the situation is not as clear — the two clusters are spread out, and a new cluster at low R^2 but large $-\widetilde{\Delta U}$ and $|\widetilde{\Delta\sigma}|$ has formed. These events are likely to be rearrangements with abnormally small displacements.

Although the separation between network events and rearrangements in Fig. 3.4 is not entirely clear for low pressures, we can still find an upper bound for the fraction of events that are rearrangements. As noted before, rearrangements involve a discontinuous jump in the energy U and the stress σ. In the case of a rearrangement, the jump in energy must be to a *lower* value. Network events can show both an increase and a decrease in energy, depending on the sign of σ. Because events with $U^+ > U^-$ cannot be rearrangements, we can take the fraction of events with $U^+ \leq U^-$ as an upper bound to the fraction of rearrangements. In Fig. 3.5, we show this fraction as a function of P. We observe the bound starts out at 30% for $P = 10^{-7}$, decreases to 10% for $P = 10^{-1}$ and increases again to 30% at $P = 2 \times 10^{-1}$. We cannot be certain whether this trend is due to a changing prevalence of rearrangements, or due to network events being more or less likely to have a negative energy change. Nonetheless, we can be certain

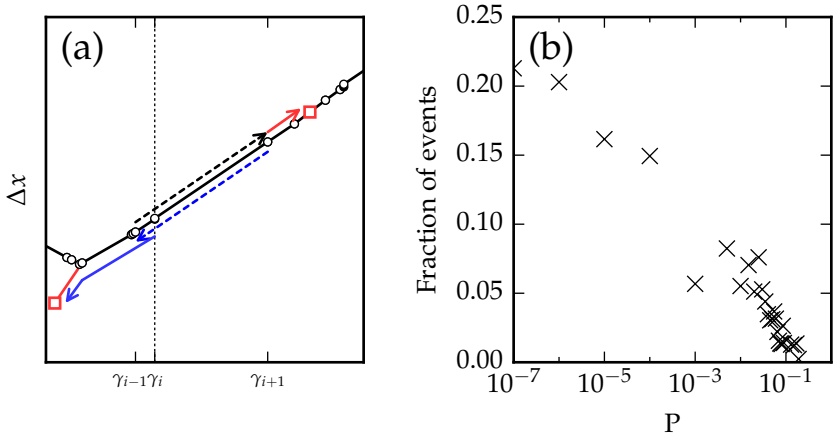

FIGURE 3.6: (a) A single particle coordinate as function of strain during the strain cycle and during stress relaxation. During the strain cycle (black and blue dashed arrows), the system is fully reversible. The stress relaxation *before* the event (blue solid arrow) relaxes to a lower strain, but after the event, $\sigma < 0$, and the system relaxes to a stable position at a *higher* strain (red solid arrow). The system is therefore irreversible. (b) The fraction of events with $\sigma^-_{i+1} < 0$

that at most 30% of events are rearrangements, and network events occur more regularly.

We have seen that we can clearly distinguish network events from rearrangements for systems at high pressure. At low pressure, the distinction is blurred. Whether this is due to our choice of parameters remains to be seen, and is a topic for future work. Nevertheless, we are able to give an upper bound for the fraction of rearrangements, and find at most 30% of events are rearrangements.

3.5.2 Reversibility

We now focus on the connection between the event type and reversibility under stress and strain. We expect several distinct classes of behavior, and will show preliminary data on the prevalence of the different types of events.

We first focus on network events. In general, we expect these to be reversible: When particle motions are continuous, as is the case for network

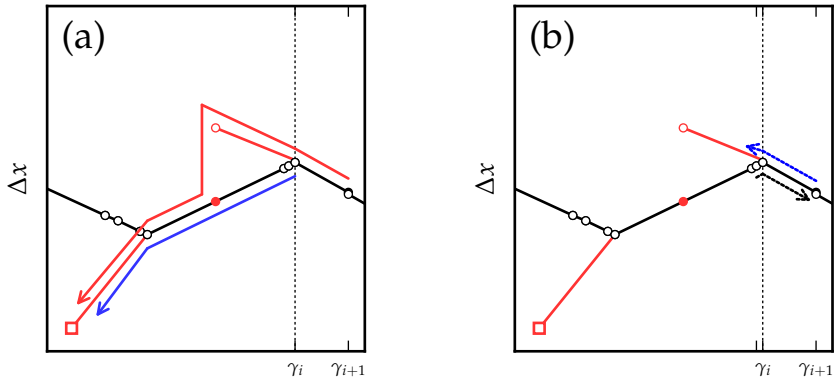

FIGURE 3.7: A single particle coordinate as function of strain during (a) stress relaxation (red and blue arrows) and (b) during the strain cycle (black and blue arrows). In the stress cycle, the system is loop reversible: from γ^+ downward, a different branch is followed, but both branches merge at some strain $\gamma < \gamma^+_{i-1}$. During the strain cycle, the system also follows the second branch on the way back, but never shears back far enough to jump back to the original branch. We detect the system as irreversible under strain cycling.

events, there is no clear path for them to become irreversible. There are two exceptions to this rule. First, when we create a rattler at γ_i, the path of that rattler from γ_i to γ^-_{i+1} is ill-defined, and so is its path back to γ^+_i. It is unlikely for the rattler to become part of the contact network at exactly the same strain. Nonetheless, the particle is locally confined, and we thus expect the particle to rejoin the network somewhere near γ_i, which would make the system loop reversible. Second, we can expect event i to be stress irreversible without rearrangements if $\sigma^-_{i+1} < 0$ while $\sigma^-_i > 0$. In that case, the system will relax to a lower strain when starting from γ^-_i, but will relax to a *higher* strain when starting from γ^-_{i+1}, as sketched in Fig. 3.6(a). We can again determine an upper bound for this type of event — we can determine the fraction of events with $\sigma^-_{i+1} < 0$, but we do not know how these events would be classified under strain reversal. In Fig. 3.6(b), we show the fraction of events with $\sigma^-_{i+1} < 0$, and observe a strong decrease with pressure. While for low P, almost one in four events has a negative post-event stress, the prevalence decreases to almost zero at $P = 10^{-2}$.

We now turn to the reversibility of rearrangements. Here, we can see either loop reversible or irreversible events, and we have no a priori expectation for the prevalence of either. Instead, we will focus on the expected correlations between strain and stress reversibility.

First, we expect no line reversible events: discontinuities normally are associated with hysteresis — the instability of the system at γ_i^- that leads to a jump towards a new state at γ_i^+ should not cause the state at γ_i^+ to be similarly unstable under backwards shear. We thus expect all rearrangements to be either loop reversible or irreversible.

Second, we expect systems that are loop reversible under strain to be similarly loop reversible under stress. If the system jumps back to the original branch between γ_i and γ_{i-1} in strain control, we expect the stress relaxation to follow the same path. The exceptions to this are, as discussed before, events with $\sigma_{i+1}^- < 0$. In contrast, events that are (loop) reversible under stress relaxation are not necessarily loop reversible under stress relaxation. In Fig. 3.7, we sketch an example where the event is loop reversible under stress but irreversible under strain, because the system jumps back to the original branch only for $\gamma < \gamma_{i-1}^+$.

Finally, the system can be irreversible under stress relaxation. In that case, we expect the strain cycle to follow the same irreversible path, and we would classify the event also as irreversible under strain.

We have sketched the expected reversibility behavior for network events and rearrangements, and summarize the behavior in Table 3.2. In general, we expect network events to be line reversible, with two exceptions. We expect to observe the discontinuities of rearrangements in loop reversible or line reversible behavior.

	event type	strain cycle	stress relaxation
typical behavior			
	network	line reversible	reversible
	rearrangement	loop reversible	reversible
	rearrangement	irreversible	irreversible
network events involving rattlers			
	network	loop reversible	reversible
	network	irreversible	irreversible
Fig. 3.6(a) ($\sigma_{i+1}^{-} < 0$)			
	network	line reversible	irreversible
	rearrangement	loop reversible	irreversible
Fig. 3.7			
	rearrangement	irreversible	reversible

TABLE 3.2: Possible combinations of event type and reversibility in the strain cycle and under stress relaxation, as discussed in § 3.5.

3.6 Conclusion and outlook

We have shown that in granular systems, rearrangements that alter the total energy or shear stress in a system, denoted rearrangements, are rarer than network events that alter the contact network but leave the energy unchanged. We propose a connection between the type of event and their behavior under stress relaxation and strain reversal. We have discussed that we expect stress and strain reversal to disagree in a significant minority of events ($< 25\%$), in situations where $\sigma_{i+1}^{-} < 0$.

We propose several directions for future research. First, and foremost, we will implement and analyze the stress relaxation and strain cycle protocols. In parallel, we will investigate whether it is possible to make a clean distinction between network events and rearrangements at low pressures, and if not, which ranges of pressure allow for a clean distinction. Once these pieces are in place, we will be able to numerically verify the proposed correlations between event type and the reversibility properties. In addition, we

will be able to show trends with P in the various measures, where we expect to see a transition between behavior close to the jamming transition and behavior at high densities, as it is known that the nature of rearrangements change with pressure – close to jamming, particles have strong nonaffine motion, and one expects rearrangements to be extended and fragile [31, 52], while at high pressure, rearrangements become localized, as described in Shear Transformation Zone theories [4, 111].

The nature of rearrangements has strong experimental relevance. The prevalence and stress reversibility of events and, to a lesser extent, the discontinuities of rearrangements are measurable in experiments. As such, any pressure dependence is likely to have implications for oscillatory strain protocols, and whether memory formation and readout are more effective at different pressures.

So far, we have restricted ourselves to studying particle packings that are not strained very far (less than 5%) from a zero-stress state. Therefore, we are unlikely to see large avalanches associated with self-organized states that occur when the average shear stress is comparable to the average pressure. It will be interesting to study how reversibility is affected by the average shear stress in addition to the pressure.

CHAPTER 4

SHEARED FOAMS

A paper based on the work presented in this chapter is in preparation as:

[122] Merlijn S. van Deen, Alexander O.M. Siemens and Martin van Hecke *Rearrangements in Wet and Dry Foams*.

In this chapter, we investigate the behavior of a jammed two-dimensional foam under shear. We focus on the behavior under slow steady shear, as this allows us to come as close as possible to the quasi-static limit studied in numerical simulations in the previous chapters. We will first show qualitative changes by comparing foams at low ($\phi = 0.85$) and very high ($\phi = 1.5$) densities. While at high densities abrupt rearrangements dominate, nonaffine motion dominates the behavior at low densities. We will show that this change in behavior can be quantified by various measures: we will determine the structural relaxation time and the autocorrelation time, quantify the amount of nonaffine motion and finally quantify the degree of localization. A coherent picture emerges, where discrete, localized events at high density give way to qualitatively different, much more smooth and homogeneous behavior near jamming.

4.1 Introduction

The focus of this work is on the response of foams in slow steady shear over a range of packing density ϕ. Earlier work on foams has mostly focused on the behavior in the high density limit [123–127], on the rheology [39, 40, 58], or on static properties [26, 51]. The phenomenology in this limit is similar to other experimental work on plastic behavior in colloids, where the system behaves like a densely packed foam. This behavior is typically described in terms of shear transformation zones and avalanches [111, 121, 128], although the interest in nonaffine behavior is growing [129, 130]. The issue is that at lower densities, closer to jamming, the phenomenology appears to

change qualitatively. By controlling the packing density over a wide range while slowly shearing the system, we uncover unambiguous trends in the behavior of the system.

The outline of this chapter is as follows. First, we will introduce our setup, measurement protocols and post processing steps in §§ 4.2 and 4.3. We will then discuss our results in § 4.4: we will discuss the viscous and structural relaxation timescales in §§ 4.4.1 and 4.4.2, non-affine behavior in § 4.4.3 and finally discuss two characteristics of rearrangements, spatial localization and caged motion, in § 4.4.4. We will finish with the discussion and conclusion in § 4.5.

4.2 Setup and protocol

In this section, we will discuss our measurement set up, as well as the driving protocols. We perform measurements on a bidisperse quasi-2D monolayer of foam bubbles, as shown in Fig. 4.1. These bubbles are trapped under a glass plate, to stabilize the bubbles and to remove the effect of surface tension, which leads to bubble-bubble attraction [26, 40, 59], also known as the 'Cheerios effect' [132]. From the sides, the system is confined between four walls. This serves two purposes. First, where earlier work tuned the packing density using a gap between the glass plate and the liquid [26, 133], we can directly and precisely compress the foam over a wide range of densities by moving one or both walls inward. Second, we can apply a pure shear deformation by moving one wall inward and the other outward. We measure the response of the foam by imaging the system from above using a digital camera. We will discuss each part of the setup in the following subsections. We will first discuss the surfactant solution and the creation of foam bubbles. We will then turn to the mechanical setup used to drive the walls, and finally turn to the question of the measurement protocol.

4.2.1 Surfactant and foam

We create the two-dimensional packing by blowing nitrogen bubbles in a surfactant solution. In this subsection, we will describe the surfactant solution used and the procedure for creating bubbles.

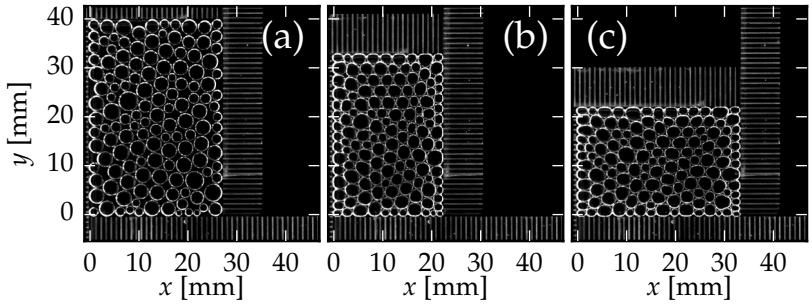

FIGURE 4.1: Foam at different densities (see § 4.2.4) and deformation (see § 4.2.5). (a) Foam at $\phi = 0.85$, $s_{CD} = -0.2$. (b) Foam at $\phi = 1.25$, $s_{CD} = -0.2$. (c) Foam at $\phi = 1.25$ after pure shear deformation, $s_{CD} = +0.2$. The frames are cropped to 800×800 px, corresponding to 50.4 mm $\times$ 50.4 mm. Video versions of these figures are available on-line [131, S1 and S2].

As surfactant solution, we use the basic foam mix from Golemanov et al. [134]. The solution is prepared in two steps. First, we create a stock surfactant solution by mixing 59.4 g (6.6 wt%) sodium lauryl ether sulfate (SLES), 30.6 g (3.4 wt%) cocamidopropyl betaine (CAPB) with 810 g (90 wt%) demineralized water. This is stirred mechanically until the SLES has completely dissolved. In the second step, we first prepare a viscous mix of water and glycerol. The high viscosity helps to stabilize the foam, as the diffusion coefficient of gas through the foam boundaries, i.e., from bubble to bubble, is inversely proportional to viscosity [135]. We use 2640 g (43.7 wt%) glycerol and 3130 g (51.8 wt%) demineralized water. After the glycerol has been completely dissolved, we add 275 g (4.5 wt%) of the stock surfactant solution and use a stir plate to gently mix the solution. The final solution contains 0.30 wt% SLES and 0.16 wt% CAPB. Density, viscosity and surface tension were measured by Siemens [59], and are $\rho = (1094 \pm 2)\,\mathrm{kg/m^3}$, $\eta = (3.87 \pm 0.01)\,\mathrm{mPa\,s}$ and $\sigma = (25.6 \pm 0.3)\,\mathrm{mN/m}$, respectively. During measurements, approximately 100 mL of water evaporates per day, corresponding to a fluid level decrease of 1 mm. To compensate for this loss, we top up the container with demineralized water daily. We do not observe any changes in behavior due to this refilling procedure.

To create the foam, we bubble nitrogen through the surfactant using a needle, held at the bottom of the surfactant solution, at a depth $D = 50$ mm. The gas flow is limited by a combination of a pressure control valve and a

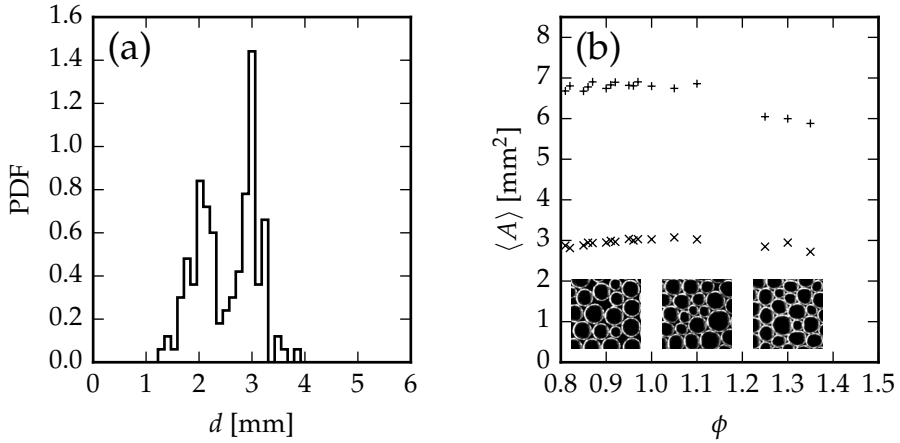

FIGURE 4.2: (a) PDF of bubble radii for an uncompressed system. Our systems are largely bidisperse, with a 50 : 50 mixture of $d \approx 2\,\mathrm{mm}$ and 3 mm. (b) Mean bubble area as a function of density ϕ for small (crosses) and large bubbles (pluses). The small bubble area is largely independent of ϕ, but the large bubbles are more easily deformed, and decrease in area for $\phi > 1.2$. Snapshots show sections of the foam at $\phi = 0.9$, 1.1 and 1.3.

flow control valve. The pressure control valve limits the overpressure to 1 bar, while the flow control valve limits the flow to $Q = 0.55\,\mathrm{mL/s}$ at a pressure difference of 1 bar. To prevent crystallization, the foam has to have a sufficiently large variety in bubble sizes [39, 136, 137]. We therefore use a 50 : 50 mixture with an ≈ 1.4 size ratio, as is common in simulations [3, 13, 137]. We create bubbles using two different needles. Large bubbles are created using a 21G needle, resulting in bubbles with $d = (3.0 \pm 0.2)\,\mathrm{mm}$. Small bubbles are created using a 30G needle, resulting in bubbles with $d = (2.1 \pm 0.3)\,\mathrm{mm}$. We create approximately 250 bubbles — twice the required amount of bubbles. By hand, we remove bubbles to reach the desired 50 : 50 bubble ratio and to remove any crystalline patches. In this way, we end up with a packing of 120–130 bubbles, with an unjammed size of 380–435 mm^2. We show the final probability density function of the bubble radii for an example system in Fig. 4.2(a).

We have measured the stability of the foam during a set of shear experiments with a total runtime of 75 hours. In this period, we measured only 3 coalescence events, i.e., events where two bubbles merge, reducing the

number of bubbles from 136 to 133. Coarsening, where the large bubbles drain nitrogen from the small bubbles, is not noticeable over this period of time; the change in both the mean and the standard deviation of the distribution is much smaller than the measurement error. We note that for high densities $\phi \gtrapprox 1.2$ (see § 4.2.4 for definition) the large bubbles deform noticeably, with their area reducing by 10–15%, while the effect on the small bubbles is negligible (Fig. 4.2(b)). In addition, we are limited to $\phi \lessapprox 1.5$, above which bubbles buckle out of plane and form a second layer.

4.2.2 Mechanical setup

We trap the bubbles between a glass plate on the top and four boundaries on the sides (Fig. 4.3). The glass plate serves two purposes. First, the plate removes the attraction between the bubbles due to surface tension. Second, the plate reduces coarsening and coalescence by keeping the Plateau borders hydrated [138]. The surface of the liquid is always higher than the glass plate, typically by 3–5 mm. Using a set of micrometer screws, we carefully level the glass plate, with a maximum deviation from level of 10^{-5} rad, to reduce the effect of gravity on the packing [59].

The boundaries on the sides are used to confine, compress and shear the system. Each of the boundaries is driven by a linear translation stage (Bahr Modultechnik `EL30`) connected to a stepper motor (Lin Engineering `4118L-01-R0`). Each stepper motor is powered by a driver (Advanced Micro Systems `CDR-4MPS`), which is controlled by a computer using a TTL pulse input. To determine the proportionality constant, we measured the distance between the walls using a caliper for various pulse counts, and found that

$$C_{\mathrm{st}} = 4.95 \times 10^{-5}\,\mathrm{mm/pulse}. \tag{4.1}$$

From LabVIEW, these stepper motors are driven using two *pulse train* (square wave at a given frequency) outputs for the velocity and two digital direction outputs for the direction. We use one output pair to drive the b motor, which moves the B and C boundaries in the y direction, and a second pair to drive the c and d motors in unison. These motors move the C and D boundaries in the x direction (Fig. 4.3(c)).

The frequency of the pulse train output can only be updated at a limited rate. This causes the actual deformation to 'lag behind' the deformation we want to apply — the wall moves too fast if the frequency decreases, or too

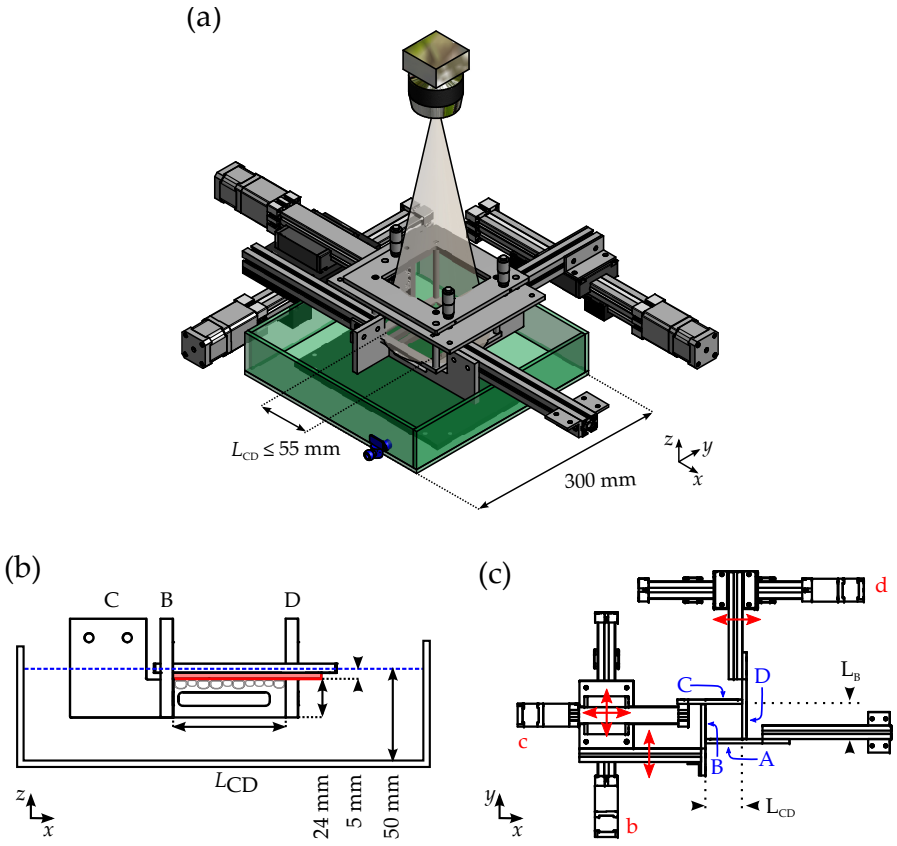

FIGURE 4.3: The bi-axial measurement setup. (a) Overview. Bubbles are created in a surfactant solution and trapped between a glass plate on top and four boundaries on the sides. Three of the four boundaries are driven by linear stages. The glass plate can be leveled using three micrometer screws. The system is imaged from the top using a CMOS camera. (b) Side view, where boundary A has been removed for clarity. Boundaries B, C and D are indicated. Bubbles are trapped under a glass plate (red), and the water level (blue) is 5 mm above the glass plate. (c) Top view, with the top plate removed. The four boundaries and their motion are indicated; boundary A is fixed, while boundary B moves in the y direction, D in the x direction, and C in both directions (red arrows). Their driving stages are marked as a, b and c; boundary C is displaced by stages b and c; stages c and d follow the same displacement. Confinement lengths L_B and L_{CD} are indicated.

slow if the frequency increases. To remedy this, we implement a simple feedback in our system. We measure the number of sent pulses using a second I/O card, and, using the measured deviation, apply proportional feedback. Including a feedback term, the frequency of the square wave we send to the stepper motor driver is given by

$$f = \left| C_{\mathrm{st}}^{-1} \frac{\partial l}{\partial t} - q(p_{\mathrm{sent}} - p_{\mathrm{expected}}) \right|, \tag{4.2}$$

where p_{sent} and p_{expected} are the measured and calculated pulse counts, respectively. We find $q = 1/\mathrm{s}$ gives effective feedback, keeping $|p_{\mathrm{sent}} - p_{\mathrm{expected}}| \lesssim 2\,\mathrm{pulses} \approxeq 0.1\,\mu\mathrm{m}$.

We use a set of four inductive position sensors to detect the end of the movement range on both axes; two on each axis. These serve a dual purpose. First, we use them to define the zero point for the position counters. We define $n_B = 0$, $n_{CD} = 0$ to be at the outermost sensors, which corresponds to a maximum physical box size

$$l_B(0) = 45.3\,\mathrm{mm} \times l_{CD}(0) = 56.6\,\mathrm{mm}, \tag{4.3}$$

which corresponds to a length of 916 000 and 1 144 000 pulses, respectively. We move each side wall outwards until the inductive sensor is triggered. We then move inwards at a slower rate, until the sensor is no longer triggered. We reset the pulse count at this point. We repeat this protocol with ever decreasing rates. We always reset the pulse count on the inward direction, as the inductive sensors are somewhat hysteretic. This protocol allows us to recover the zero position with an error of $\sim 10\,\mathrm{pulses} \approxeq 0.5\,\mu\mathrm{m}$. We run this calibration at the start of each measurement session.

Second, we use the sensors to end the measurement when we reach one of them, indicating that the end of the measurement range has been reached. In addition to this software-based approach, we also have a set of break switches, which disable the stepper motors on a hardware level. This prevents hardware damage due to software errors.

4.2.3 Imaging

To measure the response of the system, we image the system from the top using a Basler A622f CMOS camera (8 bits grayscale, 1280×1024 pixel, $6.7\,\mu\mathrm{m} \times 6.7\,\mu\mathrm{m}$ pixel size [139]) with a Tamron $28 - 300$ mm macro lens at

$f \approx 38\,\mathrm{mm}$. The distance from sensor to the glass plate is 455 mm, resulting in an overall image scale of $C_{\mathrm{im}} = 60\,\mu\mathrm{m/px}$.

To clearly image the foam bubbles, we mount 30 cm long LED strips around each side of the setup (off-brand '3528' SMD LEDs, 240/m, with an input power of 1.8 W per strip). The light from these LED strips is reflected by the Plateau borders of the bubbles, and causes the bubbles to show up as white circles [26, 59]. We have determined camera gain (ca. 350 photons per bit, register value 112) and shutter time (11.24 ms, register value 562) to correspond to saturated bubbles at the given lighting conditions (Fig. 4.1). We typically image at $f_{\mathrm{im}} = 1\,\mathrm{Hz}$ or 10 Hz, and store all images for post-processing.

4.2.4 Packing density

We define the packing density in terms of an area fraction, where we divide the undeformed foam area by the current system area. This is analogous to what is commonly done in simulations on jamming [3, 13, 22].

To determine the undeformed foam area, we measure the transition from the *boundary jammed* to the *gravity jammed* regime [59], the closest analog to the jamming transition in this system. We will call the confinement box size at which this happens the *jamming area* A_j. To determine A_j, we use two different protocols. While setting up the experiment, we slowly move one boundary outwards until a hole forms, and denote the area at which the hole first appears as A_j. This protocol works best in the initial setup, where we can manually move the walls to accurately find the correct area. To measure A_j after each measurement, we expand the system until a significant hole has formed, and measure the hole size A_h in ImageJ. We then find $A_j = A - A_h$, where A is the confinement box size [59]. We find A_j is essentially constant ($< 1\%$ change) over 72 hours. We will therefore take A_j as constant, and all values of ϕ reported will be calculated with respect to A_j measured while setting up the measurement.

Given A_j, we calculate the foam area by assuming the packing fraction at this confinement is $\phi_j \approx 0.842$, as reported in jamming simulation literature [13]:

$$A_{\mathrm{foam}} = \phi_j A_j = 0.842 A_j \,. \tag{4.4}$$

For a given confinement box size A, we can now determine ϕ using

$$\phi = \frac{A_{\mathrm{foam}}}{A} \,, \tag{4.5}$$

where we use the *undeformed* foam area A_{foam}. We note that ϕ can become larger than 1 due to the deformation of foam bubbles. Inversely, we can determine the system area for a given ϕ as

$$A = \frac{A_{\text{foam}}}{\phi} = \frac{\phi_j}{\phi} A_j \,, \tag{4.6}$$

which we use to set the density in the driving protocol.

4.2.5 Deformation

We deform our system by driving the side walls of our system. In this section, we will discuss how we independently drive the walls to compress and shear the system. For our measurements, the most relevant deformation is continuous pure shear, and we will choose our notation to reflect that.

We note that there are multiple valid ways to define shear strain in a system. As we expect the response of our system to be best described by a series of small strain increments, we choose to work with the logarithmic or Hencky strain [140]

$$\varepsilon = \int_L^l \frac{1}{l'} dl' = \ln(l/L) \,, \tag{4.7}$$

where $l(t)$ is the deformed length and L the undeformed length. In Hencky strain, a constant strain rate corresponds to an exponential movement of the boundaries, and it is therefore useful to write the lengths of the boundaries in terms of an area A_0 and a length factor $e^{s_j(t)}$:

$$\begin{aligned} l_B &= \sqrt{A_0} \cdot e^{s_B(t)} \,, \\ l_{CD} &= \sqrt{A_0} \cdot e^{s_{CD}(t)} \,. \end{aligned} \tag{4.8}$$

At the beginning of each measurement, $A = A_0$, and $s_B(0) = -s_{CD}(0)$. In our experiments, we then apply a deformation of the form

$$\begin{aligned} s_B(t) &= -s_{CD}(0) - \frac{1}{2}\gamma(t) + \varepsilon_{BB}(t) \,, \\ s_{CD}(t) &= +s_{CD}(0) + \frac{1}{2}\gamma(t) \,, \end{aligned} \tag{4.9}$$

a combination of pure shear strain and uniaxial compressional strain, and typically start at $s_{CD}(0) = -0.2$ (Fig. 4.4(a)). We use the following protocols: (i) continuous pure shear $\gamma(t) = \dot{\gamma}t$, (ii) sinusoidal pure shear $\gamma(t) = \gamma_{\max}\sin(\omega t)$, (iii) step pure shear $\gamma(t) = \gamma_s H(t)$, where $H(t)$ is the Heaviside step function, and (iv) continuous uniaxial compression $\varepsilon_{BB} = \dot{\varepsilon}_{BB}t$.

We can derive the effective shear and compression rate from the wall velocities

$$\frac{\partial}{\partial t}l_B = l_B\frac{\partial s_B}{\partial t}\ ; \quad \frac{\partial}{\partial t}l_{CD} = l_{CD}\frac{\partial s_{CD}}{\partial t}\ , \tag{4.10}$$

and find

$$\begin{aligned}\dot{\gamma}(t) &= \frac{\partial l_{CD}/\partial t}{l_{CD}} - \frac{\partial l_B/\partial t}{l_B} = \frac{\partial s_{CD}}{\partial t}(t) - \frac{\partial s_B}{\partial t}(t)\ , \\ &= \frac{\partial}{\partial t}\left[\gamma(t) - \varepsilon_{BB}(t)\right]\ . \end{aligned}\tag{4.11}$$

The compression rate is

$$\begin{aligned}\dot{\varepsilon}(t) &= \frac{1}{A}\frac{\partial A}{\partial t} = \frac{\partial l_B/\partial t}{l_B} + \frac{\partial l_{CD}/\partial t}{l_{CD}} = \frac{\partial s_{CD}}{\partial t}(t) + \frac{\partial s_B}{\partial t}(t) \\ &= \frac{\partial}{\partial t}\varepsilon_{BB}(t)\ , \end{aligned}\tag{4.12}$$

where positive $\dot{\varepsilon}$ corresponds to expansion.

In Fig. 4.4, we sketch the general protocol of a single measurement. First, we expand the system to the jamming transition at $A = A_j$. After relaxing the system, we compress it to a given density ϕ, and again relax the system. We then run the measurement; in the case of a shear deformation, we set $\dot{\varepsilon} = 0$, $\dot{\gamma} = \dot{\gamma}$, and start at $s_{CD}(0) = -0.2$. We deform until $s_{CD}(t) = 0.2$, for a total shear strain $\Delta\gamma = 0.4$. Finally, we slowly expand the foam to re-measure the jamming area, which allows us to detect foam coalescence and coarsening. A full measurement run consists of 10 to 20 of these individual measurements, each for a different value of ϕ.

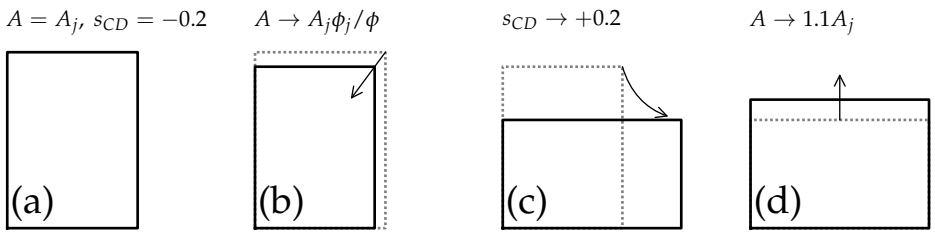

FIGURE 4.4: The bi-axial shear protocol. (a) Initially, we move the system to $A = A_j$ at $s_{CD} = -0.2$. We relax the system for 20 min. (b) Next, we compress the system to the target density ϕ by decreasing the area to $A = A_j\phi_j/\phi$, and let the system relax for 10 min. (c) We then shear the system at a fixed $\dot{\gamma}$ from $s = -0.2$ to $s = 0.2$. (d) Finally, we measure the current foam size by moving a single wall outwards, until we reach $A = 1.1A_j$. We use this information afterwards to calibrate our densities.

4.3 Post processing

In the following two sections, we will describe in detail the post-processing steps we apply to the recorded images. In this section, we will first focus on *difference imaging* and the *image variance* $\langle \Delta I^2 \rangle(t, \Delta t)$, including correcting for the affine deformation field. Second, we will introduce our particle tracking algorithm and will discuss the tracking quality and affine correction.

4.3.1 Difference imaging

We will first describe how we measure the activity in the system using difference imaging. In Fig. 4.5(a,b), we show a $\phi = 1.25$ foam under pure shear at (a) $t = 5000$ s and (b) $t = 5010$ s, which we will use to explain the process.

We describe each image as a set of intensities $I(x, y, t)$, where $0 \leq I < 1$ (Fig. 4.5(a,b)). We can then calculate the difference image

$$\Delta I(x, y, t, \Delta t) = I(x, y, t + \Delta t) - I(x, y, t) \,, \tag{4.13}$$

which is shown in Fig. 4.5(c). The difference image highlights the motion between (a) and (b). Each moving particle shows up as a set of crescents, indicating the old and new positions of the edges. The crescents corresponding to the old positions have negative ΔI (red), while the crescents corresponding to the new positions have positive ΔI (blue). We observe

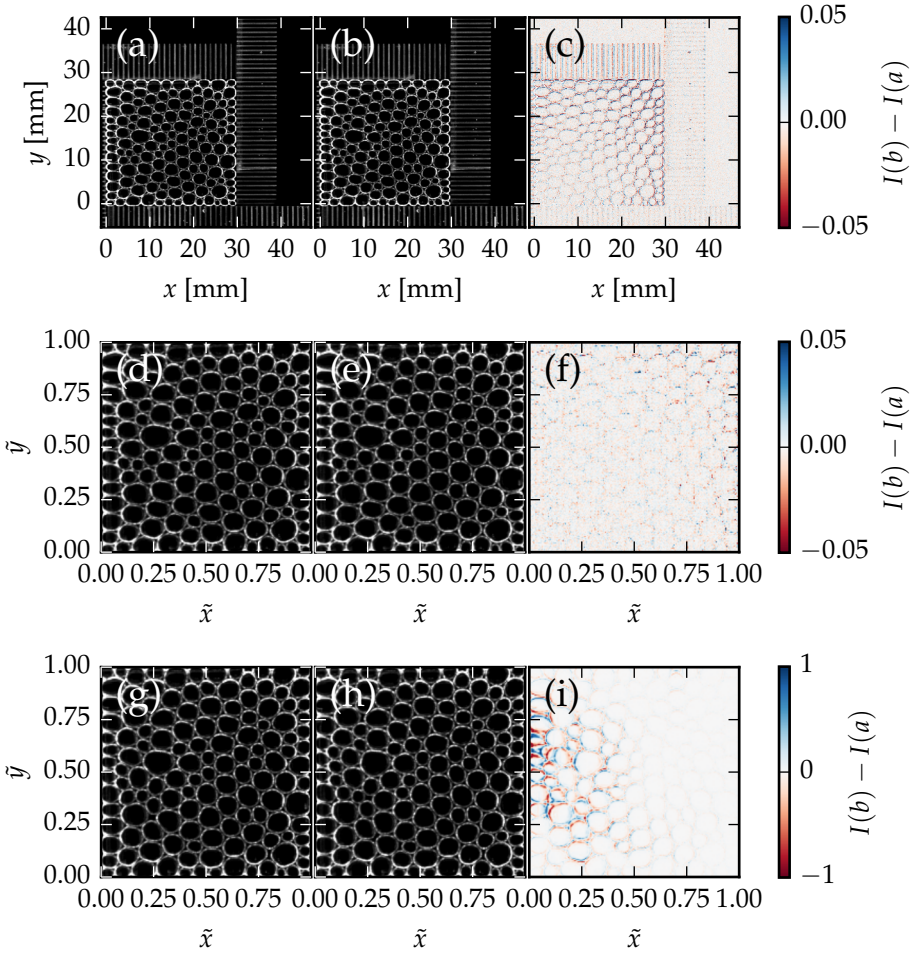

FIGURE 4.5: $\phi = 1.25$ foam under pure shear $\dot{\gamma} = 3 \times 10^{-5}$/s. (a) $t = 5000$ s. (b) $t = 5010$ s. (c) The difference image is dominated by the affine deformation field; $\langle \Delta I^2 \rangle = 2.6 \times 10^{-4}$. (d,e) Affine-corrected version of (a) and (b). We apply the correction by cropping the image to the foam, and resizing the image to a square 200×200 px image. (c) The difference image is almost homogeneous now, showing just the non-affine parts of the deformation field; $\langle \Delta I^2 \rangle = 5.4 \times 10^{-5}$. (g,h) Rearrangement between (g) $t = 5890$ s and (h) $t = 5900$ s. (i) Affine-corrected difference image; $\langle \Delta I^2 \rangle = 1.2 \times 10^{-2}$. Video versions of these figures are available on-line [131, S3 and S4].

that the difference image is dominated by the affine deformation: the top wall moves towards the bottom, while the right wall moves towards the right. The foam largely follows this deformation.

From the difference image, we then quantify the behavior by calculating the mean of squared pixel differences, i.e., the *image variance*

$$\langle \Delta I^2 \rangle (t, \Delta t) = \left\langle (\Delta I(x, y, t, \Delta t))^2 \right\rangle , \tag{4.14}$$

where the average is taken over the foam area. A high $\langle \Delta I^2 \rangle$ corresponds to a large amount of motion in the system. If there is no motion in the system, we are limited by pixel noise, and find $\langle \Delta I^2 \rangle \approx 2 \times 10^{-5}$. At the high end, we observe saturation of the signal for $\langle \Delta I^2 \rangle \approx 4 \times 10^{-2}$.

We find $\langle \Delta I^2 \rangle$ is dominated by the affine deformation field, as shown in Fig. 4.5(c), where we find $\langle \Delta I^2 \rangle = 2.6 \times 10^{-4}$. We are, however, mostly interested in the *nonaffine* behavior, as we expect the nonaffine behavior to differ between low and high ϕ. We therefore apply an affine correction by resizing each frame to a fixed size of 200×200 pixels using cubic spline interpolation, as shown in Fig. 4.5(d,e). This almost completely removes the affine deformation field, as shown in Fig. 4.5(f), and we find an affine-corrected $\langle \Delta I^2 \rangle = 5.4 \times 10^{-5}$.

Finally, we show an example of a rearrangement in Fig. 4.5(g-i). In this rearrangement, a bubble moves inwards from the edge, and the foam around it moves to accommodate this rearrangement. For this rearrangement, we find $\langle \Delta I^2 \rangle = 1.2 \times 10^{-2}$, close to the saturation level. This is not surprising — almost half of the system participates in the rearrangement.

4.3.2 Particle tracking

To supplement our difference imaging, we implemented an iterative particle tracking algorithm, where the particle detection in each step is supported by position information from the previous time step. In this section, we will introduce our tracking method.

Regular particle tracking algorithms have difficulty tracking bubbles for various reasons. First, a particle tracking algorithm cannot easily distinguish bubbles and the empty areas between bubbles — an issue that is especially problematic for foams close to jamming. Second, in our setup, bubbles are not lighted homogeneously, which makes thresholding difficult.

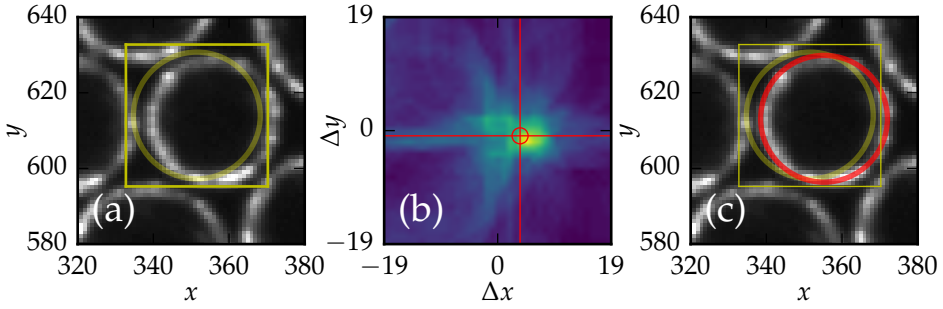

FIGURE 4.6: Hough-based particle tracking. (a) Frame $t = i + 1$ with the old position at $t = i$ overlaid (yellow circle). We crop the new frame around the original particle, with an extra 2 px border (yellow square). (b) Hough transform of the binarized cropped image. We use standard Gaussian particle fitting to find maximum, which gives us the displacement $(\Delta x, \Delta y) = (3.7, -0.9)$. (c) Same as (a), but with the new particle position overlaid (red circle).

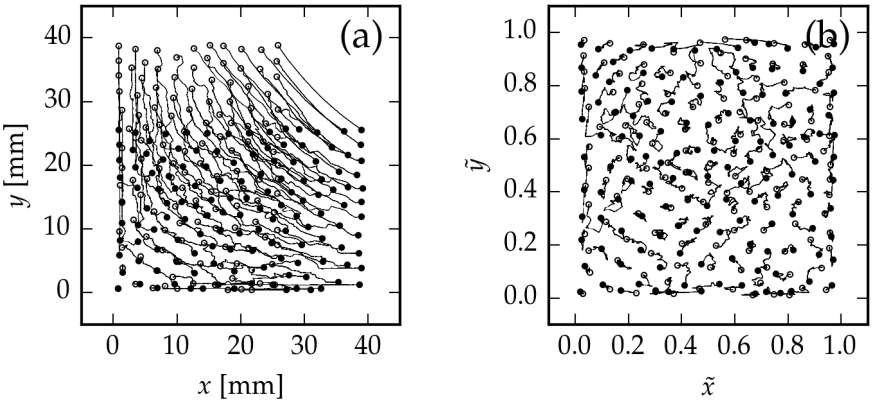

FIGURE 4.7: Particle trajectories for a $\phi = 0.85$ system under $\dot{\gamma} = 3 \times 10^{-5}$/s. Open circles indicate the starting position, closed circles the final positions. (a) Trajectories; (b) Affine-corrected trajectories. Video versions of these figures are available on-line [131, S5 and S6].

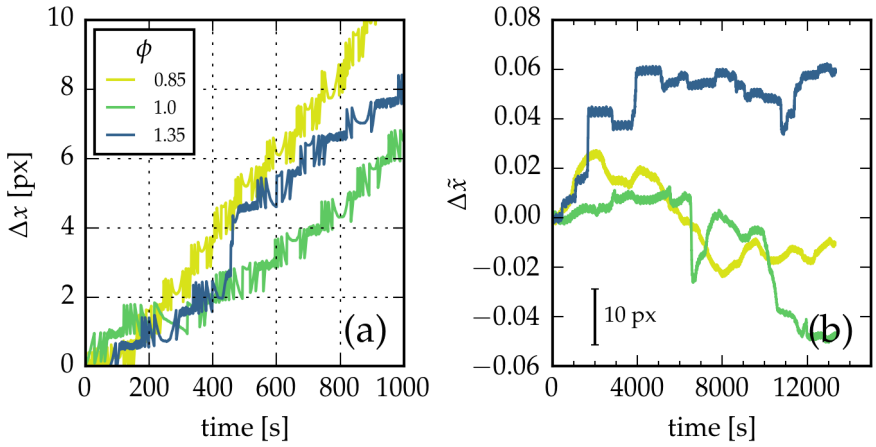

FIGURE 4.8: (a) $x(t)$ and (b) affine corrected $\tilde{x}(t)$ for three densities under $\dot{\gamma} = 3 \times 10^{-5}$/s. Notice the difference in scale — one pixel corresponds to $\Delta\tilde{x} \approx 2 \times 10^{-3}$, and (b) covers the full measurement rather than just the first 1000 s. The error in tracking is ± 1 px. The motion in $x(t)$ is dominated by the affine deformation. After subtracting the affine deformation, we observe distinct behaviors for different densities: smooth and nonaffine for low ϕ, and affine plateaus connected by jumps for high ϕ. Corresponding 2D trajectories are shown in Fig. 4.20.

We solve the first issue by manually marking the bubbles in the first frame, and solve the second issue by using a Hough circle transform (HCT) [141] rather than more commonly-used blob detection mechanisms, as the HCT does not require a contiguous area, and instead makes use of the circular symmetry of bubbles.

First, we choose a fixed threshold, chosen to maintain as much of the circular structure of the bubbles as possible. We apply this threshold to each image, and use these images as input to the HCT algorithm. To fit the new center of a particle at $t = t + 1$, we start with known old position (x_0, y_0) at $t = t$, and particle radius r. First, we crop the frame around (x_0, y_0) to $L = 2r + 4$ px on each axis. Next, we apply the Hough circle transform for $r = r$ on this cropped image. This results in an image with a single large peak, centered on the new position (x, y). We fit a 2D Gaussian to the image to retrieve the best fit for (x_1, y_1). We are able to track the complete particle paths for 95% of all particles. This process is illustrated

in Fig. 4.6. To bootstrap the process, we manually mark particles on the first frame of each experiment, and use HCT for a range of radii to find the best x, y and r. This process is repeated for each particle, and the resulting set of (x_0, y_0, r) are used as starting position for the tracking process.

After applying the iterative method, we have a set of coordinates $(x(t), y(t))$ for each particle. We show an example path for a $\phi = 0.85$ system under shear in Fig. 4.7(a). As before, the particle motion is dominated by the affine deformation field. To subtract the affine deformation field, we reshape the rectangular box to a square, and define

$$\tilde{x}(t) = x(t)/L_x \; ; \; \tilde{y}(t) = y(t)/L_y \; , \tag{4.15}$$

where the box lengths $L_x = L_{CD}/C_{\text{im}}$ and $L_y = L_B/C_{\text{im}}$ are known from the applied deformation. The resulting affine-corrected paths are shown in Fig. 4.7(b), where we observe the particles rarely move over large distances.

We will now investigate the accuracy of the tracking algorithm. In Fig. 4.8(a), we show $x(t)$ for a single particle for three different densities. We observe our particle tracking is fairly noisy, with an error in position of 1 px, or approximately 0.05 times the mean bubble diameter. Nonetheless, we can clearly follow the trajectories of the particles, and we note that these are dominated by the affine deformation field. In Fig. 4.8(b), we plot the affine corrected position of the same particle, for longer t. We can clearly distinguish different behavior for different densities ϕ: for low ϕ, the motion is smooth, while for high ϕ, the behavior can be described as purely affine (plateaus) plus discontinuous jumps. For intermediate ϕ we find intermediate behavior, with a combination of smooth drift and discontinuous jumps.

4.4 Results

Using the tools provided in the previous section, we will now focus on measuring qualitative and quantitative changes in the behavior of foam packings at varying density. We will use difference imaging to capture global changes, and will use particle tracking to investigate localized behavior.

Because we are working in a system where viscous effects play a significant role at higher shear rates, we will first investigate the time scale at which these effects play a role. We will then probe the structural relaxation

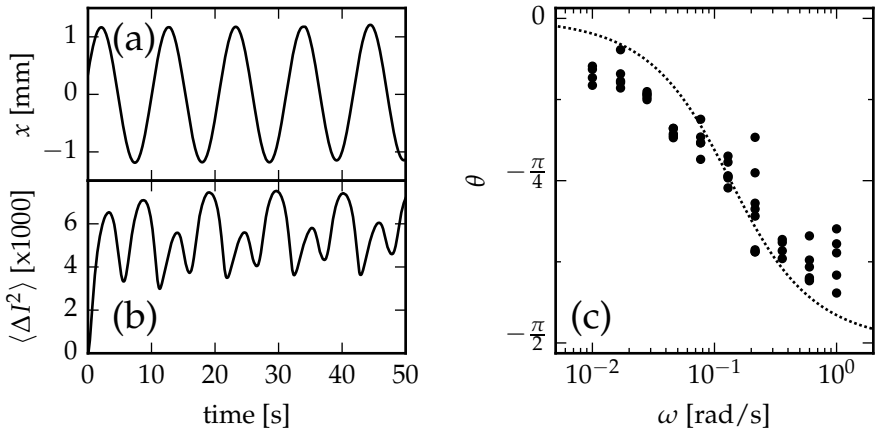

FIGURE 4.9: (a) Deformation $x = A\sin(\omega t)$, with $A = 1.2\,\text{mm}$ and $\omega = 0.6\,\text{rad/s}$. The maximum wall velocity is $A\omega = 0.72\,\text{mm/s}$. (b) The response of a foam ($\phi = 0.86$), compared to the state at $t = 0$. The system reaches a limit cycle after a few cycles. The frequency is double that of the driving, as both positive and negative driving lead the system away from the zero deformation state. The response is slightly anisotropic, as indicated by the difference in height of subsequent maxima. (c) Phase difference θ (see text for definition) as function of driving angular frequency ω, for $A = 1.2\,\text{mm}$ and $\phi = 0.86$. For each ω, we perform five measurements, each running for 20 cycles. The dotted line is a fit to $\tan^{-1}(-\omega/\omega_0)$, the expected phase shift for a first-order filter, with $w_0 = 0.14\,\text{rad/s}$. We observe the phase shift is somewhat slower than that of a first-order filter. Nonetheless, we observe almost the entire $\pi/2$ phase shift over three orders of magnitude in ω. The phase difference is small, although non-zero, at $\omega = 10^{-2}$ rad/s, indicating viscous effects are important for $\omega \gtrsim 10^{-2}$ rad/s.

time under step shear. As we will see, this time scale decreases strongly with ϕ. We then focus on measuring the global behavior from the difference imaging of foams under slow steady shear. We will show that the autocorrelation time strongly depends on ϕ, and will show qualitative trends in $\langle \Delta I^2 \rangle$. We then continue with data from tracked particles, and will show trends with ϕ in the mean squared displacement, the inverse participation ratio and the distribution of velocities.

4.4.1 Viscous time scale

First, we will determine the time scale at which viscous effects begin to dominate. Because the viscous damping is non-linear [142], the time scale depends on the velocity, and we will measure the scale for the velocities relevant in our experiment. We perform this measurement with a foam at density $\phi = 0.86$, as we expect the largest effects to emerge at low ϕ, where forces between particles are small.

To measure the viscous velocity scale, we drive the system with a sinusoidal deformation $x = A\sin(\omega t)$, where we use $A = 1.2\,\mathrm{mm}$ and vary ω from 10^{-2} rad/s to 1 rad/s (Fig. 4.9(a)). We measure the resulting image variance $\langle \Delta I^2 \rangle$ by comparing each frame to the initial frame (Fig. 4.9(b)). Because $\langle \Delta I^2 \rangle$ measures the deformation from the base state, it is positive for both positive and negative strain, and the resulting $\langle \Delta I^2 \rangle$ is quadratic in x.

We quantify the viscous effects with the phase shift θ. For this, we first determine the components of $\langle \Delta I^2 \rangle$ that are in-phase (X) and out-of-phase (Y) with x^2 as

$$X = \left\langle R\left(x^2(t)\right) \cdot R\left(\langle \Delta I^2 \rangle(t)\right) \right\rangle_t , \tag{4.16}$$

$$Y = \left\langle R\left(\frac{\partial}{\partial t} x^2(t)\right) \cdot R\left(\langle \Delta I^2 \rangle(t)\right) \right\rangle_t , \tag{4.17}$$

where we normalize the mean and standard deviation of each component using

$$R(q) = \frac{q - \langle q \rangle_t}{\langle (q - \langle q \rangle_t)^2 \rangle_t} . \tag{4.18}$$

We then calculate the phase shift

$$\theta = \tan^{-1}\left(Y/X\right) . \tag{4.19}$$

Although we did not measure a wide enough range of ω to measure the full shift from in-phase to $\pi/2$ out of phase behavior, we do observe a clear trend. At low driving rate $\omega = 10^{-2}$, we are close to in-phase behavior, and extrapolation suggests $\omega = 10^{-3}$ is slow enough to not have any noticeable viscous effects. $\omega = 10^{-3}$ corresponds to a wall velocity $v = A\omega = 1.2\,\mu\mathrm{m/s}$. At the typical wall length $L = 35\,\mathrm{mm}$, this

corresponds to a shear rate $\dot{\gamma} = 4 \times 10^{-5}$. Most of our measurements are at a lower rate, $\dot{\gamma} = 3 \times 10^{-5}$, but to measure the effect of shear rate, we also measure at higher rates. For these measurements, viscous effects start to play a role.

4.4.2 Structural relaxation time

In this section we investigate the relationship between the structural relaxation time and ϕ and $\dot{\gamma}$. To do so, we apply a step shear to the system, and image the resulting relaxation process. Using difference imaging, we quantify the process and then determine the timescales involved.

In Fig. 4.10(a), we show a step shear $\gamma = 5.3 \times 10^{-4}$ applied between $t = 0$ and $t = 0.5\,\mathrm{s}$. The system is then allowed to relax for 300 s, after which the next step is applied. Overall, we have an instantaneous shear rate $\dot{\gamma} = 10^{-3}$, and a mean shear rate $\dot{\gamma} = 2 \times 10^{-6}$. In Fig. 4.10(b), we show the variance $\langle \Delta I^2 \rangle$ between the first state after the step shear and each subsequent state. When we compare $\langle \Delta I^2 \rangle$ for a low and a high density system, we observe (i) a stronger response for the low density foam, and (ii) a slower decay for the low density foam.

We fit the resulting curve with an exponential

$$\langle \Delta I^2 \rangle = I_{\mathrm{max}} \left[1 - \exp\left(\frac{t - t_0}{\tau^*_{\mathrm{SR}}} \right) \right] , \tag{4.20}$$

where I_{max}, t_0 and τ^*_{SR} are free parameters in the fit. In Fig. 4.10(c), we plot the resulting value of τ^*_{SR} as a function of ϕ and step size γ. We observe that, for the smallest strain step $\gamma = 5.3 \times 10^{-4}$, the relaxation time decreases from $\tau^*_{\mathrm{SR}} \approx 40\,\mathrm{s}$ at $\phi = 0.85$ to $\tau^*_{\mathrm{SR}} \approx 6.7\,\mathrm{s}$ at $\phi = 1.3$. Larger strain steps result in longer relaxation times, where the relaxation time doubles from $\gamma = 5.3 \times 10^{-4}$ to $\gamma = 7.2 \times 10^{-3}$. I_{max}, i.e., $\langle \Delta I^2 \rangle$ for the final relaxed state, scales roughly linearly with the step size, and decreases slightly with increasing ϕ. This is likely due to relaxation of the system while it is being sheared, as $\langle \Delta I^2 \rangle$ is calculated with respect to the first state after the step shear.

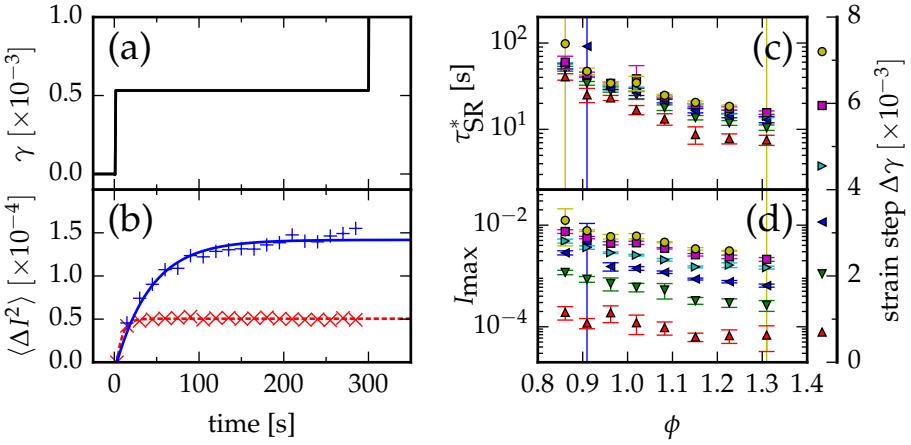

FIGURE 4.10: (a) The applied step shear $\gamma = 5.3 \times 10^{-4}$ is applied between $t = 0$ and 0.5 s. The system is then relaxed for 300 s. (b) $\langle \Delta I^2 \rangle$ for $\phi = 0.85$ (blue pluses) and $\phi = 1.3$ (red crosses), with an exponential fit $\langle \Delta I^2 \rangle = I_{max}(1 - \exp((t - t_0)/\tau^*_{SR})$ ($\phi = 1.3$: $\tau^*_{SR} = 6.7$ s, $I_{max} = 5.0 \times 10^{-5}$; $\phi = 0.85$: $\tau^*_{SR} = 42$ s, $I_{max} = 1.4 \times 10^{-4}$). (c) τ as a function of density ϕ. Markers indicate the mean, error bars indicate the standard deviation. Symbols and colors indicate the strain step size. We observe structural relaxation times are a factor 5 longer for low ϕ than for dense systems. Larger strain steps correspond to longer decay times, but a factor 30 in step size only results in a 2 times longer decay. (d) I_{max} as a function of density ϕ. I_{max} scales roughly linearly with step size, and decreases slightly with density.

4.4.3 Difference imaging

We will now focus on several measures we obtain from difference imaging. First, we will discuss the behavior of $\langle \Delta I^2 \rangle$ as a function of both time t and the time step Δt. We will first show qualitatively how the behavior changes as a function of ϕ in uniaxial compression. We will then show the expected behavior for a single bubble in a synthetic example, and show that the behavior can be described by a power law on short time scales. Once we have set up this framework, we turn to the behavior of foam under pure shear. We will first determine the autocorrelation time, and will then investigate trends with ϕ in nonaffine behavior and the occurrence of rearrangements.

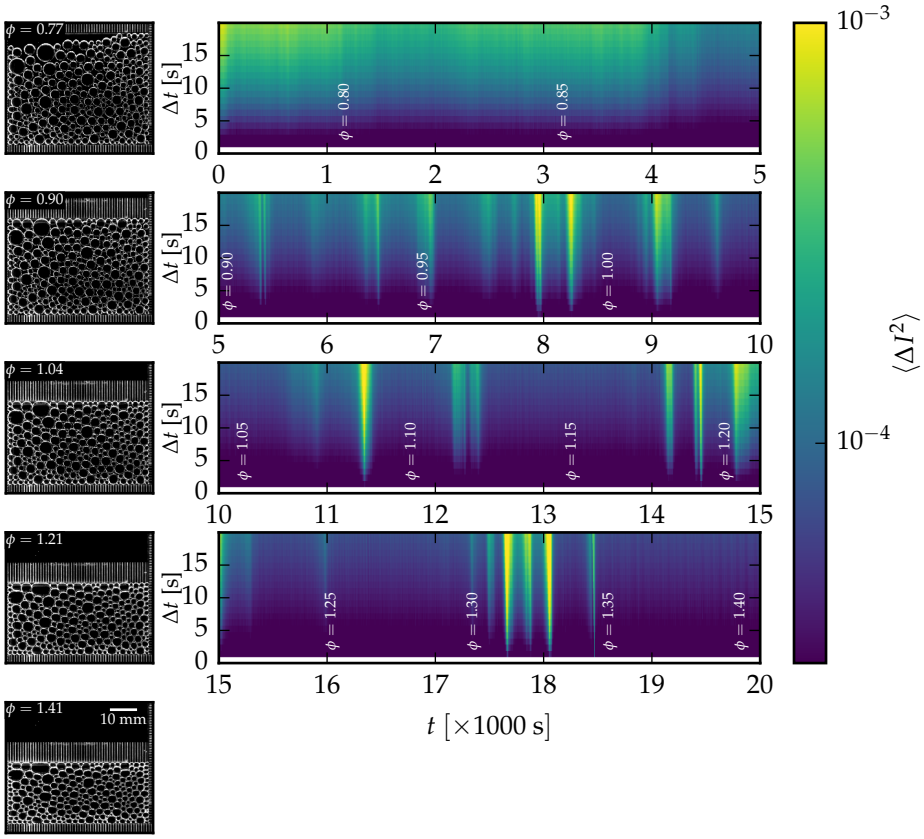

FIGURE 4.11: Compression of a two-dimensional foam from $\phi = 0.77$ to $\phi = 1.41$ under $\dot{\varepsilon} = -3 \times 10^{-5}$/s. (left row) Snapshots at $\phi = 0.77$, 0.90, 1.04, 1.21 and 1.41, corresponding to $t = 0$ s, 5000 s, 10 000 s, 15 000 s and 20 000 s. The size is indicated with a scale bar. (right row) Flame graphs of $\langle \Delta I^2 \rangle(t, \Delta t)$. Densities are indicated at every 5% change in ϕ. With increasing confinement, we observe a transition from fully smooth to fully intermittent behavior. A video version of this figure is available on-line [131, S7].

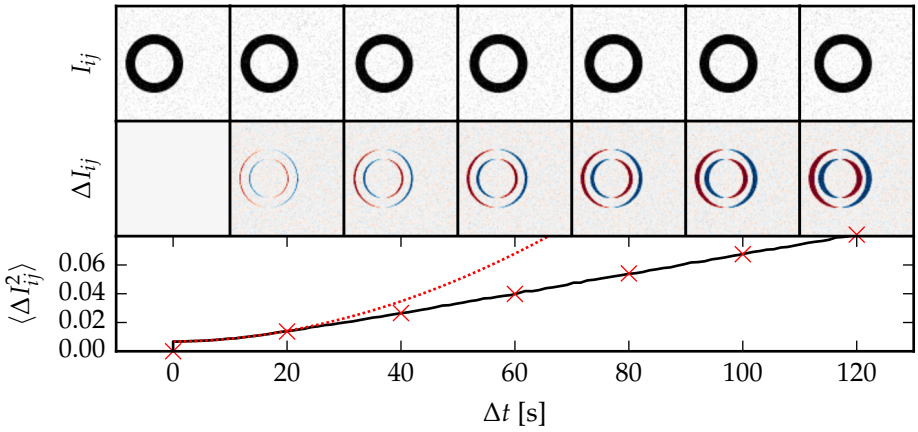

FIGURE 4.12: Example of difference imaging. (top) A particle, here modeled with an annulus with inner radius $r = 16$ px and outer radius $R = 24$ px, moves horizontally at $v = 0.01$ px/s. The intensity of the ring is $I = 1$. A Gaussian noise term with standard deviation $s = 1/16$ is added to simulate imaging noise. (middle) Difference images show the displaced particle as a set of four crescents. (bottom) By averaging over the squared differences, we capture the displacement in a single number. Red crosses indicates values corresponding to the ΔI_{ij} images. Values computed from intermediate annulus positions are shown with a black line. A power law fit $A(\Delta t)^\beta + C$ to $0 < \Delta t < 20$ is shown with the red dotted line ($A = 2.3 \times 10^{-5}$, $\beta = 1.9$, $C = 0.007$).

In Fig. 4.11, we show a *flame graph* of $\langle \Delta I^2 \rangle(t, \Delta t)$ for a system under uniaxial compression: using color and intensity, we show $\langle \Delta I^2 \rangle$ as a function of both t (x) and Δt (y). At $t = 0$, we start at $\phi = 0.77$. For $\phi < \phi_j \approx 0.84$, the behavior is completely smooth, and $\langle \Delta I^2 \rangle$ varies slowly. Above ϕ_j, we observe a larger variety in motion, with 'hot' and 'cold' sections. Nonetheless, $\langle \Delta I^2 \rangle$ still varies slowly. When we increase ϕ further, we observe sharp triangles that are characteristic of intermittent behavior in the system (Fig. 4.13).

We now turn to capturing this behavior in simpler parameters. To do so, we first focus on a synthetic example of a single moving bubble. In Fig. 4.12, we show a synthetic bubble (annulus) moving horizontally. We then determine the difference image as compared to the original state. Finally, we calculate $\langle \Delta I^2 \rangle$ for these difference images, and plot $\langle \Delta I^2 \rangle$ as

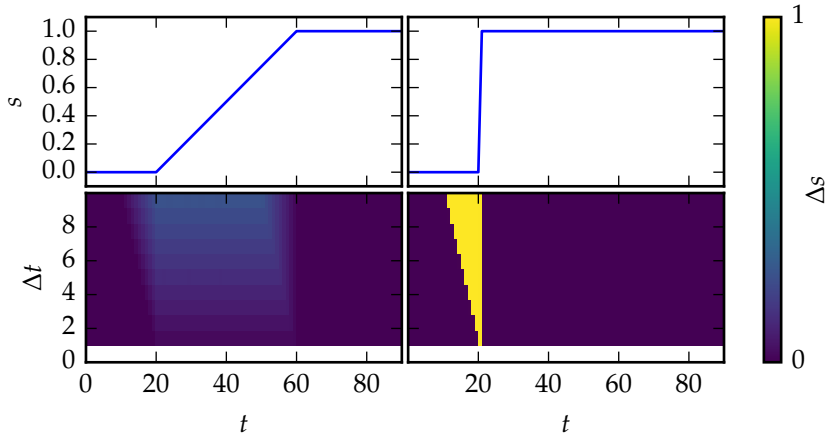

FIGURE 4.13: $t, \Delta t$ flame graphs for two examples: a linearly increasing function (a,c), and a step function (b,d). For the linearly increasing function, we observe a smooth flame graph, with an increased Δs for increased Δt. For the step function, we observe a sharp triangular shape — if the step happens between t and $t + \Delta t$, $\Delta s = 1$. Otherwise, $\Delta s = 0$. When we approach the event at $t = 20$, we capture the event for a wider range of Δt; this is the leading edge of the triangle. After the event, $s = 1$, and $\Delta s = 0$, irrespective of Δt, and we find that the trailing edge of the triangle is sharp.

a function of Δt. We find that the behavior on short timescales can be well-described as a power law, and we therefore summarize the behavior of $\langle \Delta I^2 \rangle$ for different Δt by fitting $\langle \Delta I^2 \rangle$ to

$$\langle \Delta I^2 \rangle (\Delta t) = A \left(\frac{\Delta t}{1\,\mathrm{s}} \right)^{\beta} + C \,, \tag{4.21}$$

where A, β and C are fit parameters, for $\Delta t \leq 20\,\mathrm{s}$. This gives us a rate of nonaffine behavior $A = 2.3 \times 10^{-5}$ and a power $\beta = 1.9$. $C = 0.007$ captures the offset resulting from imaging noise.

We now turn to the behavior for real foams under shear. In Figs. 4.14(a) and (b), we show flame graphs for a low density ($\phi = 0.9$) and a high density ($\phi = 1.5$) foam, sheared at the same rate $\dot{\gamma} = 3 \times 10^{-5}$. We observe large qualitative differences. For the dense foam, we observe the behavior is largely affine, indicated by the low value of $\langle \Delta I^2 \rangle$, even at $\Delta t = 20\,\mathrm{s}$ ($\langle \Delta I^2 \rangle \sim 10^{-4}$). The exception to this are rearrangements, recognizable by

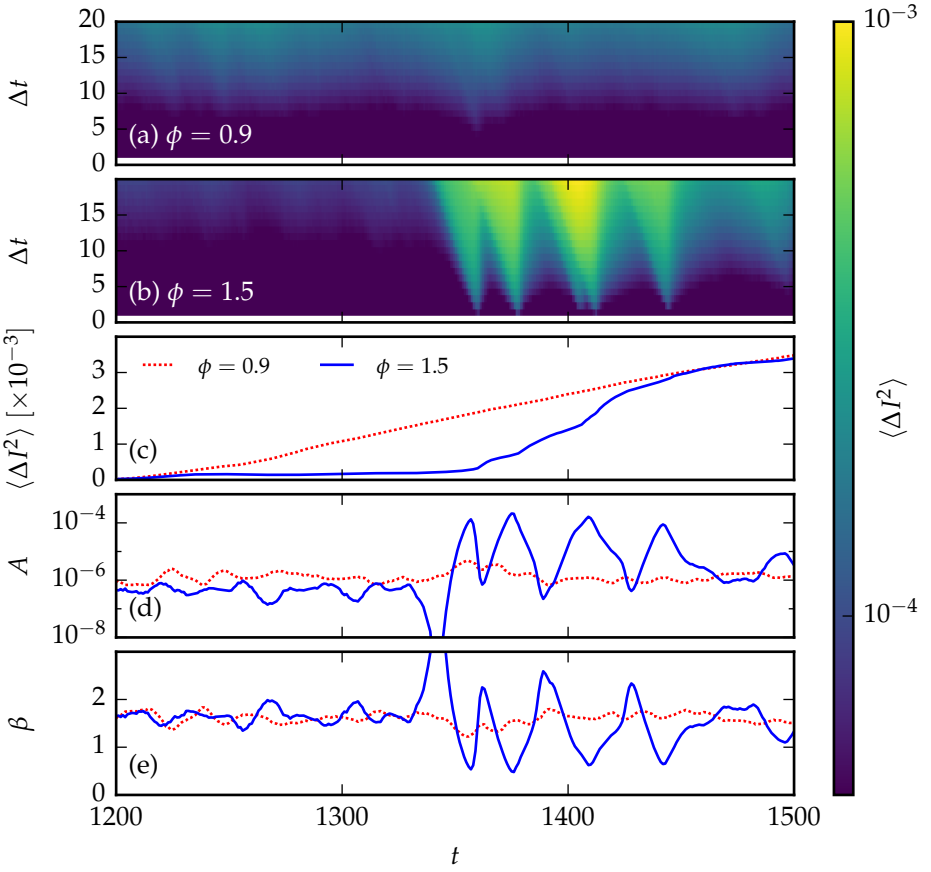

FIGURE 4.14: Behavior of $\langle \Delta I^2 \rangle(t, \Delta t)$ for a low density ($\phi = 0.9$) and a high density ($\phi = 1.5$) foam. Both samples are sheared with a constant shear rate $\dot{\gamma} = 3 \times 10^{-5}$/s (total strain $\Delta\gamma = 9 \times 10^{-3}$). (a) Intensity plot of $\langle \Delta I^2 \rangle(t, \Delta t)$ for $\phi = 0.9$. Larger Δts lead to larger $\langle \Delta I^2 \rangle$, but the behavior is largely time-independent. (b) $\langle \Delta I^2 \rangle(t, \Delta t)$ for $\phi = 1.5$. Here, we can clearly distinguish individual events, which show up as bright triangles. (c) Image variance when compared to the state at $t = 1200$ s. The low density system has a slow but consistent increase. The high density system generally has a slow growth, but has significant jumps when rearrangements occur. (d,e) The results from fitting $\langle \Delta I^2 \rangle(t, \Delta t) = A \times (\Delta t)^{\beta} + C$. For the low density, $A \approx 10^{-6}$ and $\beta \approx 1.6$ are fairly constant, while we can clearly distinguish the quiet and active periods for the high density foam. Video versions of these figures are available on-line [131, S8 and S9].

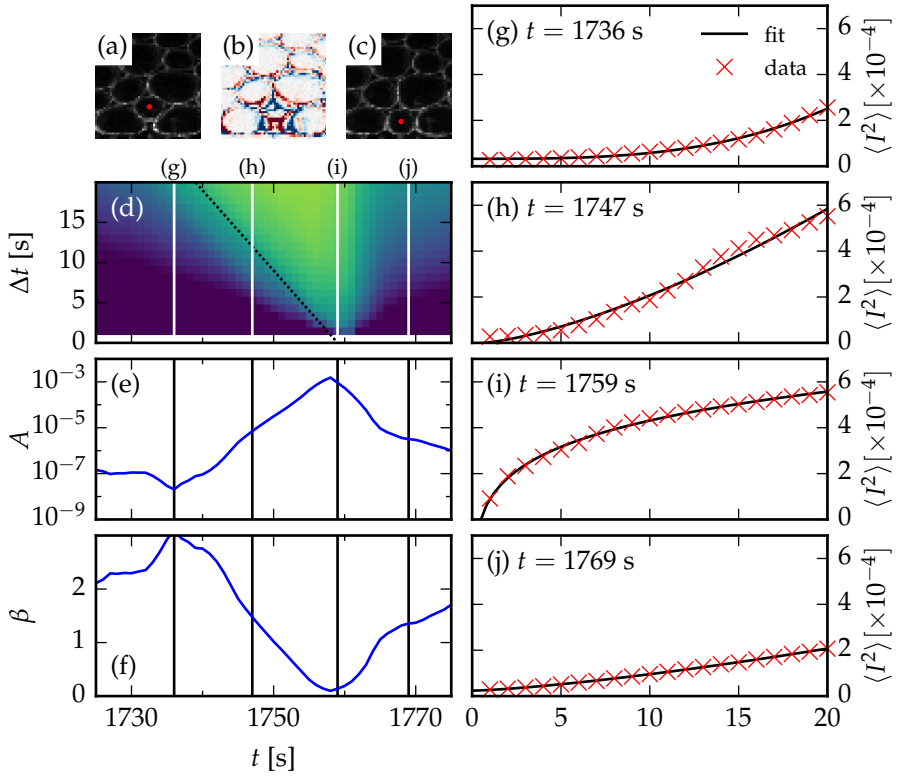

FIGURE 4.15: Example of a rearrangement in a dense ($\phi = 1.5$) foam under shear ($\dot{\gamma} = 3 \times 10^{-5}$). (a-c) Snapshots at $t = 1730$ s and $t = 1770$ s and the corresponding difference image. The bubble marked with a red dot moves down to the lower wall. (d) The corresponding $\langle \Delta I^2 \rangle (t, \Delta t)$ intensity plot. The intensity profile roughly follows the dotted line $t + \Delta t = 1759$ s. (e,f) The corresponding amplitude $A(t)$ and power $\beta(t)$. β peaks and A starts to increase when the first sign of the event enters our fit range (g). The maximum A and minimum β are just before the rearrangement (i). In the intermediate regime (h) we find the behavior is not well-described by a power law. Finally, we recover the regular $\beta \approx 1.6$ when most motion has dissipated (j).

their distinctive triangular shape, as explained in Fig. 4.13. In contrast, for the low density foam, we do not observe distinct rearrangements, but $\langle \Delta I^2 \rangle$ is typically higher by a factor 2, indicating a larger amount of nonaffine motion.

We fit Eq. (4.21) to $\langle \Delta I^2 \rangle(t, \Delta t)$ for every value of t, and plot the resulting $A(t)$ and $\beta(t)$ in Figs. 4.14(d) and (e). $C(t) \approx 6.25$ (not shown) is essentially independent of time and corresponds to approximately 2.5 bits of imaging noise. For the low-density system, we observe a constant $A \approx 10^{-6}$ and $\beta \approx 1.6$. For the high-density system, we observe $A \approx 5 \times 10^{-7}$, $\beta \approx 1.6$ for the quiet parts, while A and β strongly vary near rearrangements.

In Fig. 4.15, we now focus on the behavior of A and β near rearrangements. In Figs. 4.15(a-c), we show the before and after state of the rearrangement, with their difference image. A single bubble worms its way in between two larger particles. In Fig. 4.15(d-f), we show the behavior of $\langle \Delta I^2 \rangle(t, \Delta t)$, $A(t)$ and $\beta(t)$ for this rearrangement. We observe the characteristic triangular shape, and observe $A(t)$ increases strongly close to the event at $t = 1758\,\mathrm{s}$. β peaks approximately 20 s before the event, where the first precursor of the event enters the fit interval, and dips to $\beta \approx 0.1$ at the event. In Figs. 4.15(g-j), we show $\langle \Delta I^2 \rangle(t, \Delta t)$ for four values of t, indicating the variety of behaviors around a rearrangement.

Autocorrelation time. We now first focus on determining the autocorrelation time of motion in the system from $A(t)$ and $\beta(t)$. First, we combine $A(t)$ and $\beta(t)$ into a single *signal function*

$$\alpha(t) = \log_{10} A(t) + \mu\beta(t)\,, \tag{4.22}$$

where $\mu = 1$ was chosen to optimize the signal to noise ratio. We then normalize α as

$$\tilde{\alpha}(t) = \frac{\alpha(t) - \langle \alpha(t) \rangle_t}{\left\langle (\alpha(t) - \langle \alpha(t) \rangle_t)^2 \right\rangle_t^{1/2}}\,, \tag{4.23}$$

whose mean is 0 and standard deviation is 1. We then calculate the autocorrelation function

$$R_{\alpha\alpha}(\tau) = \langle \tilde{\alpha}(t+\tau) \cdot \tilde{\alpha}(t) \rangle_t \;.is \tag{4.24}$$

In Fig. 4.16(a), we show the autocorrelation function $R_{\alpha\alpha}(\tau)$ for $\phi = 0.85 \ldots 1.5$ under a steady shear $\dot{\gamma} = 3 \times 10^{-5}/\mathrm{s}$. We observe a strong effect of ϕ: $R_{\alpha\alpha}(\tau)$ decreases much more rapidly for high densities.

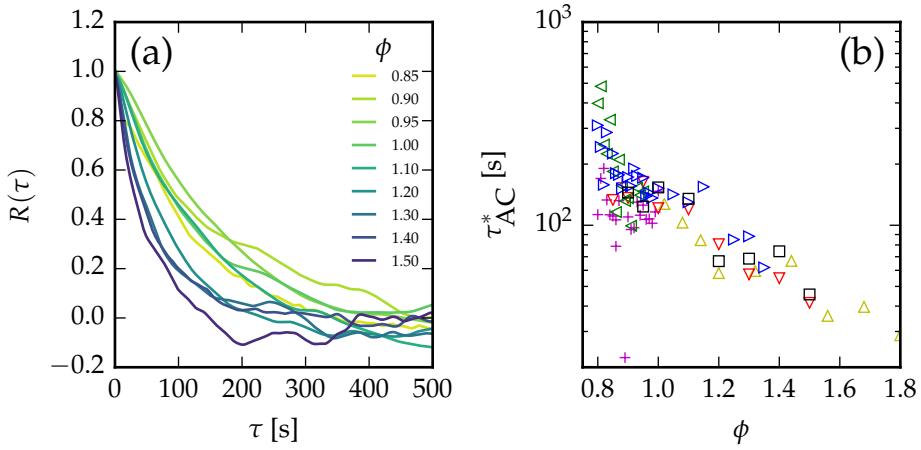

FIGURE 4.16: (a) Autocorrelation function $R(\tau)$ for a range of systems at $\phi = 0.85 \ldots 1.5$, under pure shear at $\dot{\gamma} = 3 \times 10^{-5}$. Higher values of ϕ correlate with a faster decay of $R(\tau)$. We fit each function with $R(\tau) = \exp((\tau - \tau_0)/\tau^*)$ with τ_0 and τ^* as free parameters. (b) Characteristic time scale τ^* as a function of ϕ for all measurements at $\dot{\gamma} = 3 \times 10^{-5}$. Different colors indicate seven different measurement series. For $\phi < 1$, the scatter between measurements is large, although we recover the same trend, where τ^* decreases for increasing ϕ, for each measurement series. For higher densities, we find consistent behavior between different series.

We determine the autocorrelation *time* by fitting $R_{\alpha\alpha}$ with

$$R_{\alpha\alpha}(\tau) = \exp\left(\frac{\tau - \tau_0}{\tau^*_{AC}}\right) , \tag{4.25}$$

where τ_0 and τ^*_{AC} are free parameters in the fit. In Fig. 4.16(b), we now show the autocorrelation time τ^*_{AC} as a function of density ϕ for seven independent measurement series at $\dot{\gamma} = 3 \times 10^{-5}/\text{s}$. We observe comparable behavior for all series, where $\tau^*_{AC} \approx 500\,\text{s}$ for $\phi = 0.85$ and $\tau^*_{AC} \approx 50\,\text{s}$ for $\phi = 1.3$.

In Fig. 4.17(a), we focus on the relation between τ^*_{AC} and the shear rate $\dot{\gamma}$. We observe τ^*_{AC} is strongly dependent on $\dot{\gamma}$, with a scaling not in contradiction with $\tau^*_{AC} \sim \dot{\gamma}^{-1}$. This suggests motion in the system is most strongly correlated with a *strain* scale rather than a time scale, consistent with quasi-static shear.

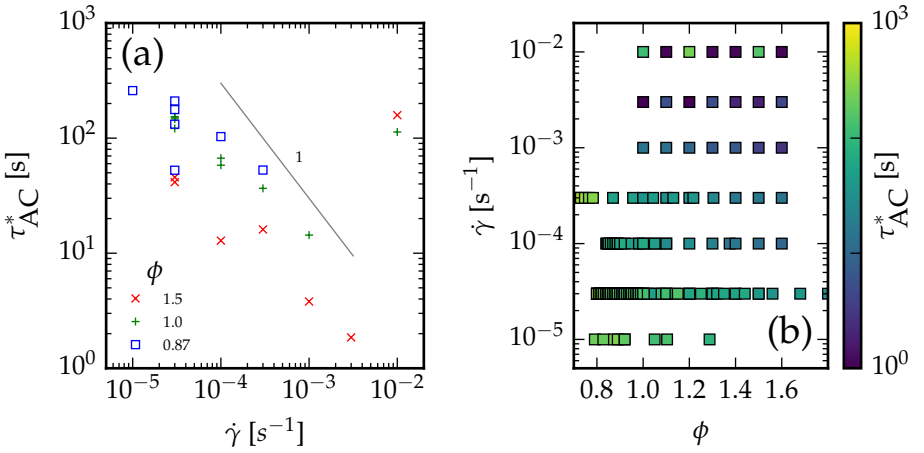

FIGURE 4.17: (a) Characteristic time scale τ^* as a function of shear rate $\dot{\gamma}$ for three densities ϕ. We observe τ^* decreases roughly as $\dot{\gamma}^{-1}$, suggesting we are dealing with a characteristic *strain* scale rather than a *time* scale. (b) τ^* as a function of both ϕ and $\dot{\gamma}$. Both trends are clearly visible: higher ϕ and higher $\dot{\gamma}$ both lead to smaller values of τ^*_{AC}.

Nonaffine behavior and rearrangements. We now focus on the nonaffine behavior of foams. From jamming simulations, it is well known that behavior near the jamming transition becomes increasingly nonaffine [32], while the behavior in dry foams is largely affine, interspersed with rearrangement events [135].

Here, we will investigate the nonaffine behavior as measured by the image variance $\langle \Delta I^2 \rangle$. In Fig. 4.14(c), we show $\langle \Delta I^2 \rangle$ as a function of Δt, i.e., we measure how $\langle \Delta I^2 \rangle$ builds up over longer periods of time. For high ϕ, we observe $\langle \Delta I^2 \rangle$ grows slowly with Δt, except when rearrangements happen, causing a jump in the signal. For low ϕ, the behavior is remarkably different: there are no distinct events, and $\langle \Delta I^2 \rangle$ grows smoothly with time. Nevertheless, $\langle \Delta I^2 \rangle$ reaches values comparable to those of a rearrangement at $t \approx 1450\,\mathrm{s}$.

By fitting $\langle \Delta I^2 \rangle$ to Eq. (4.21), we capture the nonaffine behavior in a single parameter $A(t)$. For purely affine behavior, $A(t) = 0$, and $A(t)$ grows with increasing nonaffinity. We thus expect typical values of $A(t)$ to be small for high ϕ, and large close to jamming. $A(t)$ also captures the effect

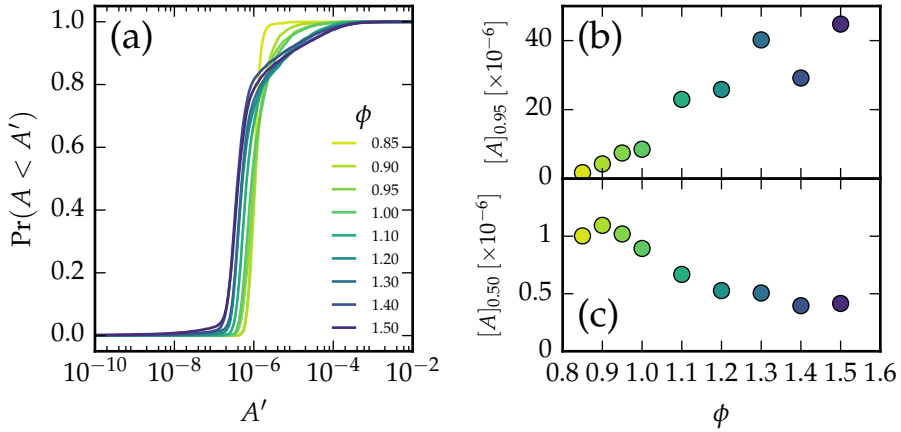

FIGURE 4.18: (a) CDFs $\Pr(A < A')$ for fitting parameter A. The typical value of A is higher for low ϕ, but the peaks are much larger for high ϕ. (b) 5%, 50% (median) and 95% percentiles of A as a function of packing fraction ϕ. The median A decreases with ϕ, but the 95% percentile, i.e. peaks in the signal, becomes more prominent for higher ϕ.

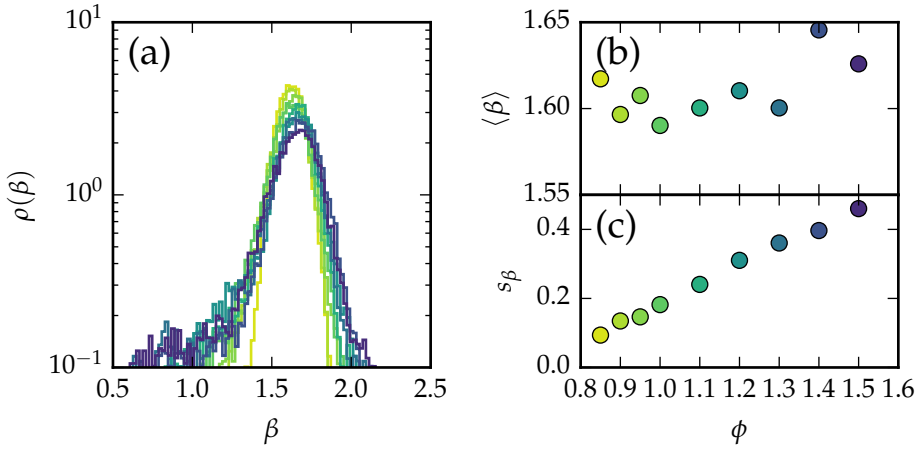

FIGURE 4.19: (a) PDFs of $\beta(t)$ for systems at a range of densities ϕ. For higher densities, the distribution becomes wider, and a tail towards low β appears. (b) The mean $\langle\beta\rangle$ does not change with ϕ. (c) The standard deviation s_β increases linearly with ϕ.

of rearrangements: at a rearrangement, $A(t)$ shortly peaks, with values 100 to 1000 times larger than typical (Fig. 4.14(d)). For larger time scales, this causes $\langle \Delta I^2 \rangle$ to reach comparable values for both low and high ϕ.

We capture both behaviors in Fig. 4.18(a), where we have plotted CDFs of $A(t)$. For low densities, we observe the CDF is close to a step function, indicating all values of $A(t)$ are close to the typical values — in other words, there are no rearrangements where $A(t)$ jumps to a high value. For increasing ϕ, we observe two effects. First, the *typical* value of $A(t)$ halves, from $[A(t)]_{0.5} \approx 10^{-6}$ at $\phi = 0.85$ to $[A(t)]_{0.5} \approx 4 \times 10^{-7}$ at $\phi = 1.5$. Second, the shape no longer resembles a step function for high densities. Instead, we find the upper 20% percentile now consists of values much larger than the median, consistent with the appearance of rearrangements.

In Figs. 4.18(b) and 4.18(c), we plot the median $[A]_{0.5}$ and the 95% percentile $[A]_{0.95}$ as a function of ϕ, and find the behavior indicated above. $[A]_{0.5}$ decreases smoothly with ϕ, and seems to reach a plateau around $\phi = 1.4$. $[A]_{0.95}$ increases roughly linearly with $\Delta\phi$, up to 4×10^{-5} at $\phi = 1.5$.

We can also capture the rearrangement behavior using the power law exponent $\beta(t)$. In Fig. 4.14(e), we have seen $\beta(t) \approx 1.6$ in steady state, without any large-scale deviations. However, near rearrangements, $\beta(t)$ fluctuates strongly. In Fig. 4.19(a), we plot the PDFs of β for different ϕ. For increasing ϕ, we observe (i) the peak of the distribution shifts to higher β, (ii) the width of the distribution increases, and (iii) a tail at low β forms. In Fig. 4.19(b), we plot the mean value of β, and observe $\langle \beta \rangle = 1.6$, independent of ϕ. At the same time, the standard deviation of β grows from 0.1 at $\phi = 0.85$ to 0.5 at $\phi = 1.5$ (Fig. 4.19(c)).

Conclusion. We have observed several trends with density ϕ. First, we quantified the autocorrelation time, and observed it decreases with a factor 30 between $\phi = 0.85$ and $\phi = 1.5$. We observed qualitative changes in nonaffine behavior from the distribution of $A(t)$, where we observe the amount of nonaffine behavior decreases with density ϕ. Finally, we observed qualitative changes in the prevalence of rearrangements from the $[A]_{0.95}$ and the standard deviation of $\beta(t)$.

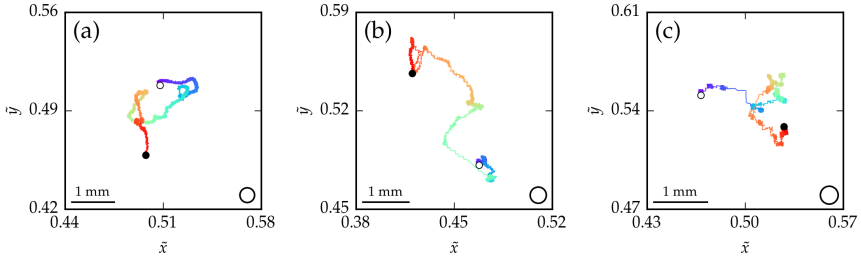

FIGURE 4.20: Affine-corrected particle trajectories for a single particle for systems under continuous shear $\dot{\gamma} = 3 \times 10^{-5}/\text{s}$. (left) $\phi = 0.85$, (middle) $\phi = 1$, (right) $\phi = 1.35$. Color changes with time. We observe a qualitative change in behavior: at low ϕ, the bubble follows a smooth path through space, while at the highest ϕ, the particle jumps around between caged states. The intermediate $\phi = 1$ exhibits a mixture of both behaviors. Circles indicate the Lindemann criterion $r = 0.14\langle r \rangle$.

4.4.4 Tracked particle trajectories

We will now focus on the behavior of the systems using tracked particle trajectories. First, we focus on differences in the motion of individual particles, where we observe a transition from smooth behavior at low ϕ to caged behavior at high ϕ. We will then look at various measures to quantify these differences. First, we focus on the mean squared displacement, where we find smaller displacements for larger ϕ at the same Δt, but no clear signature of a caging timescale. We then investigate localization directly using the inverse participation ratio and by characterizing the distribution of velocities.

Caged motion. We first focus on trajectories of individual particles. In Fig. 4.20, we show the particle trajectory for a single particle in the middle of the system for three systems at different densities. We observe a clear qualitative trend, consistent with Fig. 4.8(b): the low density system smoothly moves across phase space, while the high density system is in a 'cage' which deforms affinely, and the particle jumps from cage to cage. For intermediate ϕ, we find intermediate behavior.

Mean squared displacement. To quantify this behavior, we turn to the mean squared displacement (MSD). We calculate the MSD from the particle

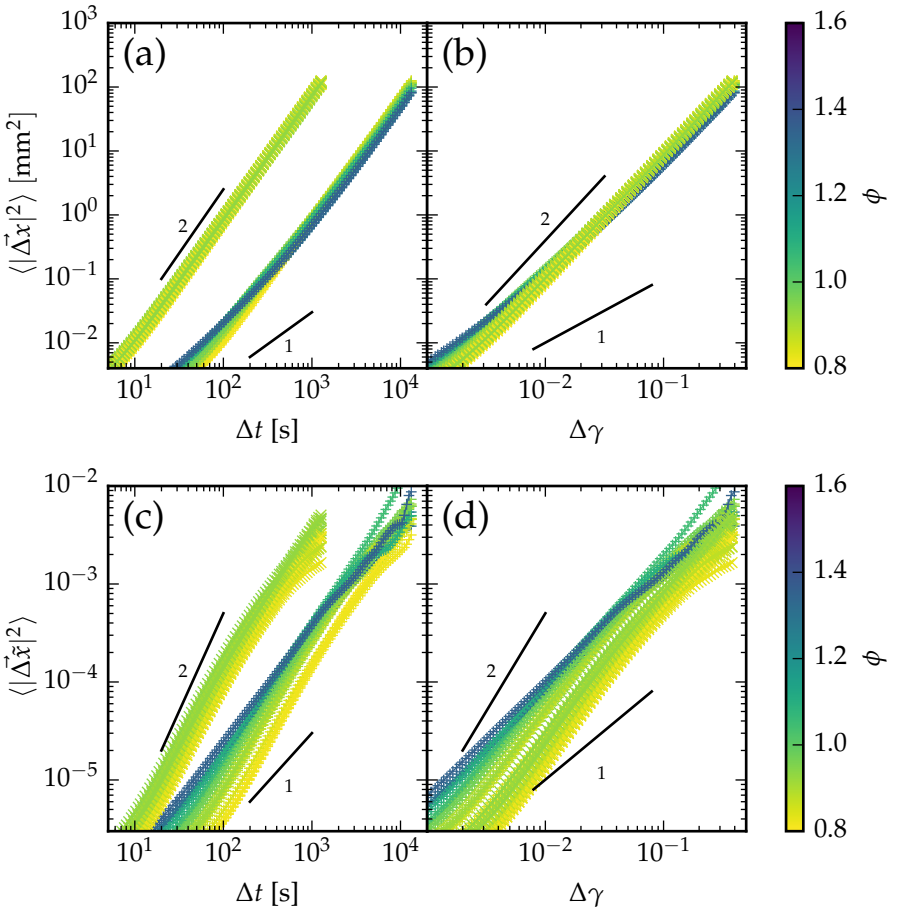

FIGURE 4.21: Mean squared displacement for systems at a range of ϕ (colors) at $\dot{\gamma} = 3 \times 10^{-5}$/s (pluses) or $\dot{\gamma} = 3 \times 10^{-4}$/s (crosses). (a,b) MSD as function of Δt and $\Delta\gamma$. (c,d) Affine corrected MSD as function of Δt and $\Delta\gamma$. In all figures, power laws corresponding to diffusive (1) and ballistic (2) motion are indicated.

positions as

$$\langle|\overrightarrow{\Delta x}|\rangle(t,\Delta t) = \left\langle (x_i(t+\Delta t) - x_i(t))^2 + (y_i(t+\Delta t) - y_i(t))^2 \right\rangle , \quad (4.26)$$

where the average is taken over all particles and all times t. Our particle positions are accurate to up to 1 px, and we therefore expect reliable results for $\langle|\overrightarrow{\Delta r}|\rangle > 1\,\mathrm{px}^2 \approx 4 \times 10^{-3}\,\mathrm{mm}^2$, or 3×10^{-6} in affine-corrected units.

In Fig. 4.21(a), we show $\langle|\overrightarrow{\Delta x}|^2\rangle$ for shear measurements at shear rates $\dot{\gamma} = 3 \times 10^{-5}$/s and $\dot{\gamma} = 3 \times 10^{-4}$/s at a range of density ϕ. First, we observe that the curves describe ballistic behavior, consistent with motion that is largely dominated by the affine deformation. Next, we observe that the curves for $\dot{\gamma} = 3 \times 10^{-5}$/s and $\dot{\gamma} = 3 \times 10^{-4}$/s are separated by an order of magnitude in time. In Fig. 4.21(b), we have plotted the curves as a function of strain and observe the curves almost collapse. Finally, we observe a trend with ϕ for $\dot{\gamma} = 3 \times 10^{-5}$/s: higher densities have a larger $\langle|\overrightarrow{\Delta x}|^2\rangle$ at small Δt, but have a slower growth: at $t \approx 3 \times 10^2$ s, $\langle|\overrightarrow{\Delta x}|^2\rangle$ is approximately equal for all ϕ. At longer timescales, $\langle|\overrightarrow{\Delta x}|^2\rangle$ is larger for lower densities.

For the affine corrected $\langle|\overrightarrow{\Delta \tilde{x}}|^2\rangle$, we find comparable behavior, albeit without a clear crossing time. $\langle|\overrightarrow{\Delta \tilde{x}}|^2\rangle$ is larger for low ϕ at small Δt, but grows more rapidly for low ϕ. $\langle|\overrightarrow{\Delta \tilde{x}}|^2\rangle$ grows slower as a function of $\Delta\gamma$ for $\dot{\gamma} = 3 \times 10^{-4}$/s than for $\dot{\gamma} = 3 \times 10^{-5}$/s, suggesting nonaffine behavior is more prominent at low shear rates.

We note that we do not observe plateaus in the mean squared displacement function, as typically associated with caging behavior [143, 144]. This suggest there is no typical time or spatial scale for these cages, causing the plateaus to be averaged out.

Inverse participation ratio. Another hallmark of rearrangements is their localization in space: typically, only four particles (a *T1* event) or a small group of particles (a *shear transformation zone* or STZ) are participating. We quantify this behavior using the Inverse Participation Ratio (IPR), defined as

$$\Lambda(t) = \frac{\langle|\Delta\vec{\tilde{r}}|^4\rangle}{\langle|\Delta\vec{\tilde{r}}|^2\rangle^2} , \quad (4.27)$$

where $\overrightarrow{\Delta\tilde{r}}$ is the displacement in affine-corrected coordinates within a time step Δt and the average is taken over all particles. We choose $\Delta t = 10$ s, as

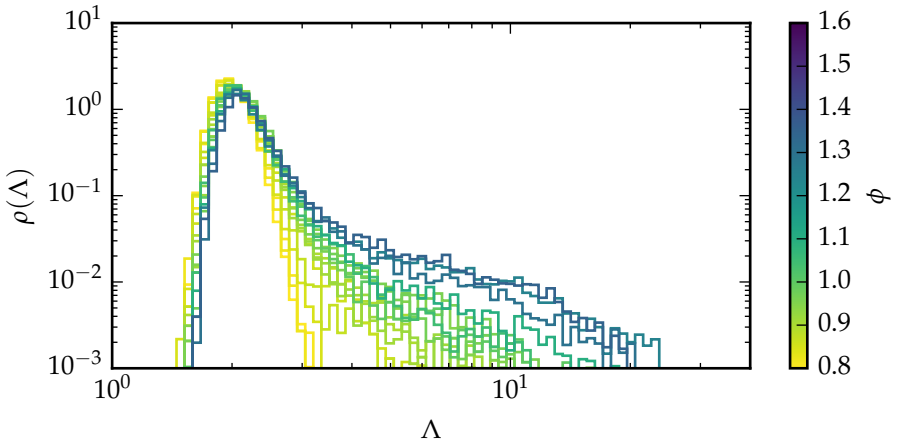

FIGURE 4.22: PDFs of the inverse participation ratio Λ (see text), for foams sheared at $\dot{\gamma} = 3 \times 10^{-5}/\mathrm{s}$. Λ is determined using a time step $\Delta t = 10\,\mathrm{s}$. For $\phi = 0.85$, the PDF is approximately Gaussian. For increasing ϕ, and increasingly prominent tail at high Λ forms, indicating the appearance of rearrangements.

this corresponds to the shortest time scale where the particle tracking is not dominated by noise, as we observed in the mean squared displacement Fig. 4.21(a). To interpret this value, we note that for a fully homogeneous system, $\langle |\Delta\vec{r}|^4 \rangle = \langle |\Delta\vec{r}|^2 \rangle^2$, and $\Lambda = 1$. For a fully localized system, where only a single particle i has a finite $\Delta\vec{r}$, $\langle |\Delta\vec{r}|^4 \rangle = |\Delta\vec{r}_i|^4/N$, while $\langle |\Delta\vec{r}|^2 \rangle^2 = |\Delta\vec{r}_i|^4/N^2$, so $\Lambda = N$, where N is the number of particles. In numerical simulations of particles with viscous interactions, Woldhuis et al. [38] measured the IPR of the energy dissipation between particles, and observed the IPR increased from ≈ 3 at low ϕ and high $\dot{\gamma}$ to ≈ 286 at high ϕ and low $\dot{\gamma}$. Here, we observe comparable behavior: In Fig. 4.22, we show PDFs of $\Lambda(t)$ for a range of ϕ ($\dot{\gamma} = 3 \times 10^{-5}/\mathrm{s}$, $\Delta t = 10\,\mathrm{s}$), and observe that the tail of the distribution becomes much more prominent at higher ϕ. We observe an increase in the prevalence of high values, indicating there are more rearrangement events at higher ϕ. We also observe that the maximum observed value increases, indicating the events become more and more localized. For high densities, we find the maximum IPR is $\max \Lambda \approx 25$. When we take the number of samples into account, this is comparable to the results found by Woldhuis et al. [38].

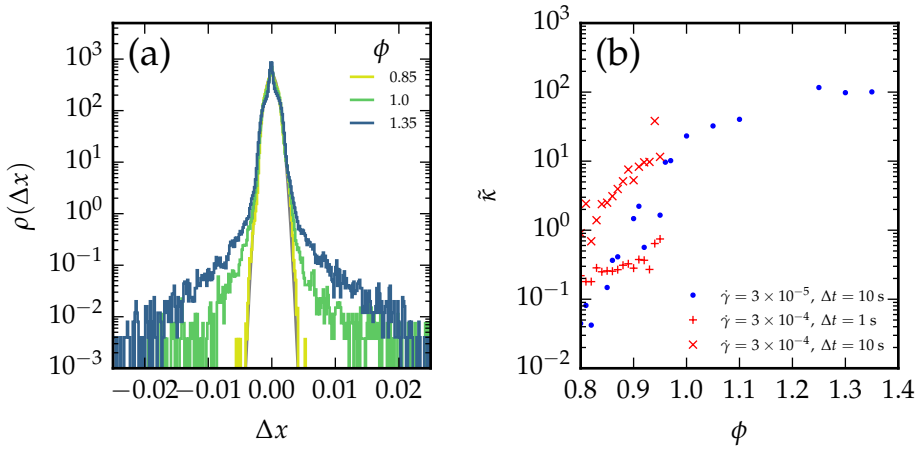

FIGURE 4.23: (a) PDFs of Δx for three densities ($\dot{\gamma} = 3 \times 10^{-5}$/s, $\Delta t = 10$ s). The gray background curve indicates a Gaussian distribution with standard deviation $s = 8 \times 10^{-4}$. (b) Excess kurtosis $\tilde{\kappa} = k - 3$ for a range of ϕ for $\dot{\gamma} = 3 \times 10^{-5}$/s at $\Delta t = 10$ s (blue crosses), and $\dot{\gamma} = 3 \times 10^{-4}$/s at $\Delta t = 1$ s (red pluses) and $\Delta t = 10$ s (red crosses).

Velocity distribution. We can also capture this localized behavior in the distribution of velocities if the system, i.e., the PDFs of $\Delta\tilde{x}$ and $\Delta\tilde{y}$, where we calculate the distribution for all particles i and times t. We show the PDFs of $\rho(\Delta\tilde{x})$ for $\phi = 0.85$, 1.0 and $\phi = 1.5$ for $\Delta t = 10$ s in Fig. 4.23(a); the PDFs for $\Delta\tilde{y}$ are completely equivalent. As before, $\Delta t = 10$ s is large enough to limit the impact of tracking errors, but small enough to clearly show the differences between the distributions.

For $\phi = 0.85$, the distribution is approximately Gaussian, except for a peak at $\Delta x = 0$, an artifact of the tracking algorithm. For higher ϕ, fatter tails appear. In other words, most particles move at a 'typical' velocity for low ϕ, while there is a much larger spread for high ϕ. We quantify this trend by calculating the kurtosis

$$\kappa = \frac{\langle |\Delta\vec{\tilde{r}}|^4 \rangle}{\langle |\Delta\vec{\tilde{r}}|^2 \rangle^2}, \tag{4.28}$$

where the average is now taken over both particles and time. For a purely Gaussian distribution, $\kappa = 3$. We therefore plot the *excess kurtosis* $\tilde{\kappa} = \kappa - 3$

as a function of ϕ in Fig. 4.23(b), and show results for $\dot{\gamma} = 3 \times 10^{-5}$/s at $\Delta t = 10$ s and 3×10^{-4}/s at $\Delta t = 1$ s and 10 s. For the $\dot{\gamma} = 3 \times 10^{-4}$/s system, $\Delta t = 1$ s is sufficient to be unaffected by tracking noise, and has the same γ interval as as the $\dot{\gamma} = 3 \times 10^{-5}$/s system at $\Delta t = 10$ s. However, we have seen that the structural relaxation time is largely independent of $\dot{\gamma}$, and we therefore also show results for $\Delta t = 10$ s

For $\dot{\gamma} = 3 \times 10^{-5}$/s, we observe $\tilde{\kappa}$ varies over four decades, with an exponential increase for $\phi < 1$, before flattening out to $\tilde{\kappa} \approx 100$. For $\dot{\gamma} = 3 \times 10^{-4}$/s, we find qualitatively the same behavior, but we note that at low ϕ, $\tilde{\kappa}$ is higher than for $\dot{\gamma} = 3 \times 10^{-5}$/s, irrespective of Δt.

Conclusion. Using particle tracking data, we have shown qualitative trends with ϕ: First, we observe caging behavior for high ϕ systems, and this behavior smoothly changes into smooth behavior at low ϕ. Second, we have observed the mean squared displacement is larger for higher ϕ at the same Δt, but find no convincing signal of caging. Finally, we investigated localization, and found clear trends with ϕ in the inverse participation ratio Λ, as well as in the kurtosis κ of the distribution of velocities. The effect of $\dot{\gamma}$ on these measures is not clear yet, and is subject for further research.

4.5 Discussion and conclusion

In this chapter, we performed bi-axial pure shear measurements on a monolayer of foam bubbles. We have introduced our setup and measurement protocol, and have shown that we can describe the observed behavior using several quantities: the image variance $\langle \Delta I^2 \rangle (t, \Delta t)$, the image variance fit parameters $A(t)$ and $\beta(t)$ and finally using the tracked particle positions.

Using these quantities, we first quantified the viscous time scale under sinusoidal shear, where we find a characteristic timescale $\tau \sim 1/\omega_0 = 7$ s at $\phi = 0.86$ and typical deformation scales. We then used a step shear deformation to quantify the structural relaxation time τ^*_{SR}, and measured its dependence on ϕ. We found that τ^*_{SR} decreases with ϕ, from ≈ 50 s for $\phi = 0.85$ to $\tau^*_{\mathrm{SR}} \approx 7$ s at $\phi = 1.3$, comparable to the viscous relaxation time scale.

We then investigated trends in foams under steady shear. First, we determined the autocorrelation time τ^*_{AC}, which decreases from $\tau^*_{\mathrm{AC}} \approx 500$ s at low ϕ to $\tau^*_{\mathrm{AC}} \approx 50$ s at high ϕ. We note that this time scale is much longer

than both the structural relaxation timescale and the viscous timescale, hence at these shear rates, we are close to quasi-static

Finally, we indicate several qualitative trends. First, we find that the distributions of the fit parameters of $\langle \Delta I^2 \rangle(t, \Delta t)$, $A(t)$ and $\beta(t)$, show a clear transition from smooth but nonaffine motion at low ϕ to affine with interspersed rearrangements at high ϕ. We find the same trends in the inverse participation ratio Λ and the kurtosis of the distribution of velocities $\rho(\Delta\tilde{x})$.

Overall, we have shown that we observe a clear transition from global, smooth, nonaffine behavior at low ϕ to local, intermittent behavior at high ϕ. We observe this transition to be smooth — there is not a single ϕ at which we suddenly switch from one behavior to the other. Instead, we find a mix of behaviors, which is best evidenced by Figs. 4.8(b) and 4.20.

We suggest several direction for future research. First, the dependence of the nature of rearrangements on the shear rate remains relatively unexplored. Our trends suggest the behavior is largely unaffected by the strain rate, which suggests that we have well separated the intrinsic relaxation time and the straining time scale. In contrast, Woldhuis et al. [38] find that the shear rate can play a similar role as the density, and the behavior is governed by $\Delta\phi^\beta/\dot{\gamma}$, with $\beta \approx 1.1 \ldots 1.3$. It remains to be seen whether this regime can be reached, as the shear rates in this system are limited by the viscous drag with the top plate.

Second, information on the forces between bubbles would help to uncover many of the microscopic details of the system. Eric Weeks' group at Emory University has invested a considerable amount of effort into measuring these details in oil-water emulsions [60, 62–64, 145, 146]. As both the physics and the imaging in these emulsions are comparable to those in foams, we propose these same methods should transfer to our system.

Appendix

4.A Reversibility

In this section, we focus on measuring reversibility under cyclic step shear. First, we step forwards to $\gamma = \gamma_{\max}$ in four $\gamma_{\max}/4$ steps. For each step, we shear forwards at a rate $\dot{\gamma} = 10^{-3}/\mathrm{s}$, and we relax the system for 300 s after each step. After performing four steps forward, we step backwards in the

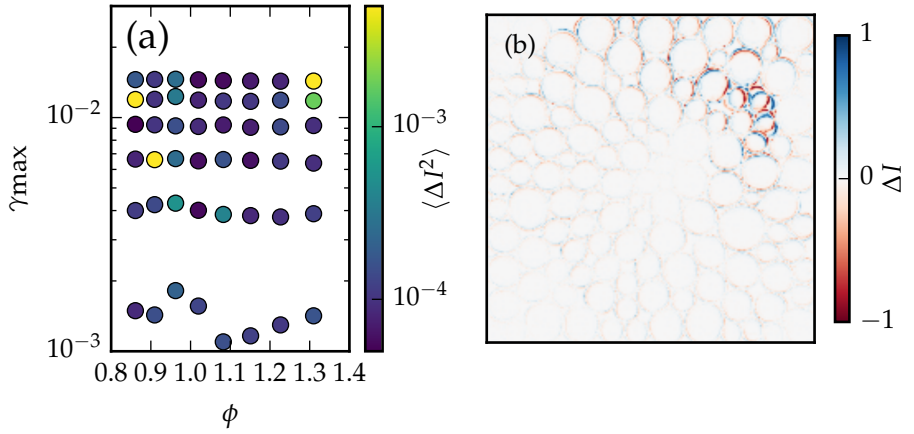

FIGURE 4.24: (a) $\langle \Delta I^2 \rangle$ between initial and final state, for a range of pressures and deformations γ. We expect a trend where larger γ and smaller ϕ correspond to larger $\langle \Delta I^2 \rangle$, but the measure is dominated by localized rearrangements. (b) An example of a localized rearrangement: $\phi = 0.91$, $\gamma = 6.6 \times 10^{-3}$, $\langle \Delta I^2 \rangle = 8.9 \times 10^{-3}$.

same way, until we return at $\gamma = 0$. We then compare the final state to the initial state, and determine the variance $\langle \Delta I^2 \rangle$.

We show this measure for a range of ϕ and γ_{max} in Fig. 4.24(a). We observe no clear relationship for either, as the signal is dominated by localized events.

SUMMARY

Foams are all around us: from personal care (shaving foam) to food (whipped cream) to building materials (polyurethane foam). At the same time, their behavior is poorly understood: how is it possible that whipped cream can act both as a solid, on top of a pie, and as a liquid, when extruded from a piping bag? The key to understanding this lies in the structure of the foam. A foam is not a homogeneous material, but consists of a large number of small air bubbles. The whole is more than the sum of its parts: even though the behavior of a single bubble is easy to understand, their collective behavior is much more complicated and completely different. The reason for this is that a deformation of the whole is only reflected partially in the deformation of individual bubbles. Instead, a large part of the deformation is reflected in a change in the *structure* of the foam. In this thesis, we investigate this change in structure.

In the first part of this thesis, we use a simple microscopic computer model to simulate the response of a foam when it is deformed by a tiny amount. Initially, the response is elastic, and the foam relaxes back to its original shape when released. We measure how far we need to deform the foam until it is irreversibly deformed. In the second part of this thesis, we focus on an experiment, where we measure the response of a two-dimensional foam when it is deformed at the edges. We observe that the response of bubbles in the center of the foam qualitatively depends on how densely the bubbles are packed together.

In chapter 2, we numerically investigate the first change in the structure formed by the bubbles. We describe the structure using the so-called *contact network*: the list of all bubbles that touch each other. Earlier work has shown that the elastic response of a foam is mainly determined by this contact network, which implies that a change in this network results in a change in the elastic response. We measure how far we need to deform the foam until two bubbles lose contact, or two bubbles are brought into contact. We observe that the process of making and breaking contacts depends strongly on how densely the bubbles are packed together: we need to deform the

foam further if the bubbles are more densely packed together. We also observe that the number of bubbles in the foam matters: in a larger foam, it is more likely that a single contact change occurs *somewhere* in the system. At the same time, the effect of a single contact change decreases with size, allowing the overall response to stay well-defined.

In chapter 3, we extend this work to larger deformations, and ask when and how systems become irreversibly deformed. First, we check for sudden changes in the location of particles: discontinuous jumps are often a sign of an irreversible process. Second, we observe what happens when we deform the system back to its initial shape. Do particles follow the same path back, or do they move to a different location? Finally, we measure what happens when the foam is allowed to relax. Do the bubbles move back to their initial position, or does the system stay deformed? Although we have not been able to answer all questions in this chapter, we have laid the ground work for further research.

Finally, in chapter 4, we describe an experiment in which a two-dimensional foam is trapped between four walls. By moving these walls, we first tune how densely the bubbles are packed together. Then, by independently moving the different walls, we deform the foam without changing the surface area. We then ask how bubbles in the center of the foam respond to this deformation at the edges. At low densities, all bubbles in the system participate, and move smoothly. This changes at high densities: there, the bubble motion becomes localized and intermittent. We characterize the behavior of the foam in various ways. First, we measure the relaxation time: how quickly is a sudden deformation transmitted through the system? The denser the bubbles are packed together, the faster the deformation is transmitted. Second, we measure the behavior when we *smoothly* deform the system, and measure a continuous change from smooth to intermittent behavior. Finally, we identify the potential of tracking individual particles, where we again identify this transition. In each of these properties, we find a strong dependence on packing density. In each case, we find two qualitatively different regimes, with mixed behavior in between. This shows foams cannot be modeled as just bubbles or just straight soap films: those are approximations that only work well in the low and high density limits, respectively.

SAMENVATTING

Schuim is overal: van persoonlijke verzorging (scheerschuim) tot voedsel (slagroom) tot bouwmaterialen (purschuim). Toch is het gedrag van deze materialen slecht begrepen. Waarom kan slagroom zowel stil boven op een taart liggen, als ware het een vaste stof, als uit een slagroomspuit stromen, als ware het een vloeistof? De clou zit hem in de opbouw van schuim. Een schuim is geen homogene stof, maar een samenvoeging van een groot aantal kleine luchtbellen. Het geheel is meer dan de som der delen: elke losse bel gedraagt zich simpel, maar het collectieve gedrag is complex en compleet anders. Een vervorming van het geheel uit zich namelijk maar deels in vervorming van de individuele *bellen*. Een groot deel van de vervorming uit zich in een verandering van de *structuur* die de bellen samen vormen. Het is die structuurverandering die in dit proefschrift onderzocht is.

We maken eerst gebruik van een simpel microscopisch computermodel, en simuleren daarmee wat er gebeurt als we een schuim een klein beetje vervormen. Hierbij meten we hoe lang een schuim elastisch blijft en terugveert, en hoe ver we het schuim moeten vervormen voordat de vervorming onomkeerbaar wordt. Vervolgens meten we in een experiment wat er gebeurt als een twee-dimensionaal schuim aan de randen wordt vervormd, en zien dat het gedrag van de bellen aan de binnenkant van het schuim sterk afhangt van hoe stevig de bellen zijn samengepakt.

In hoofdstuk 2 kijken we naar de eerste verandering van de structuur die door de bellen gevormd wordt. Die structuur beschrijven we met het zogenaamde *netwerk van contacten*: de lijst van alle bellen die elkaar raken. Uit eerder onderzoek is namelijk bekend dat het elastische gedrag van het systeem voornamelijk bepaald wordt door dit netwerk. We bekijken hoe ver we het systeem moeten vervormen tot twee bellen het contact verliezen of met elkaar in contact komen. We zien daarbij dat het proces van het maken of verbreken van contacten samenhangt met hoe sterk de bellen zijn samengedrukt: het systeem moet verder vervormd worden als de bellen sterker op elkaar worden gedrukt. We zien dat ook het aantal bellen in het

schuim uitmaakt: als het systeem groter is dan zal het eerder voorkomen dat *ergens* in het systeem twee bellen een contact verliezen of maken. Het elastische gedrag verandert daardoor eerder in grotere systemen, maar tegelijkertijd wordt het effect van een enkele contactverandering kleiner. Hierdoor blijft het gedrag van het schuim goed gedefiniëerd.

In hoofdstuk 3 kijken we naar iets grotere vervormingen, en kijken daarbij naar wanneer en op welke manier een systeem onomkeerbaar wordt vervormd. Allereerst meten we of er abrupte sprongen zijn in de posities van deeltjes: zo'n sprong is vaak een teken van een onomkeerbaar proces. Ten tweede kijken we wat er gebeurt als we het systeem een stukje terug bewegen: volgen de deeltjes dan exact hetzelfde pad terug? Als laatste kijken we wat er gebeurt als we het systeem laten terugveren. Beweegt het systeem dan terug naar de starttoestand, of blijft het systeem vervormd? We hebben deze vragen nog niet volledig kunnen beantwoorden, maar we hebben wel de fundamenten gelegd voor vervolgonderzoek.

In hoofdstuk 4 beschrijven we een experiment waarbij we een tweedimensionale laag schuimbellen opsluiten tussen vier wanden. Door deze wanden te verplaatsen kunnen we allereerst de bellen meer of minder tegen elkaar aandrukken. Vervolgens kunnen we, met een slimme beweging van de wanden, het schuim vervormen zónder de oppervlakte te veranderen. De vraag is vervolgens hoe de bellen aan de *binnenkant* van het systeem op deze vervorming aan de rand reageren. We hebben het gedrag op een aantal manieren in kaart gebracht. Allereerst kijken we naar de relaxatietijd: hoe snel wordt een abrupte beweging door het hele systeem doorgegeven? Hoe sterker de bellen op elkaar gedrukt worden, hoe sneller dit gaat. Vervolgens meten we het gedrag van het schuim bij een voortdurende vervorming, waarbij we een langzame overgang tussen soepel en abrupt gedrag vinden. Als laatste bekijken we de mogelijkheden van het automatisch volgen van deeltjes (*particle tracking*), waarbij we wederom deze overgang zien. We zien dus dat elke eigenschap sterk afhangt van de dichtheid, waarbij het gedrag bij lage dichtheden soepel is, maar bij hoge dichtheden abrupt en lokaal wordt. Bovendien is er altijd sprake van een gemengd regime, wat laat zien dat schuim niet gemodelleerd kan worden met alleen ronde bellen of alleen rechte zeepvliezen: dat zijn benaderingen die alleen in de limit van zeer lage respectievelijk zeer hoge dichtheden goed werken.

PUBLICATION LIST

ON WORK PRESENTED IN THIS THESIS:

(i) Merlijn S. van Deen, Johannes Simon, Zorana Zeravcic, Simon Dagois-Bohy, Brian P. Tighe, and Martin van Hecke. *Contact Changes near jamming*. Phys. Rev. E **90**, 020202 (2014). doi:10.1103/PhysRevE.90.020202

(ii) Merlijn S. van Deen, Brian P. Tighe, and Martin van Hecke. *Contact Changes of Sheared Systems: Scaling, Correlations, and Mechanisms*. Submitted to Phys. Rev. E., arXiv:1606.04799

(iii) Merlijn S. van Deen, Sven Wijtmans, M. Lisa Manning, and Martin van Hecke. *Rearrangements in Sheared Disordered Solids*. In preparation.

(iv) Merlijn S. van Deen, Alexander O.N. Siemens, and Martin van Hecke. *Rearrangements in Wet and Dry foams*. In preparation.

ON OTHER WORK

(v) Erik Woldhuis, Vijayakumar Chikkadi, Merlijn S. van Deen, Peter Schall and Martin van Hecke. *Fluctuations in flows near jamming*, Soft Matter **11**, 7024 (2015). doi:10.1039/c5sm01592h

(vi) Merlijn S. van Deen, Thibault Bertrand, Nhung Vu, David Quéré, Eric Clément, and Anke Lindner. *Particles accelerate the detachment of viscous liquids*, Rheologica Acta **52**, 403 (2013). doi:10.1007/s00397-013-0691-9

PUBLISHED SOFTWARE AND DATA SETS
Authors listed in alphabetical order

(vii) Simon Dagois-Bohy, Johannes Simon, Merlijn S. van Deen, and Zorana Zeravcic.
JamBashBulk: two-dimensional packing simulation.
Zenodo. doi:10.5281/zenodo.60972

(viii) Merlijn S. van Deen.
Data analysis code for *JamBashBulk* packings.
Zenodo. doi:10.5281/zenodo.60687

(ix) Simon Dagois-Bohy, Silke Henkes, Johannes Simon, Brian P. Tighe, Merlijn S. van Deen, Martin van Hecke, and Zorana Zeravcic.
Shear-stabilized jammed packings.
Zenodo. doi:10.5281/zenodo.59216

(x) Simon Dagois-Bohy, Silke Henkes, Johannes Simon, Brian P. Tighe, Merlijn S. van Deen, Martin van Hecke, and Zorana Zeravcic.
Sheared shear-stabilized jammed packings.
Zenodo. doi:10.5281/zenodo.59217

SUPPLEMENTAL MATERIAL TO THIS THESIS

(xi) Merlijn S. van Deen.
Mechanical Response of Foams: Elasticity, Plasticity, and Rearrangements (Supplemental material).
Zenodo. doi:10.5281/zenodo.57013

(xii) Merlijn S. van Deen.
Mechanical Response of Foams: Elasticity, Plasticity, and Rearrangements (Data analysis notebooks).
Zenodo. doi:10.5281/zenodo.60684

Curriculum vitae

I was born on November 22nd, 1988 in The Hague. I grew up in the same city, and followed my secondary education at the *Gymnasium Haganum*. In 2006, I obtained my vwo degree and started my undergraduate studies in both Physics and Astronomy at Leiden University. During that time, I spent a year organizing science shows for high schools, as board member for Stichting Rino. In 2010, after a research project in the Quantum Optics group on *Spatial Heterodyne Spectroscopy*, I obtained both BSc diplomas.

After finishing both BScs, I started on an MSc in Experimental Physics, also at Leiden University. For this degree, I worked on two research projects: *Measurements on 2D Force Networks* in the Complex Media and Metamaterials (CMM) research group at Leiden University, and *Experiments on the droplet detachment of suspensions* in the PMMH group at the ESPCI (Paris, France). I received my degree *cum laude* in 2012, and started my PhD in the CMM group shortly thereafter.

Under supervision of Prof. dr. M.L. van Hecke, I researched the mechanical response of foams, in both simulations and experiments. The results of these four years have been collected in this thesis. Part of this work was performed in close collaboration with dr. M.L. Manning and S. Wijtmans at Syracuse University (United States).

During my PhD, I was a Teaching Assistant for the undergraduate courses *Diffusion*, *Fourier Physics* and *Introduction to Python*. I attended schools in Orsay, Les Houches and Montpellier (France), Enschede (The Netherlands), and Easton, MA (United States), and presented work at conferences in Thessaloniki (Greece), Ruthin (Wales), Nantes (France), Baltimore, Denver and San Antonio (United States).

In September 2016, I started as Advisor in New Technologies at UL's Transaction Security division in Leiden.

Acknowledgments

This thesis is the result of four years of research at the Huygens-Kamerlingh Onnes Lab in Leiden. Even though only my name is on the cover, science is a group effort, and I would never have been able to reach this result without the help of many people around me.

Martin, thank you, for your inspiration, enthousiasm and practical support over the years. Jeroen, your continued technical support – often when I had broken something – has been invaluable. Without you, the Bi-ax would never have been as good as it is. Daniëlle, thank you for all your help in keeping track of all the forms, especially in the last months. Sven and Lisa, our collaborators from Syracuse: thank you. Without you, we would never have understood rearrangements as well as we do now.

Thanks to my colleagues in Leiden and Amsterdam with whom I discussed my work and who inspired me: Anne, Casper, Corentin, Daniela, Elie, Erik, Kiri, Luuk, Nitin, Vera, Vera, Scott, Siet and Tomek. In particular, I want to thank Alex, Brian and Simon, who were indispensable in getting my projects off the ground. My office mates Geert, Bastiaan and Peter, thank you for your jokes, debates and for thinking along. Bastiaan, thank you in particular for helping me maintain sight of the bigger picture.

I wish to express my gratitude for the support from family, in particular my parents, Hansje and Jurjen, and my sister Welmoed. Friends, in particular Anton, Steven, and Elbert, thank you for the enlightening discussions. Finally, Annelies, thank you, for making life so much more fun!

BIBLIOGRAPHY

[1] (a) *xlibber*. *Ultimate Sand Castle*. CC-BY (2010). https://www.flickr.com/photos/56844661@N00/4846203074; (b) Michal Osmenda. *"My Way"*. CC-BY-SA (2009). http://www.flickr.com/photos/michalo/3363960580/; (c) Tim Pierce. *Time and again*. CC-BY (2014). https://www.flickr.com/photos/qwrrty/14957272659/.

[2] A. J. Liu and S. R. Nagel. *The Jamming Transition and the Marginally Jammed Solid*. Annu. Rev. Condens. Matter Phys. **1**, 347 (2010). doi:10.1146/annurev-conmatphys-070909-104045.

[3] M. van Hecke. *Jamming of soft particles: geometry, mechanics, scaling and isostaticity*. J. Phys.: Condens. Matter **22**, 033 101 (2010). doi:10.1088/0953-8984/22/3/033101.

[4] M. L. Falk and J. Langer. *Deformation and Failure of Amorphous, Solidlike Materials*. Annu. Rev. Condens. Matter Phys. **2**, 353 (2011). doi:10.1146/annurev-conmatphys-062910-140452.

[5] D. Bi, S. Henkes, K. E. Daniels, and B. Chakraborty. *The Statistical Physics of Athermal Materials*. Annu. Rev. Condens. Matter Phys. **6**, 63 (2015). doi:10.1146/annurev-conmatphys-031214-014336.

[6] (a) *jeffreyw*. *Mmm... Apple Crisp with Whipped Cream*. CC-BY (2011). https://www.flickr.com/photos/jeffreyww/6220715962/; (b) Rob Bogaerts / Anefo. *Staatssecretaris Albert-Jan Evenhuis opent Nebato Tech in Utrecht door gebakjes met slagroom te bespuiten*. CC-BY (1987). hdl:10648/ad5ed534-d0b4-102d-bcf8-003048976d84.

[7] A. J. Liu and S. R. Nagel. *Nonlinear dynamics: Jamming is not just cool any more*. Nature **396**, 21 (1998). doi:10.1038/23819.

[8] A. Liu, S. Nagel, W. Van Saarloos, and M. Wyart. *Dynamical Heterogeneities in Glasses, Colloids, and Granular Media*, chapter The jamming scenario-an introduction and outlook. Oxford University Press (2010). ISBN: 9780199691470. doi:10.1093/acprof:oso/9780199691470.003.0009.

[9] D. J. Hornbaker, R. Albert, I. Albert, A.-L. Barabási, and P. Schiffer. *What keeps sandcastles standing?* Nature **387**, 765 (1997). doi:10.1038/42831.

[10] A.-L. Barabási, R. Albert, and P. Schiffer. *The physics of sand castles: maximum angle of stability in wet and dry granular media*. Phys. A **266**, 366 (1999). doi:10.1016/s0378-4371(98)00618-9.

[11] H. Princen. *Rheology of foams and highly concentrated emulsions I: Elastic Properties and Yield Stress of a Cylindrical Model System*. J. Colloid Interface Sci. **91**, 160 (1983). doi:10.1016/0021-9797(83)90323-5.

[12] R. Höhler and S. Cohen-Addad. *Rheology of liquid foam*. J. Phys.: Condens. Matter **17**, R1041 (2005). doi:10.1088/0953-8984/17/41/R01.

[13] C. S. O'Hern, S. A. Langer, A. J. Liu, and S. R. Nagel. *Random Packings of Frictionless Particles*. Phys. Rev. Lett. **88**, 075 507 (2002). doi:10.1103/PhysRevLett.88.075507.

[14] S. van den Wildenberg, R. van Loo, and M. van Hecke. *Shock Waves in Weakly Compressed Granular Media*. Phys. Rev. Lett. **111**, 218 003 (2013). doi:10.1103/PhysRevLett.111.218003.

[15] G. Combe, V. Richefeu, M. Stasiak, and A. P. F. Atman. *Experimental Validation of a Nonextensive Scaling Law in Confined Granular Media*. Phys. Rev. Lett. **115**, 238 301 (2015). doi:10.1103/PhysRevLett.115.238301.

[16] C. Coulais, R. Behringer, and O. Dauchot. *How the ideal Jamming point illuminates the world of granular media*. Soft Matter **10**, 1519 (2013). doi:10.1039/c3sm51231b.

[17] C. S. Campbell. *Granular material flows – An overview*. Powder Technol. **162**, 208 (2006). doi:10.1016/j.powtec.2005.12.008.

[18] A. Siemens and M. Van Hecke. *Jamming: A simple introduction*. Phys. A **389**, 4255 (2010). doi:10.1016/j.physa.2010.02.027.

[19] J. Dijksman, G. Wortel, L. van Dellen, O. Dauchot, and M. van Hecke. *Jamming, Yielding, and Rheology of Weakly Vibrated Granular Media*. Phys. Rev. Lett. **107**, 108 303 (2011). doi:10.1103/PhysRevLett.107.108303.

[20] N. C. Keim and P. E. Arratia. *Yielding and microstructure in a 2D jammed material under shear deformation*. Soft Matter **9**, 6222 (2013). doi:10.1039/c3sm51014j.

[21] C. S. O'Hern, L. E. Silbert, A. J. Liu, and S. R. Nagel. *Jamming at zero temperature and zero applied stress: The epitome of disorder*. Phys. Rev. E **68**, 011 306 (2003). doi:10.1103/PhysRevE.68.011306.

[22] D. J. Durian. *Foam Mechanics at the Bubble Scale*. Phys. Rev. Lett. **75**, 4780 (1995). doi:10.1103/PhysRevLett.75.4780.

[23] D. J. Durian. *Bubble-scale model of foam mechanics: Melting, nonlinear behavior, and avalanches*. Phys. Rev. E **55**, 1739 (1997). doi:10.1103/PhysRevE.55.1739.

[24] B. P. Tighe. *Relaxations and Rheology near Jamming*. Phys. Rev. Lett. **107**, 158 303 (2011). doi:10.1103/PhysRevLett.107.158303.

[25] P. Olsson and S. Teitel. *Herschel-Bulkley Shearing Rheology Near the Athermal Jamming Transition*. Phys. Rev. Lett. **109**, 108 001 (2012). doi:10.1103/PhysRevLett.109.108001.

[26] G. Katgert and M. van Hecke. *Jamming and geometry of two-dimensional foams*. Europhys. Lett. **92**, 34 002 (2010). doi:10.1209/0295-5075/92/34002.

[27] C. P. Goodrich, W. G. Ellenbroek, and A. J. Liu. *Stability of jammed packings I: the rigidity length scale*. Soft Matter **9**, 10 993 (2013). doi:10.1039/c3sm51095f.

[28] C. P. Goodrich, S. Dagois-Bohy, B. P. Tighe, M. van Hecke, A. J. Liu, and S. R. Nagel. *Jamming in finite systems: Stability, anisotropy, fluctuations, and scaling*. Phys. Rev. E **90**, 022 138 (2014). doi:10.1103/PhysRevE.90.022138.

[29] T. Bertrand, R. P. Behringer, B. Chakraborty, C. S. O'Hern, and M. D. Shattuck. *Protocol dependence of the jamming transition*. Phys. Rev. E **93**, 012 901 (2016). doi:10.1103/PhysRevE.93.012901.

[30] W. G. Ellenbroek, E. Somfai, M. van Hecke, and W. van Saarloos. *Critical Scaling in Linear Response of Frictionless Granular Packings near Jamming*. Phys. Rev. Lett. **97**, 258 001 (2006). doi:10.1103/PhysRevLett.97.258001.

[31] W. G. Ellenbroek, M. van Hecke, and W. van Saarloos. *Jammed frictionless disks: Connecting local and global response*. Phys. Rev. E **80**, 061 307 (2009). doi:10.1103/PhysRevE.80.061307.

[32] W. G. Ellenbroek, Z. Zeravcic, W. van Saarloos, and M. van Hecke. *Non-affine response: Jammed packings vs. spring networks*. Europhys. Lett. **87**, 34 004 (2009). doi:10.1209/0295-5075/87/34004.

[33] C. P. Goodrich, A. J. Liu, and S. R. Nagel. *Finite-Size Scaling at the Jamming Transition*. Phys. Rev. Lett. **109**, 095 704 (2012). doi:10.1103/PhysRevLett.109.095704.

[34] S. Dagois-Bohy, B. P. Tighe, J. Simon, S. Henkes, and M. van Hecke. *Soft-Sphere Packings at Finite Pressure but Unstable to Shear*. Phys. Rev. Lett. **109**, 095 703 (2012). doi:10.1103/PhysRevLett.109.095703.

[35] M. Lundberg, K. Krishan, N. Xu, C. S. O'Hern, and M. Dennin. *Reversible plastic events in amorphous materials*. Phys. Rev. E **77**, 041 505 (2008). doi:10.1103/PhysRevE.77.041505.

[36] S. Sandfeld, Z. Budrikis, S. Zapperi, and D. F. Castellanos. *Avalanches, loading and finite size effects in 2D amorphous plasticity: results from a finite element model*. J. Stat. Mech. Theor. Exp. **2015**, P02 011 (2015). doi:10.1088/1742-5468/2015/02/p02011.

[37] F. Varnik, S. Mandal, V. Chikkadi, D. Denisov, P. Olsson, D. Vågberg, D. Raabe, and P. Schall. *Correlations of plasticity in sheared glasses*. Phys. Rev. E **89**, 040 301 (2014). doi:10.1103/PhysRevE.89.040301.

[38] E. Woldhuis, V. Chikkadi, M. S. van Deen, P. Schall, and M. van Hecke. *Fluctuations in flows near jamming*. Soft Matter **11**, 7024 (2015). doi:10.1039/c5sm01592h.

[39] G. Katgert, M. Möbius, and M. van Hecke. *Rate Dependence and Role of Disorder in Linearly Sheared Two-Dimensional Foams*. Phys. Rev. Lett. **101**, 058 301 (2008). doi:10.1103/PhysRevLett.101.058301.

[40] M. E. Möbius, G. Katgert, and M. van Hecke. *Relaxation and flow in linearly sheared two-dimensional foams*. Europhys. Lett. **90**, 44 003 (2010). doi:10.1209/0295-5075/90/44003.

[41] B. P. Tighe, E. Woldhuis, J. J. C. Remmers, W. van Saarloos, and M. van Hecke. *Model for the Scaling of Stresses and Fluctuations in Flows near Jamming*. Phys. Rev. Lett. **105**, 088 303 (2010). doi:10.1103/PhysRevLett.105.088303.

[42] V. Chikkadi, E. Woldhuis, M. van Hecke, and P. Schall. *Correlations of strain and plasticity in a flowing foam*. Europhys. Lett. **112**, 36 004 (2015). doi:10.1209/0295-5075/112/36004.

[43] S. Ulam, R. D. Richtmyer, and J. von Neumann. *Statistical methods in neutron diffusion*. Technical Report LAMS–551, Los Alamos Scientific Laboratory (1947). URL `http://permalink.lanl.gov/object/tr?what=info:lanl-repo/lareport/LA-00551-MS`.

[44] N. Metropolis, A. W. Rosenbluth, M. N. Rosenbluth, A. H. Teller, and E. Teller. *Equation of State Calculations by Fast Computing Machines*. J. Chem. Phys. **21**, 1087 (1953). doi:10.1063/1.1699114.

[45] R. B. Potts and C. Domb. *Some generalized order-disorder transformations*. Math. Proc. Cambridge Philos. Soc. **48**, 106 (1952). doi:10.1017/s0305004100027419.

[46] B. J. Alder and T. E. Wainwright. *Phase Transition for a Hard Sphere System*. J. Chem. Phys. **27**, 1208 (1957). doi:10.1063/1.1743957.

[47] F. Bolton and D. Weaire. *Rigidity loss transition in a disordered 2D froth*. Phys. Rev. Lett. **65**, 3449 (1990). doi:10.1103/PhysRevLett.65.3449.

[48] H. Hertz. *Ueber die Berührung fester elastischer Körper*. J. Reine Angew. Math. **92**, 156 (1882). doi:10.1515/crll.1882.92.156.

[49] D. Miedema, C. Hamster, G. Katgert, and M. van Hecke. *Interactions between Bubbles Trapped Below Glass Plates*. In preparation.

[50] S. Hutzler, R. P. Murtagh, D. Whyte, S. T. Tobin, and D. Weaire. *Z-cone model for the energy of an ordered foam*. Soft Matter **10**, 7103 (2014). doi:10.1039/c4sm00774c.

[51] R. Murtagh, D. Whyte, D. Weaire, and S. Hutzler. *Adaptation of the Z -cone model to the estimation of the energy of a bcc foam*. Philos. Mag. **95**, 4023 (2015). doi:10.1080/14786435.2015.1111531.

[52] C. E. Maloney and A. Lemaître. *Amorphous systems in athermal, quasistatic shear*. Phys. Rev. E **74**, 016 118 (2006). doi:10.1103/PhysRevE.74.016118.

[53] C. Heussinger, P. Chaudhuri, and J.-L. Barrat. *Fluctuations and correlations during the shear flow of elastic particles near the jamming transition*. Soft Matter **6**, 3050 (2010). doi:10.1039/b927228c.

[54] A. Kabla, J. Scheibert, and G. Debregeas. *Quasi-static rheology of foams. Part 2. Continuous shear flow*. J. Fluid Mech. **587**, 45 (2007). doi:10.1017/S0022112007007276.

[55] A. Kabla and G. Debregeas. *Quasi-static rheology of foams. Part 1. Oscillating strain*. J. Fluid Mech. **587**, 23 (2007). doi:10.1017/S0022112007007264.

[56] C.-C. Kuo and M. Dennin. *Scaling of critical velocity for bubble raft fracture under tension*. J. Rheol. **56**, 527 (2012). doi:10.1122/1.3695152.

[57] M. Maiti and C. Heussinger. *Rheology near jamming: The influence of lubrication forces*. Phys. Rev. E **89**, 052 308 (2014). doi:10.1103/PhysRevE.89.052308.

[58] N. D. Denkov, S. Tcholakova, K. Golemanov, K. P. Ananthpadmanabhan, and A. Lips. *The role of surfactant type and bubble surface mobility in foam rheology*. Soft Matter **5**, 3389 (2009). doi:10.1039/b903586a.

[59] A. O. N. Siemens. *Elasticity and plasticity: foams near jamming*. Ph.D. thesis, Leiden University (2013). hdl:1887/21709.

[60] K. W. Desmond, P. J. Young, D. Chen, and E. R. Weeks. *Experimental study of forces between quasi-two-dimensional emulsion droplets near jamming*. Soft Matter **9**, 3424 (2013). doi:10.1039/c3sm27287g.

[61] K. W. Desmond and E. R. Weeks. *Influence of particle size distribution on random close packing of spheres*. Phys. Rev. E **90**, 022 204 (2014). doi:10.1103/PhysRevE.90.022204.

[62] K. W. Desmond and E. R. Weeks. *Measurement of Stress Redistribution in Flowing Emulsions*. Phys. Rev. Lett. **115**, 098 302 (2015). doi:10.1103/PhysRevLett.115.098302.

[63] D. Chen, K. W. Desmond, and E. R. Weeks. *Topological rearrangements and stress fluctuations in quasi-two-dimensional hopper flow of emulsions*. Soft Matter **8**, 10 486 (2012). doi:10.1039/c2sm26023a.

[64] D. Chen, K. W. Desmond, and E. R. Weeks. *Experimental observation of local rearrangements in dense quasi-two-dimensional emulsion flow*. Phys. Rev. E **91**, 062 306 (2015). doi:10.1103/PhysRevE.91.062306.

[65] M. S. van Deen, J. Simon, Z. Zeravcic, S. Dagois-Bohy, B. P. Tighe, and M. van Hecke. *Contact changes near jamming*. Phys. Rev. E **90**, 020 202 (2014). doi:10.1103/PhysRevE.90.020202.

[66] M. S. van Deen, B. P. Tighe, and M. van Hecke. *Contact Changes of Sheared Systems: Scaling, Correlations, and Mechanisms* (2016). Submitted to Phys. Rev. E., arXiv:1606.04799.

[67] N. C. Keim, J. D. Paulsen, and S. R. Nagel. *Multiple transient memories in sheared suspensions: Robustness, structure, and routes to plasticity*. Phys. Rev. E **88**, 032 306 (2013). doi:10.1103/PhysRevE.88.032306.

[68] A. Lemaître and C. Caroli. *Plastic response of a two-dimensional amorphous solid to quasistatic shear: Transverse particle diffusion and phenomenology of dissipative events*. Phys. Rev. E **76**, 036 104 (2007). doi:10.1103/PhysRevE.76.036104.

[69] K. M. Salerno, C. E. Maloney, and M. O. Robbins. *Avalanches in Strained Amorphous Solids: Does Inertia Destroy Critical Behavior?* Phys. Rev. Lett. **109**, 105 703 (2012). doi:10.1103/PhysRevLett.109.105703.

[70] H. G. E. Hentschel, S. Karmakar, E. Lerner, and I. Procaccia. *Size of Plastic Events in Strained Amorphous Solids at Finite Temperatures*. Phys. Rev. Lett. **104**, 025 501 (2010). doi:10.1103/PhysRevLett.104.025501.

[71] V. Chikkadi, O. Gendelman, V. Ilyin, J. Ashwin, I. Procaccia, and C. A. B. Z. Shor. *Spreading plastic failure as a mechanism for the shear modulus reduction in amorphous solids*. Europhys. Lett. **110**, 48 001 (2013). doi:10.1209/0295-5075/110/48001.

[72] P. Olsson and S. Teitel. *Critical Scaling of Shear Viscosity at the Jamming Transition*. Phys. Rev. Lett. **99**, 178 001 (2007). doi:10.1103/PhysRevLett.99.178001.

[73] M. Wyart. *Marginal Stability Constrains Force and Pair Distributions at Random Close Packing*. Phys. Rev. Lett. **109**, 125 502 (2012). doi:10.1103/PhysRevLett.109.125502.

[74] M. Wyart. *On the rigidity of amorphous solids*. Ann. Phys. Fr. **30**, 1 (2005). doi:10.1051/anphys:2006003.

[75] M. L. Manning and A. J. Liu. *Vibrational Modes Identify Soft Spots in a Sheared Disordered Packing*. Phys. Rev. Lett. **107**, 108 302 (2011). doi:10.1103/PhysRevLett.107.108302.

[76] C. F. Schreck, T. Bertrand, C. S. O'Hern, and M. D. Shattuck. *Repulsive Contact Interactions Make Jammed Particulate Systems Inherently Nonharmonic*. Phys. Rev. Lett. **107**, 078 301 (2011). doi:10.1103/PhysRevLett.107.078301.

[77] C. P. Goodrich, A. J. Liu, and S. R. Nagel. *Comment on "Repulsive Contact Interactions Make Jammed Particulate Systems Inherently Nonharmonic"*. Phys. Rev. Lett. **112**, 049 801 (2014). doi:10.1103/PhysRevLett.112.049801.

[78] C. F. Schreck, T. Bertrand, C. S. O'Hern, and M. D. Shattuck. *Response to Comment on 'Repulsive contact interactions make jammed particulate systems inherently nonharmonic'* (2013). arXiv:1306.1961.

[79] G. Combe and J.-N. Roux. *Strain versus Stress in a Model Granular Material: A Devil's Staircase*. Phys. Rev. Lett. **85**, 3628 (2000). doi:10.1103/PhysRevLett.85.3628.

[80] E. Lerner, G. Düring, and M. Wyart. *Low-energy non-linear excitations in sphere packings*. Soft Matter **9**, 8252 (2013). doi:10.1039/c3sm50515d.

[81] A. Donev, S. Torquato, F. H. Stillinger, and R. Connelly. *Comment on "Jamming at zero temperature and zero applied stress: The epitome of disorder"*. Phys. Rev. E **70**, 043 301 (2004). doi:10.1103/PhysRevE.70.043301.

[82] A. Donev. *Jammed packings of hard particles*. Ph.D. thesis, Princeton University (2006). URL `http://cims.nyu.edu/~donev/Thesis.pdf`.

[137] D. J. Koeze, D. Vågberg, B. B. T. Tjoa, and B. P. Tighe. *Mapping the jamming transition of bidisperse mixtures*. Europhys. Lett. **113**, 54 001 (2016). doi:10.1209/0295-5075/113/54001.

[83] J. Simon. *Rearrangements in Jammed Two-Dimensional Packings of Spherical Particles*. Master's thesis, Leiden University (2012).

[84] M. Born and K. Huang. *Dynamical Theory of Crystal Lattices*. Clarendon Press (1998). ISBN: 0198503695.

[85] J. Shewchuk. *An introduction to the conjugate gradient method without the agonizing pain*. Technical report, School of Computer Science, Carnegie Mellon University, Pittsburgh, PA (1994). URL `https://www.cs.cmu.edu/~jrs/jrspapers.html`.

[86] E. Bitzek, P. Koskinen, F. Gähler, M. Moseler, and P. Gumbsch. *Structural Relaxation Made Simple*. Phys. Rev. Lett. **97**, 170 201 (2006). doi:10.1103/PhysRevLett.97.170201.

[87] J. D. Paulsen, N. C. Keim, and S. R. Nagel. *Multiple Transient Memories in Experiments on Sheared Non-Brownian Suspensions*. Phys. Rev. Lett. **113**, 068 301 (2014). doi:10.1103/PhysRevLett.113.068301.

[88] C. Croarkin and P. Tobias, editors. *e-Handbook of Statistical Methods*. NIST/SEMATECH (2014). URL `http://www.itl.nist.gov/div898/handbook/`.

[89] W. Weibull. *A Statistical Distribution Function of Wide Applicability*. J. Appl. Mech. **13**, 293 (1951).

[90] S. Dagois-Bohy. *Calculation of the Hessian*. Technical report, Leiden Institute of Physics (2013).

[91] G. Strang. *Introduction to Linear Algebra*. Wellesley Cambridge Press, 4th edition (2009). ISBN: 0980232716.

[92] J. A. Rice. *Mathematical Statistics and Data Analysis*. Brooks/Cole, 3rd edition (2006). ISBN: 0495110892.

[93] C. P. Goodrich, A. J. Liu, and S. R. Nagel. *Contact nonlinearities and linear response in jammed particulate packings*. Phys. Rev. E **90**, 022 201 (2014). doi:10.1103/PhysRevE.90.022201.

[94] M. Wyart, L. Silbert, S. R. Nagel, and T. Witten. *Effects of compression on the vibrational modes of marginally jammed solids*. Phys. Rev. E **72**, 051 306 (2005). doi:10.1103/PhysRevE.72.051306.

[95] C. P. Goodrich, A. J. Liu, and S. R. Nagel. *The Principle of Independent Bond-Level Response: Tuning by Pruning to Exploit Disorder for Global Behavior*. Phys. Rev. Lett. **114**, 225 501 (2015). doi:10.1103/PhysRevLett.114.225501.

[96] S. Dagois-Bohy, E. Somfai, B. P. Tighe, and M. van Hecke. *Oscillatory Rheology near Jamming*. In preparation.

[97] J. Boschan, D. Vågberg, E. Somfai, and B. P. Tighe. *Beyond linear elasticity: jammed solids at finite shear strain and rate*. Soft Matter **12**, 5450 (2016). doi:10.1039/c6sm00536e.

[98] C. S. O'Hern and Q. Wu. Private communication.

[99] M. Wyart. Private communication.

[100] C. Moukarzel. *Isostatic Phase Transition and Instability in Stiff Granular Materials*. Phys. Rev. Lett. **81**, 1634 (1998). doi:10.1103/PhysRevLett.81.1634.

[101] J.-N. Roux. *Geometric origin of mechanical properties of granular materials*. Phys. Rev. E **61**, 6802 (2000). doi:10.1103/PhysRevE.61.6802.

[102] M. F. Thorpe. *Elastic moduli of two-dimensional composite continua with elliptical inclusions*. J. Acoust. Soc. Am. **77**, 1674 (1985). doi:10.1121/1.391966.

[103] E. Lerner, G. Düring, and M. Wyart. *Toward a microscopic description of flow near the jamming threshold*. Europhys. Lett. **99**, 58 003 (2012). doi:10.1209/0295-5075/99/58003.

[104] M. S. van Deen, S. Wijtmans, M. L. Manning, and M. van Hecke. *Rearrangements in Sheared Disordered Solids*. In preparation.

[105] K. M. Salerno and M. O. Robbins. *Effect of inertia on sheared disordered solids: Critical scaling of avalanches in two and three dimensions*. Phys. Rev. E **88**, 062 206 (2013). doi:10.1103/PhysRevE.88.062206.

[106] Y. Shi, M. B. Katz, H. Li, and M. L. Falk. *Evaluation of the Disorder Temperature and Free-Volume Formalisms via Simulations of Shear Banding in Amorphous Solids*. Phys. Rev. Lett. **98**, 185 505 (2007). doi:10.1103/PhysRevLett.98.185505.

[107] M. L. Manning, J. S. Langer, and J. M. Carlson. *Strain localization in a shear transformation zone model for amorphous solids*. Phys. Rev. E **76**, 056 106 (2007). doi:10.1103/PhysRevE.76.056106.

[108] V. Chikkadi, D. M. Miedema, M. T. Dang, B. Nienhuis, and P. Schall. *Shear Banding of Colloidal Glasses: Observation of a Dynamic First-Order Transition*. Phys. Rev. Lett. **113**, 208 301 (2014). doi:10.1103/PhysRevLett.113.208301.

[109] K. Martens, L. Bocquet, and J.-L. Barrat. *Spontaneous formation of permanent shear bands in a mesoscopic model of flowing disordered matter*. Soft Matter **8**, 4197 (2012). doi:10.1039/c2sm07090a.

[110] P. Schall and M. van Hecke. *Shear Bands in Matter with Granularity*. Annu. Rev. Fluid Mech. **42**, 67 (2010). doi:10.1146/annurev-fluid-121108-145544.

[111] M. Falk and J. Langer. *Dynamics of viscoplastic deformation in amorphous solids*. Phys. Rev. E **57**, 7192 (1998). doi:10.1103/PhysRevE.57.7192.

[112] P. Sollich. *Rheological constitutive equation for a model of soft glassy materials*. Phys. Rev. E **58**, 738 (1998). doi:10.1103/PhysRevE.58.738.

[113] P. M. Derlet and R. Maaß. *Thermal-activation model for freezing and the elastic robustness of bulk metallic glasses*. Phys. Rev. B **84**, 220 201 (2011). doi:10.1103/PhysRevB.84.220201.

[114] J.-C. Baret, D. Vandembroucq, and S. Roux. *Extremal Model for Amorphous Media Plasticity*. Phys. Rev. Lett. **89**, 195 506 (2002). doi:10.1103/PhysRevLett.89.195506.

[115] M. Müller and M. Wyart. *Marginal Stability in Structural, Spin, and Electron Glasses*. Annu. Rev. Condens. Matter Phys. **6**, 177 (2015). doi:10.1146/annurev-conmatphys-031214-014614.

[116] C. F. Schreck, R. S. Hoy, M. D. Shattuck, and C. S. O'Hern. *Particle-scale reversibility in athermal particulate media below jamming*. Phys. Rev. E **88**, 052 205 (2013). doi:10.1103/PhysRevE.88.052205.

[117] N. Xu, V. Vitelli, A. J. Liu, and S. R. Nagel. *Anharmonic and quasi-localized vibrations in jammed solids—Modes for mechanical failure*. Europhys. Lett. **90**, 56 001 (2010). doi:10.1209/0295-5075/90/56001.

[118] I. Regev, T. Lookman, and C. Reichhardt. *Onset of irreversibility and chaos in amorphous solids under periodic shear*. Phys. Rev. E **88**, 062 401 (2013). doi:10.1103/PhysRevE.88.062401.

[119] M. Tsamados, A. Tanguy, C. Goldenberg, and J.-L. Barrat. *Local elasticity map and plasticity in a model Lennard-Jones glass*. Phys. Rev. E **80**, 026 112 (2009). doi:10.1103/PhysRevE.80.026112.

[120] D. Fiocco, G. Foffi, and S. Sastry. *Encoding of Memory in Sheared Amorphous Solids*. Phys. Rev. Lett. **112**, 025 702 (2014). doi:10.1103/PhysRevLett.112.025702.

[121] N. C. Keim and P. E. Arratia. *Mechanical and Microscopic Properties of the Reversible Plastic Regime in a 2D Jammed Material*. Phys. Rev. Lett. **112**, 028 302 (2014). doi:10.1103/PhysRevLett.112.028302.

[122] M. S. van Deen, A. O. N. Siemens, and M. van Hecke. *Rearrangements in Wet and Dry foams*. In preparation.

[123] M. F. Vaz, S. Cox, and P. Teixeira. *Cyclic deformation of bidisperse two-dimensional foams*. Philos. Mag. **91**, 4345 (2011). doi:10.1080/14786435.2011.620995.

[124] S. A. Jones and S. J. Cox. *On the effectiveness of a quasistatic bubble-scale simulation in predicting the constriction flow of a two-dimensional foam*. J. Rheol. **56**, 457 (2012). doi:10.1122/1.3687301.

[125] C. Raufaste, S. J. Cox, P. Marmottant, and F. Graner. *Discrete rearranging disordered patterns: Prediction of elastic and plastic behavior, and application to two-dimensional foams*. Phys. Rev. E **81**, 031 404 (2010). doi:10.1103/PhysRevE.81.031404.

[126] I. Cheddadi, P. Saramito, and F. Graner. *Steady Couette flows of elastoviscoplastic fluids are nonunique*. J. Rheol. **56**, 213 (2012). doi:10.1122/1.3675605.

[127] M. Twardos and M. Dennin. *Comparison between step strains and slow steady shear in a bubble raft*. Phys. Rev. E **71**, 061 401 (2005). doi:10.1103/PhysRevE.71.061401.

[128] N. C. Keim and P. E. Arratia. *Role of disorder in finite-amplitude shear of a 2D jammed material*. Soft Matter **11**, 1539 (2015). doi:10.1039/c4sm02446j.

[129] V. Chikkadi and P. Schall. *Nonaffine measures of particle displacements in sheared colloidal glasses*. Phys. Rev. E **85**, 031 402 (2012). doi:10.1103/PhysRevE.85.031402.

[130] J. Chattoraj, C. Caroli, and A. Lemaître. *Robustness of avalanche dynamics in sheared amorphous solids as probed by transverse diffusion*. Phys. Rev. E **84**, 011 501 (2011). doi:10.1103/PhysRevE.84.011501.

[131] See supplemental material at `https://zenodo.org/record/57013`, or on YouTube under `https://www.youtube.com/vanheckelab/playlists`.

[132] D. Vella and L. Mahadevan. *The "Cheerios effect"*. Am. J. Phys. **73**, 817 (2005). doi:10.1119/1.1898523.

[133] G. Katgert. *Flow of Foams*. Ph.D. thesis, Leiden Institute of Physics (2008). hdl:1887/13329.

[134] K. Golemanov, N. D. Denkov, S. Tcholakova, M. Vethamuthu, and A. Lips. *Surfactant Mixtures for Control of Bubble Surface Mobility in Foam Studies*. Langmuir **24**, 9956 (2008). doi:10.1021/la8015386.

[135] I. Cantat, S. Cohen-Addad, F. Elias, F. Graner, R. Hohler, O. Pitois, F. Rouyer, A. Saint-Jalmes, and S. Cox. *Foams: Structure and Dynamics*. Oxford University Press, USA (2013). ISBN: 0199662894.

[136] R. J. Speedy. *Glass transition in hard disc mixtures*. J. Chem. Phys. **110**, 4559 (1999). doi:10.1063/1.478337.

[138] A. Saint-Jalmes. *Physical chemistry in foam drainage and coarsening*. Soft Matter **2**, 836 (2006). doi:10.1039/b606780h.

[139] *Basler A620f Users' Manual*. Basler Vision Technologies (2005).

[140] H. Hencky. *Über die Form des Elastizitätsgesetzes bei ideal elastischen Stoffen*. Z. Techn. Phys **9**, 215 (1928).

[141] R. O. Duda and P. E. Hart. *Use of the Hough transformation to detect lines and curves in pictures*. Communications of the ACM **15**, 11 (1972). doi:10.1145/361237.361242.

[142] F. P. Bretherton. *The motion of long bubbles in tubes*. J. Fluid Mech. **10**, 166 (1961). doi:10.1017/S0022112061000160.

[143] R. Yamamoto and W. Kob. *Replica-exchange molecular dynamics simulation for supercooled liquids*. Phys. Rev. E **61**, 5473 (2000). doi:10.1103/PhysRevE.61.5473.

[144] E. R. Weeks and D. Weitz. *Subdiffusion and the cage effect studied near the colloidal glass transition*. Chem. Phys. **284**, 361 (2002). doi:10.1016/s0301-0104(02)00667-5.

[145] J. Clara-Rahola, T. A. Brzinski, D. Semwogerere, K. Feitosa, J. C. Crocker, J. Sato, V. Breedveld, and E. R. Weeks. *Affine and nonaffine motions in sheared polydisperse emulsions*. Phys. Rev. E **91**, 010 301 (2015). doi:10.1103/PhysRevE.91.010301.

[146] X. Hong, M. Kohne, and E. R. Weeks. *Jamming is difficult in frictionless 2D hoppers* (2015). arXiv:1512.02500.